Bio-inspired Design of Geometrically-Structured Suture Interfaces and Composites

by

Erica Lin

A.B., Chemistry, Harvard University (2010)

Submitted to the Department of Materials Science and Engineering
in partial fulfillment of the requirements for the degree of

Doctor of Philosophy in Materials Science and Engineering
at the
MASSACHUSETTS INSTITUTE OF TECHNOLOGY

June 2015

Author.....
Department of Materials Science and Engineering
May 6, 2015

Certified by.....
Mary C. Boyce
Ford Professor of Engineering
Thesis Supervisor

Certified by.....
Christine Ortiz
Morris Cohen Professor of Materials Science and Engineering
Thesis Supervisor

Accepted by.....
Donald R. Sadoway
Chair, Departmental Committee on Graduate Students

Bio-inspired Design of Geometrically-Structured Suture Interfaces and Composites

by

Erica Lin

Submitted to the Department of Materials Science and Engineering on May 6, 2015 in partial fulfillment of the requirements for the degree of Doctor of Philosophy

Abstract

Nature is filled with incredible examples of multi-functional materials that have evolved to possess tailored mechanical behavior. This thesis explores the structure-function-property relationship and design principles of geometrically-structured suture interfaces and composites. Suture interfaces are mechanical structures found in rigid natural materials (e.g. human skulls, turtle shells, seashells) that bear loads and provide flexibility for respiration and growth. The geometry of suture interfaces has been shown to vary within species, across species, through development, and over time as organisms evolve. Using mechanical testing of 3D-printed, bio-inspired prototypes, finite element simulations, and analytical modeling, this thesis offers a systematic, comprehensive understanding of the relationship between suture interface geometry and mechanical behavior and provides insight into the suture interface geometries that exist in nature. Triangular, general trapezoidal, and hierarchical suture interfaces and composites are designed, fabricated, and tested. The stiffness, strength, toughness, and failure mechanisms of suture interfaces are shown to be directly influenced by suture geometry. Therefore, mechanical behavior of suture interfaces can be tailored or amplified through small changes in geometry. In addition, the bending behavior of suture composites can also be tailored through changes in suture interface geometry. With a detailed understanding of the deformation mechanisms of suture composites, optimal, multi-scale, hierarchical geometries can be designed.

Thesis Supervisor: Mary C. Boyce
Title: Ford Professor of Engineering

Thesis Supervisor: Christine Ortiz
Title: Morris Cohen Professor of Materials Science and Engineering

Acknowledgements

First and foremost, I would like to thank my advisors, Prof. Mary Boyce and Prof. Christine Ortiz, for introducing me to the world of bio-inspired science and mechanics of materials. I am inspired by their passion for research, and I am grateful for their support and encouragement throughout my time in graduate school. I deeply appreciate the freedom they gave us to explore and learn.

I am grateful for Prof. Yaning Li, who worked closely with me at the beginning of this project and really provided a lot of guidance and insight into the project. I also want to thank my committee members, Prof. Michael Rubner and Prof. Darrell Irvine for their feedback, advice, and encouragement. I walked out of every committee meeting feeling excited and inspired by their comments. I am grateful for the support of Jessica Landry, Teri Hayes, and Juliette Pickering – they were amazingly helpful in making sure meetings were scheduled and everything ran smoothly.

I also acknowledge Prof. Matusik, Javier Ramos, Wenshou Wang, Pitchaya Sitthi-Amorn, Kiril Vidimce, and Subra for their work on our collaboration. I have thoroughly enjoyed working and learning from each of you these past two years and have been inspired by the possibilities of your 3D printer.

I am grateful for the support of both the Ortiz and the Boyce group members: Narges Kaynia, Swati Varshney, Eric Arnt, Katia Zolotovsky, Matt Connors, Ling Li, Hansohl Cho, Mark Guttag, Shabnam Ardakani, Cody Ni, Ashley Durand, and Juha Song. I loved working with each of them and getting to know them outside of lab.

I would also like to thank BostonFound for their support and prayers these past five years. I have loved singing with them on a weekly basis. I am also grateful for being part of TAP. It has been a joy working and playing with them, and I appreciate all the support they have given me.

Last but not least, I could not have done it without my friends and family. I thank Joony, for believing in me and being there with me every step of the way; Julia, for being the best roommate ever, all the late nights, and listening to all my practice talks; Felix, for trekking out here every week for lunch, studying with me at the library, and your encouragement and understanding; Pan, for being my lunch buddy, all our coffee dates, and all the laughs we had; Tiffany, for your support and prayers despite being across the country; and last but not least, my parents, for all the phone calls and support throughout the years.

Table of Contents

List of Figures

1 Introduction

1.1 Motivation

Bio-inspired science is a growing field in materials science that learns from the mechanical design principles found in nature. Through evolution, nature has the amazing ability to utilize limited materials to create composite materials with superior properties that accomplish a wide variety of functions [1]. These design principles can be uncovered through careful study of structural properties. A few illustrative examples that have inspired research include mollusk shells that bear loads from waves and predators without fracturing [1], spider silks that have tensile strength comparable to high-grade silk[2], and geckos' feet that have exceptional high adhesive strength to allow geckos to climb trees[3].

The inspiration for this thesis is the diverse and complex suture interfaces observed in nature. Suture interfaces are mechanical structures consisting of compliant interlocking seams connecting stiffer components and provide flexibility to accommodate growth, respiration, and locomotion[4]. There are many examples of suture interfaces in nature with a wide variety of geometries—they can be found in skulls, diatoms, turtle shells, or the pelvic assembly of stickleback fish. The geometry can vary within a single suture structure (e.g. the suture interface of the stickleback fish which varies in frequency across the structure) through growth and development (e.g. the suture interface in human skulls), and across species and evolution (e.g. the suture interfaces of ammonites).

One particularly interesting example is the suture interface of the shells of ammonites, an ancient sea creature of the class Cephalopoda. The geometries of ammonite suture interfaces range from simple curves, to intricate, fractal-like designs [5]. Paleobiologists have observed an evolutionary trend toward complex suture interfaces in ammonite shells, implying that these designs are advantageous [6,7]. Why did evolution favor greater complexity of suture interfaces? What mechanical advantage do certain geometries of suture interfaces provide, if any? How do different geometries of suture interfaces affect the overall mechanical behavior of a biological structure?

This thesis aims to answer these questions through a systematic study of suture interface prototypes inspired by the many suture interface geometries observed in nature. The primary goal is to explore and understand the fundamental role of geometries in the mechanical behavior of suture interfaces and to extract design principles for new materials. Through this research, it will be possible to design new

materials with tailored mechanical behavior through changing suture interface geometries.

1.2 Overview

This thesis systematically investigates the detailed role of geometry in the mechanical behavior of bio-inspired suture interfaces and composites. Through this investigation, bio-inspired design principles for materials with tailored mechanical behavior are developed. The general approach taken is to observe designs in nature, create bio-inspired designs, prototype, and study through experimental testing and finite element analysis. In addition, analytical models were developed and verified by experiment in order to predict mechanical behaviors of a large range of geometric parameters. Bio-inspired designs with variation in specific geometric parameters were created in order to understand the direct effects of these parameters.

The main content of this thesis is organized into five chapters, with each chapter investigating mechanical behavior of suture interfaces and composites with increasing geometric complexity. In Chapter 2, we begin with the investigation of triangular suture interfaces. From these designs, the effect of the tip angle, or frequency, of the suture interface is explored, in addition to the effect of the constituent material properties.

Chapter 3 expands the triangular suture interfaces to general trapezoidal suture interfaces. Here, by changing the shape factor, or the angle of the slant interface, four main classes of suture interface geometries can be created. We demonstrate that slight changes in this shape factor result in the ability to tailor the mechanical behavior of the suture interface.

Chapter 4 is inspired by the fractal-like design of ammonite suture interfaces and adds order of hierarchy as a geometric parameter. By increasing the order of hierarchy, amplification of mechanical properties can be achieved, and we elucidate the mechanisms that give rise to this amplification.

In Chapter 5, we investigate the mechanical behavior of suture composites, both in bending and tension. In addition to tensile stiffness, strength, and toughness, the flexibility of the suture composite can be tailored to fit specific needs by changing geometry.

Finally, Chapter 6 explores suture interfaces with multi-scale hierarchical designs. Natural materials often possess intricate structures over many length scales that enhance their mechanical behavior. Therefore, we show as a proof of concept a simple multi-scale design with amplified mechanical properties.

1.3 Background

1.3.1 Suture Interface Examples

While there are a multitude of suture interfaces in nature, several examples are of particular interest to this thesis because of their geometric variation within species, within a certain structure across species, or even with development. Cranial suture interfaces are an example of variation within species and with development (Figure 1-1a). Suture interfaces exist in the skulls of many organisms, and serve as the primary sites of bone formation during skull growth [8]. Among species, the cranial suture interfaces range in complexity. Also, within the same species, there can be changes in cranial suture interface geometries as the organism grows and develops (Figure 1-1b). For example, infant vertebrate skulls have nearly flat suture interfaces, while adult vertebrate skulls have more complex, wavy suture interfaces [9].

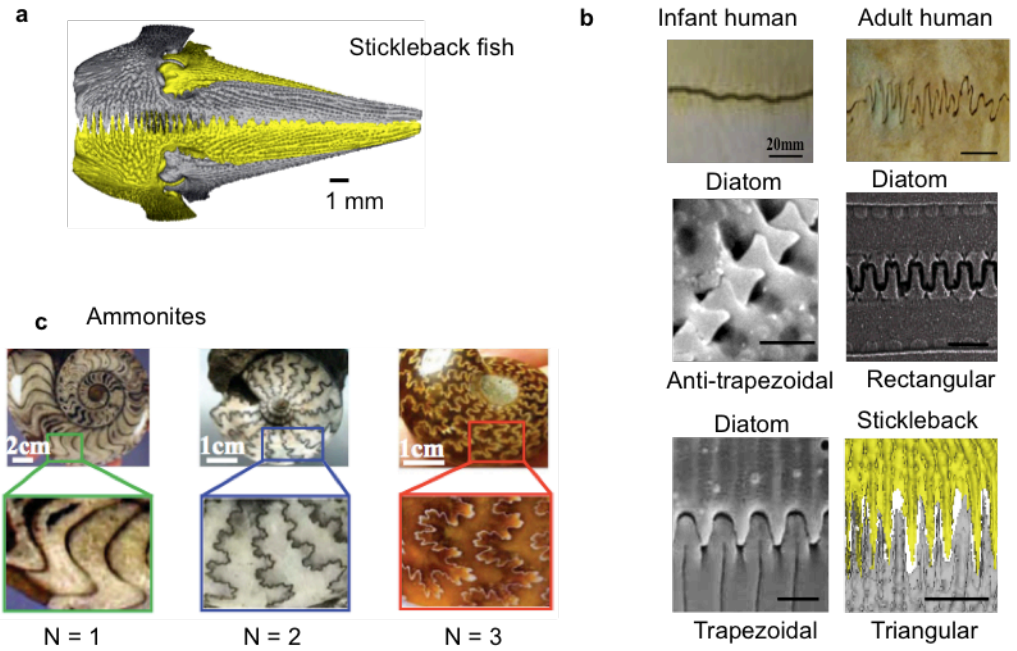

Figure 1-1| Examples of suture interfaces in nature. a) Suture interfaces in the pelvic assembly of the stickleback fish that vary in frequency [10], b) first-order geometric suture interfaces in human skulls, diatoms, and the stickleback fish [11], c) hierarchical suture interfaces in ammonites [12].

The triangular suture interfaces in the pelvic assembly of the marine three-spined stickleback fish (Gasterosteus aculeatus) are of interest because they demonstrate geometric variation within a certain structure. In particular, the frequency, amplitude, and amount of interdigitation of the suture interface is observed to vary spatially across the structure. This variation is suggested to allow increased stiffness and load-bearing support at critical locations where it is needed. [10]

Diatoms also exhibit variation in the same structure across species (Figure 1-1b). They have suture interfaces with a variety of simple geometries, ranging from trapezoidal to rectangular to anti-trapezoidal [13]. These variations in suture interface geometries are the motivation behind the exploration of mechanical advantages that drive geometric variation.

The intricate suture interface geometries on the ammonites are perhaps the most fascinating of all. The complexity, or order of hierarchy varies across different ammonites (Figure 1-1c) from simple curves to complex, fractal-like patterns. In addition, even within a single ammonite, the suture is a three-dimensional structure that has higher complexity near the surface (Figure 1-2).

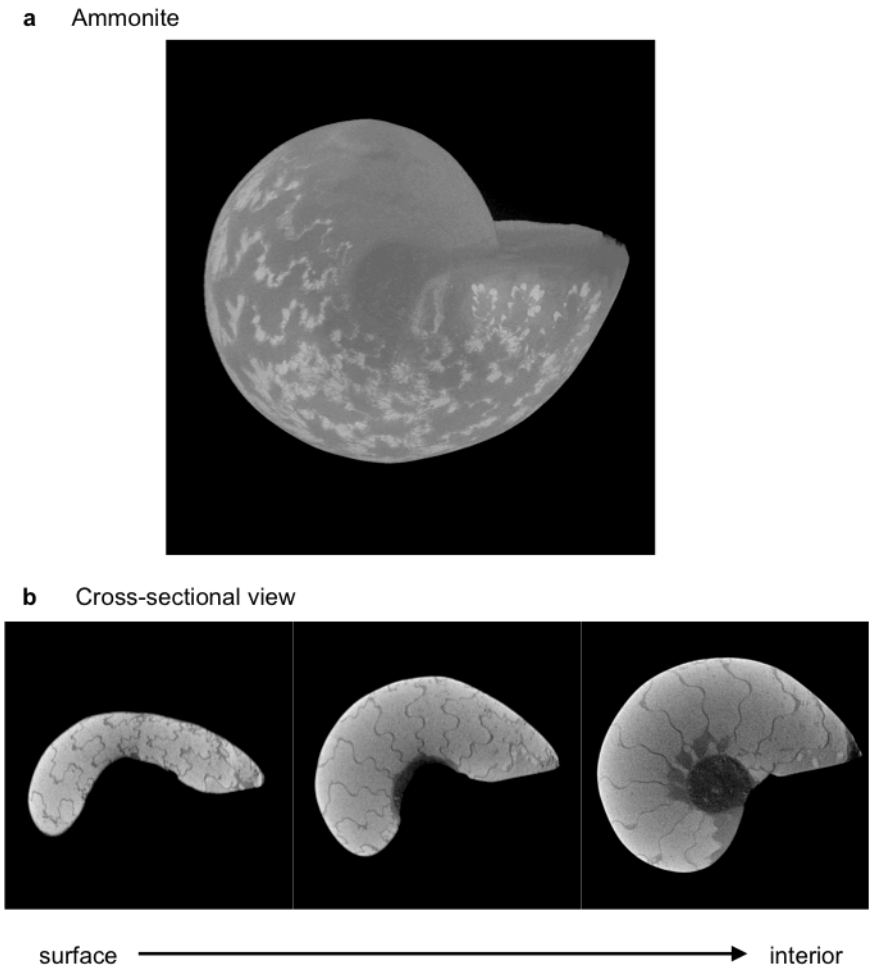

Figure 1-2| MicroCT image of ammonite shell. a) Three-dimensional view of ammonite shell, b) Cross-sectional view of ammonite shell from the surface to the interior showing the increase in complexity near the surface of the shell.

1.3.2 Function of suture interfaces

In general, suture interfaces are known to provide flexibility to accommodate growth, respiration, or locomotion [14]. However, the specific function of suture interfaces, and why certain suture interfaces possess certain geometries is unclear. For ammonite sutures in particular, the function of suture interface complexity has been debated. The most widely cited explanation is the Buckland hypothesis, which relates complex suture interfaces to higher strength to protect against implosion ([15]Buckland, 1836). This theory has been both supported by analysis using mechanical principles [16] and refuted by empirical evidence analyzing suture complexity of species in relation to the depth at which the ammonite resided [6,17].

Despite the disagreements, it has generally been agreed upon that the different geometries of suture interfaces serve at least a mechanical purpose. As mentioned before, cranial suture interfaces in vertebrates change geometries through growth and development. The easily modifiable cranial suture morphology suggests that it is a mechanical signal that triggers the changes. [14] Thus, this research focuses primarily on mechanical behavior, but can serve as a gateway to the studies of other properties.

1.3.4 Mechanical behavior of suture interfaces and composites

The mechanical behavior of specific suture interfaces has been studied both experimentally and through finite element analysis. Experimentally, it has been found that while skulls with suture interfaces are not as strong in bending as skulls without suture interfaces, skulls with suture interfaces have a significant increase in energy absorption [18] and are slightly more compliant [19]. In addition, an increase in interdigitation provides increased strength in three-point bending [18]. The suture interface of turtle shells demonstrate a nonlinear behavior under three-point bending—an initial low stiffness regime is followed by a linear, higher stiffness regime when the two sides of the bone meet, lock, and resist further deformation [20]. Also, for interfaces in general, it has been shown that interfacial strength can be enhanced through geometric complexity [21].

Additionally, finite element modeling has provided more insight into the mechanical behavior of suture interfaces. The suture interfaces of lizard skulls were found to play an important role in redistributing strain around the skull without reducing the total strain within the skull [22]. Also, increased interdigitation of suture interfaces was found to correspond with decreased suture strain energy [23].

Though research has been done on the mechanical properties of specific suture interfaces, a comprehensive, systematic study of the relationship between geometry and mechanical behavior of suture interfaces and composites is needed. There are many challenges to performing mechanical tests on biological samples, including difficulty of sample preparation, and the relationship between geometry and mechanical properties cannot be clearly elucidated due to the heterogeneity and randomness of biological samples. Therefore, the approach presented in this thesis, which utilizes mechanical testing of bio-inspired 3D-printed prototypes in combination with finite element and analytical models, acts as a framework for any future study that wishes to determine the relationship between geometry and mechanical behavior of any composite material.

1.3.5 Analytical models

Recently, the first step toward a systematic study of the relationship between geometry and mechanical behavior of sutures has been taken with the development of an analytical model predicting the strength, stiffness, and toughness of suture interfaces with several types of geometries. The analytical model has been derived for several geometric cases: first-order triangular suture interfaces, first-order suture interfaces of arbitrary geometry, and hierarchical suture interfaces. First-order suture interfaces indicate a single waveform, while hierarchical suture interfaces of higher orders refer to a fractal-like geometry, where a self-similar waveform is superimposed on the waveform of the prior order of hierarchy.[4]

The analytical models are able to predict mechanical properties of the suture interface given the geometric parameters and basic material properties of the teeth and interface. The models assume linear elasticity and deformable teeth; and the results were verified through finite element analysis. Several key findings resulted from the development of these analytical models. First, the triangular geometry was found to be optimal, in that it is the only geometry with uniform stress distribution in both the teeth and interface when under tension. Therefore, the triangular suture interface optimally distributes the stress across the structure, resulting in higher stiffness and strength relative to other geometries. [4] In addition, the results showed the possibility of nonlinearly amplifying and tailoring the mechanical behavior of a suture interface through changes in the order of hierarchy [11,12].

From these results, it is evident that suture interfaces have the potential of playing an important role in the amplification and tailorability of mechanical behavior of materials.

2 Triangular suture interfaces

2.1 Introduction

This chapter is motivated by the suture interfaces observed in the pelvic girdle of the stickleback fish (Figure 1-1a). This particular structure shows suture interfaces where the teeth are triangular and vary in frequency within a single suture structure and also differ for marine and freshwater stickleback fish (Figure 2-1). This chapter explores the effect on mechanical behavior of this simple change in frequency and aims to understand why this variation would exist.

Based on the analytical model developed by Li et al.[4], the triangular geometry was determined to the one and only geometry that is able to uniformly distribute stress across the tooth, resulting in higher stiffness and strength. In addition, for the triangular geometry, the relationship between the normal stress and shear stress is dependent only on the tip angle. The stiffness of the resulting suture interface structure was found to be dependent on the volume fraction of the interface, the tip angle, and properties of the constituent materials. For a given volume fraction and set of constituent material properties, suture interfaces with small tip angles are predicted to have higher stiffness.

The analytical model shows a clear dependence of the stiffness and strength of a triangular suture interface on the tip angle. In order to gain a better understanding of the effect of tip angle on mechanical behavior (stiffness, strength, toughness, failure mechanisms), this chapter shows results from experimental mechanical tests on 3D-printed prototypes.

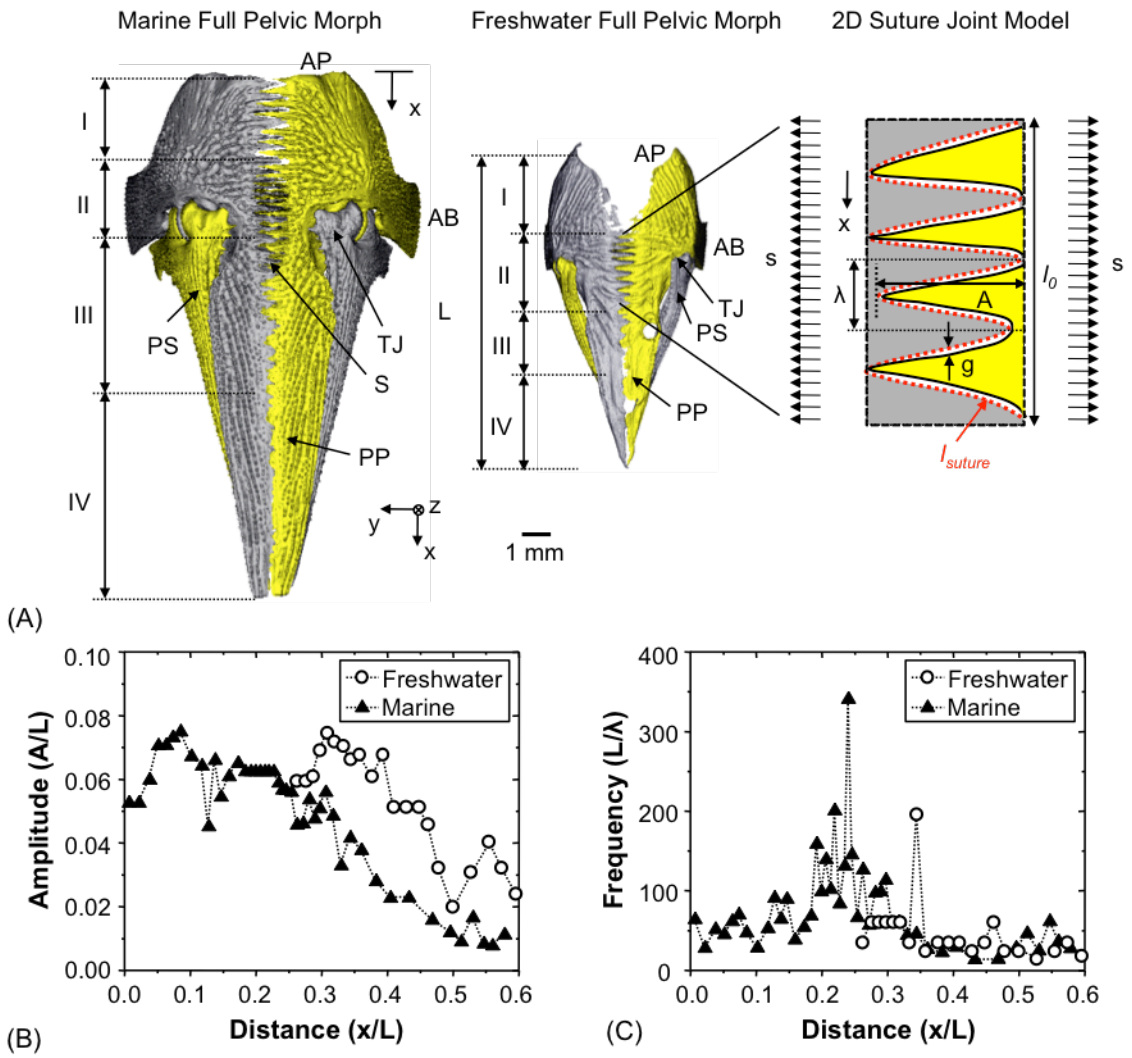

Figure 2-1| Two-dimensional morphology of the ventral median suture of bilateral pelvic girdles from marine and freshwater stickleback fish. a Ventral view of three-dimensional microCT images of the pelvic girdles (retracted position) from marine (*left*) and freshwater (*right*) *G. aculeatus* with schematic diagram of a two-dimensional suture model. The marine microCT image is similar to that reported previously (*8*). Scale bar ~ 1 mm. b-e, The dorsal to ventral spatial distribution of: b and c, relative amplitude, *A*/*L*, (b) and spatial frequency, *L*/*λ*, (c), of the median suture in marine and freshwater *G. aculeatus*; and d, predicted suture stiffness of both *G. aculeatus* populations. e, Average stiffness and ID of four regions in marine and freshwater *G. aculeatus*. †A: amplitude of a median suture, AB: ascending branch, AP: anterior process, L: total length of pelvis, PP: posterior process, PS: pelvic spine, S: median suture, TG: trochlear joint, *λ*: width of a suture tooth, g: width of the interphase region between neighboring ventral suture teeth. (Song, in prep)

2.2 Materials and Methods

Bio-inspired artificial triangular suture joints with three different frequencies were designed using Solidworks. The frequencies of the suture joints were varied by altering the tip angle θ, while maintaining a constant volume fraction of 75% and an interface

width of 0.5 mm. Samples were then fabricated with the Connex500 3D multi-material printer (Objet Geometries, USA). VeroWhite, an acrylic-based photo-polymer, was used for the tooth, TangoPlus, a rubber-like flexible material, was used for the interface. To test the basic mechanical properties of VeroWhite and TangoPlus, standard ASTM D-638-V dogbones of each material were individually fabricated. Standard dogbones were oriented at 0°, 45°, and 90° to test anisotropy. These material properties are used for the theoretical predictions of the various suture joints. Four samples of each frequency of suture joints were tested using a Zwick Mechanical Tester (Zwick Z010, Zwick Roell, Germany) for force-displacement measurements in conjunction with a video extensometer and digital image correlation software for local strain measurements. All tests were quasi-static with a constant strain rate of 0.002 s^{-1}.

2.3 Results

Figure 2-1 demonstrates the successful fabrication (Fig. 2-1a) and mechanical testing (Fig. 2-1b) of 3D-printed triangular bio-inspired artificial suture interfaces of varying frequency ($\theta = 2.85^\circ, 5.70^\circ, 11.30^\circ$), which experimentally validate the theoretical predictions and also provide proof-of-concept for rational geometrically-optimized bio-inspired design. Tensile stress versus strain behavior, including Young's modulus, tensile strength, failure mechanisms, and toughness), are seen to vary dramatically with suture frequency, with Young's modulus, tensile strength, and toughness increasing nonlinearly with increasing suture frequency (Fig. 2-1b). The suture interface theory (input parameters; volume fraction of tooth material, tooth angle θ, Young's modulus of tooth material, Young's modulus of interface material, shear modulus of interface material) predicts the experimental data exceedingly well (Fig. 2-1b). Predictions from the suture interface theory at different material properties show that increasing the stiffness or strength ratios of the interface material to the tooth material results in an increase of the effective mechanical properties for all frequencies. The same effective mechanical property can be achieved with a lower frequency suture interface by utilizing materials of a higher stiffness or strength ratio.

In all cases, the bio-inspired suture joints exhibit geometrically-controlled toughening mechanisms leading to non-catastrophic "graceful failure". The highest frequency suture interface ($\theta = 2.85^\circ$) reaches its maximum load-bearing capacity at a strain smaller than that of the lower frequency suture interface. After reaching its peak, the highest frequency suture joint has a steep drop in load-bearing capacity. The lowest frequency suture joint ($\theta = 11.30^\circ$) reaches its maximum load-bearing capacity at a higher strain and has a more gradual decline in load-bearing capacity. Failure mechanisms were observed *in situ* in Fig. 2-1d. For $\theta = 2.85^\circ$, the suture interface fails discretely at an increasingly numbers of locations until the entire interface is

disconnected. For $\theta = 11.30^{\circ}$, the initial load pulls the teeth slightly closer together and then interface failure releases this initial tension, and the teeth relax to their initial configuration, resulting in simultaneous failure of many locations across the interface, corresponding to a steeper drop in load-bearing capacity. Finite element analysis of the suture interfaces (Figure 2-2) with different frequencies at each of its maximum load-bearing capacities show localization of strain at the interface. Also, higher frequency suture interfaces have greater normal stress in the teeth. In addition, maximum principal strain in the interface is the same for all frequencies at maximum load-bearing capacity.

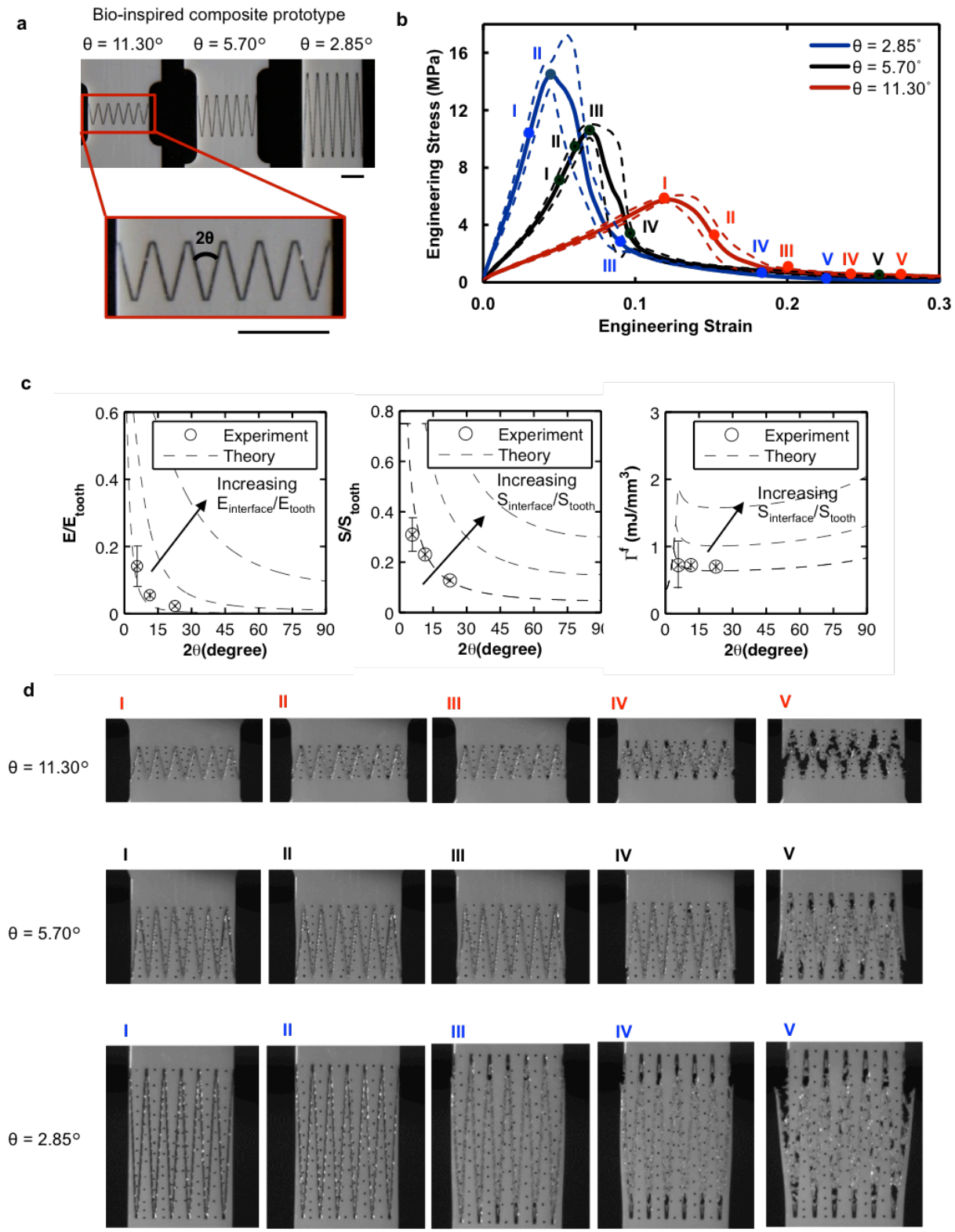

Figure 2-1| Mechanical behavior of artificial bio-inspired triangular suture interfaces. a, 3D printed prototypes of triangular suture joints with three different frequencies. b, Stress-strain behavior of triangular suture joints with three different frequencies. c, Nondimensional stiffness (E/E_{tooth}), nondimensional strength (S/S_{tooth}), and toughness (Γ_f) of triangular suture joints of different frequencies

compared to theoretical predictions from the suture interface model at different material properties ($E_{interface}/E_{tooth}$ = 0.035%, 0.5%, 5%, $S_{interface}/S_{tooth}$ = 3.2%, 10%, 20%, and $S_{interface}/S_{tooth}$ = 3.2%, 4.0%, 5.0%, for the stiffness, strength, and toughness comparisons respectively). d, Images showing the deformation of the triangular suture interfaces at corresponding stresses and strains indicated of the tensile stress-strain curves.

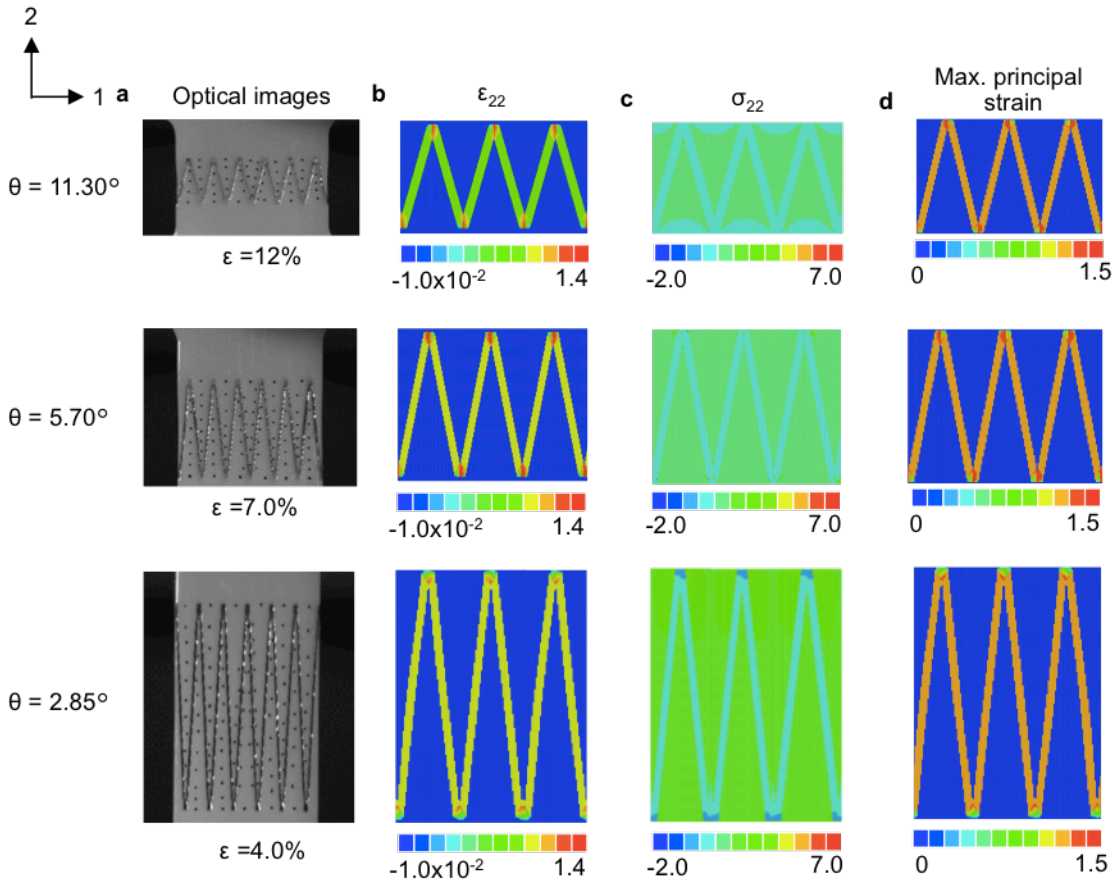

Figure 2-2| Finite element analysis of triangular suture interfaces at its experimental maximum load-bearing capacity. a Images of triangular suture interface prototypes at maximum load-bearing capacity, b contours of normal strain in the direction of loading (ε_{22}) c contours of normal stress in the direction of loading (σ_{22}), d and contours of maximum principal strain.

2.4 Discussion

In the stickleback fish, the tip angle of the triangular suture interfaces are shown to vary from 2θ = 3° to 2θ =180°. From the results shown above, this wide range in tip angle can allow for significant (close to an order of magnitude) local variations in stiffness, strength, toughness, and failure mechanisms. Regions with smaller tip angles were shown to correlate with regions that need to offer increased mechanical support to the trochlear joints and pelvic spines. Therefore, variation in tip angle is a simple way of changing suture interface properties.

3 Structured general trapezoidal suture interfaces

This chapter was published as an article in the *Journal of Mechanics and Physics of Solids* in 2014 [24].

3.1 Introduction

Geometrically structured interfaces are prevalent throughout nature and give rise to many remarkable mechanical properties in a number of biological materials ([25]Bruet et. al., 2008; Dunlop et al., 2011; Y. Li et al., 2011, 2012, 2013a; Weiner and Addadi, 1997; Zhang et al., 2012). For example, both computational [26] and experimental studies ([21]Bruck et al., 2004) reveal that geometrically interlocking interfaces enhance interfacial stiffness and strength, and interface waviness increases resistance to crack propagation [27].

A particularly fascinating example of geometrically structured interfaces is composite suture interfaces. Suture interfaces are mechanical structures often found in biology consisting of compliant, interlocking seams connecting stiffer components [5]. In nature, a wide range of suture interface geometries are observed, ranging from nearly flat suture interfaces in infant human skulls [9] to intricate, fractal-like designs in ammonites [6]. Suture interface geometries are found to vary within species [5], within a certain structure across species [10], through evolution [7], or even with development [28]. The diverse interface geometries hint at nature's ability to utilize a limited set of natural materials to achieve a wide range of properties and functions simply through variation in geometry [29].

The geometry of suture interfaces has been shown, experimentally or through finite element analysis (FEA), to influence mechanical performance. Suture interfaces have been found to increase energy absorption [18], compliance [19], deformability, [30] and flexibility [14]. In addition, suture interfaces were shown to play an important role in the redistribution of strain in skulls [22]. Increased interdigitation in suture interfaces was found to increase bending strength [18] and decrease suture strain energy [23]. These studies confirm that geometric variation affects the effective mechanical behavior of the suture interface. However, a systematic, comprehensive experimentally-verified understanding of the underlying role geometry plays in the overall mechanical behavior, including stiffness, strength, toughness, and failure mechanisms of suture interfaces, is lacking.

Recently, we developed a generalized analytical suture interface model for the case of in-plane loading of any suture interface with arbitrary geometry verified by finite

element modeling [4,11,31]. This model gives analytical solutions for the effective stiffness, strength, and fracture toughness of suture interfaces with an unbonded tip interface in terms of a set of independent geometric parameters and material properties of the compliant seam and stiffer interdigitating "teeth". Using this analytical model, it was predicted that the mechanical properties of suture interface systems have a highly nonlinear dependence on geometry and order of hierarchy. In addition, a general trapezoidal suture interface was predicted to possess significantly enhanced stiffness, strength, and fracture toughness relative to a flat interface. For a given set of materials, altering the geometry of the suture interfaces was found to result in a range of values for stiffness, strength, and fracture toughness, demonstrating the possibility of precise tailorability of mechanical properties through geometry.

The objectives of this study are threefold. On the theoretical side, the analytical model presented in Li et al. (2013) is extended to include the behavior of suture interfaces with bonded tip interfacial layers. In nature, suture interface geometries typically consist of initially fully bonded interfaces, and therefore the effect of a fully bonded interface on the effective mechanical behavior is determined. Experimentally, the relationship between geometry and mechanical behavior of general trapezoidal suture interfaces is systematically explored, through the design and fabrication of bio-inspired prototypes via 3D printing and mechanical experiments. Previously, we have employed 3D printing fabricate co-continuous composite structures with enhancements in stiffness, strength, and energy dissipation ([32]) and subsequently this fabrication method has been rapidly emerging as a means to create physical prototypes of material structures to explore the roles of geometry and materiality on properties and performance ([33-35]). Here, we exploit multi-material 3D printing to construct physical prototypes of a range of suture waveforms with soft, compliant interface layers adhering stiffer skeletal teeth and reveal the ability to tune the mechanical behavior (stiffness, strength, toughness, deformation and failure mechanisms) through the interplay between geometry and materiality. Four categories of bio-inspired representative periodic geometries that resemble suture interfaces in the linking girdles of diatoms (Figure 3-1A) are chosen: anti-trapezoidal, rectangular, trapezoidal, and triangular (Figures 3-1B and 3-1C). These four geometries were designed to possess the same tooth volume fraction and wavelength, and the same interfacial layer thickness and material combination. Hence, the only difference is the shape. Specifically, we focus on three design parameters, which include bonded vs. unbonded flat interfacial layer at the peaks of the teeth, tooth tip angle (θ), and a shape factor β (Figure 3-1B) defined by Li et al. ([11]) to distinguish tooth shape. This study enables the extraction of design principles from the theoretical and experimental results for the design of new material interfaces with tailored mechanical behavior.

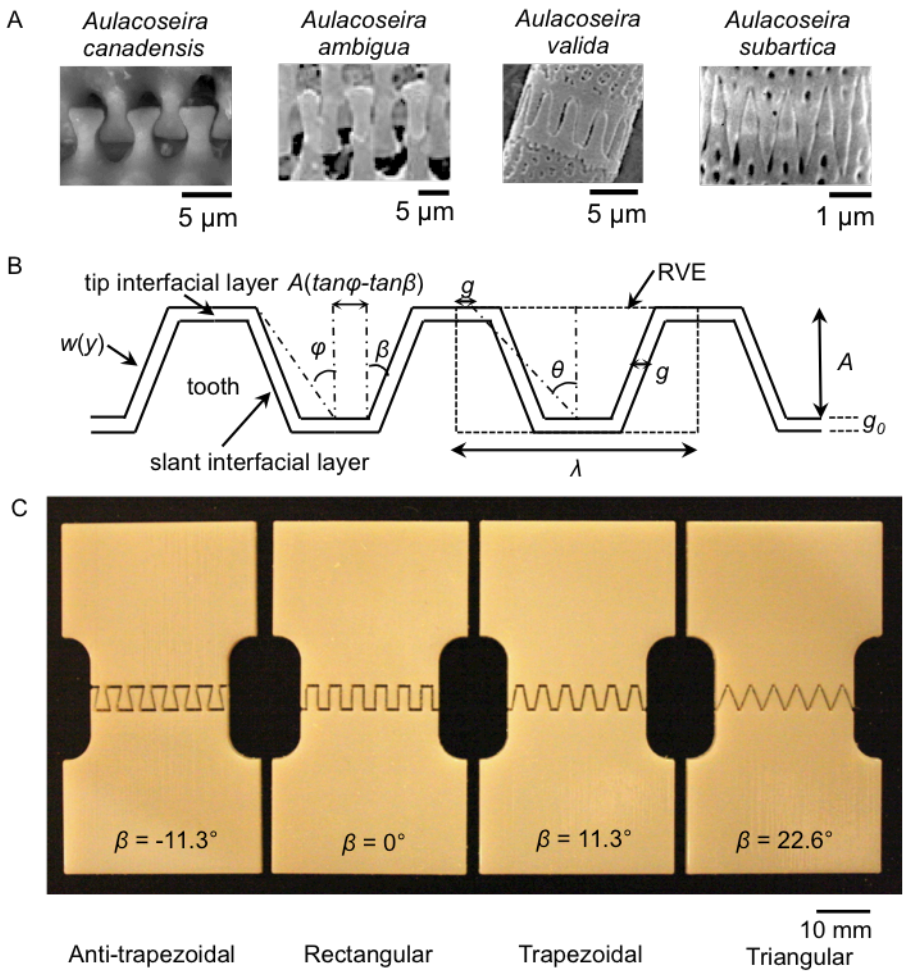

Figure 3-1| Inspiration and design of bio-inspired suture interfaces. A) Examples of suture interfaces in nature (Manoylov et. al, 2009; Bahls et. al, 2009; Genkal and Popovskaya, 2008), B) Schematic of general trapezoidal suture interfaces and defining geometric parameters, C) optical images of bio-inspired 3D printed suture interface prototypes.

3.2 Materials and methods

Bio-inspired suture interfaces with and without bonded tip regions, with different tip angles, and with different geometries were designed within Solidworks (Dassault Systemes, 2013) and fabricated (Figure 3-1C) with an Objet Connex500 3D multi-material printer (Stratasys Ltd., USA). VeroWhite, an acrylic-based photo-polymer, was used for the teeth, and TangoPlus, a rubber-like compliant material, was used for the interfacial layers. For each set of designs, the volume fraction and interface width were held constant. Four samples of each design were tested and all errors reported represent standard deviation. The resolution of the 3D multi-material printer is 16 micrometers in the z-direction (thickness) and 42 micrometers in the x and y-direction. Therefore the

smallest feature size of the prototypes is designed to be at least an order of magnitude greater than the resolution to minimize any effects of the manufacturing process on the mechanical behavior.

To test the basic mechanical properties of VeroWhite and TangoPlus, standard ASTMD-638-V dogbones of each material were individually fabricated. The Young's moduli of TangoPlus and VeroWhite were determined to be 0.63 +/- 0.02 MPa and 2.0 +/- .09 GPa, respectively. The tensile strength of TangoPlus and Verowhite were determined to be 1.1 +/- 0.2 MPa and 43.7 +/- 0.3 MPa, respectively (Figure 3-2A). In addition, in order to test the pure tensile and simple shear strength of the interfacial layer, samples with a flat interface and a simple shear interface were designed and fabricated (Figure 3-2B). Due to the nature of the 3D printing, and recognizing the presence of a graded material region in between the tooth material and the interfacial layer, two interface widths of 0.5 mm and 1 mm were used in the suture prototype designs, and the tensile and shear strength for each interface width was tested. The tensile strength is determined to be 1.8 +/- 0.94 MPa and 0.97 +/- 0.41 MPa for an interface width of 0.5 mm and 1 mm, respectively. The shear strength is determined to be 1.4 +/- 0.11 MPa and 1.1 +/- 0.16 MPa for interfacial layers of 0.5 mm and 1 mm, respectively. For both interface widths, the interfaces exhibit nonlinear elastic behavior until initial failure, at which point plastic deformation occurs until catastrophic failure. Failures were found to be cohesive failures within the interfacial layer. The cohesive failure was verified through SEM of 3D-printed suture interface prototypes post-failure ([36]). These material properties were used for the analytical predictions of the various suture interfaces. To account for the different properties between the two interface widths, the experimentally determined material properties corresponding to the interface width are utilized in analytical predictions to represent the tensile strength of the interface material.

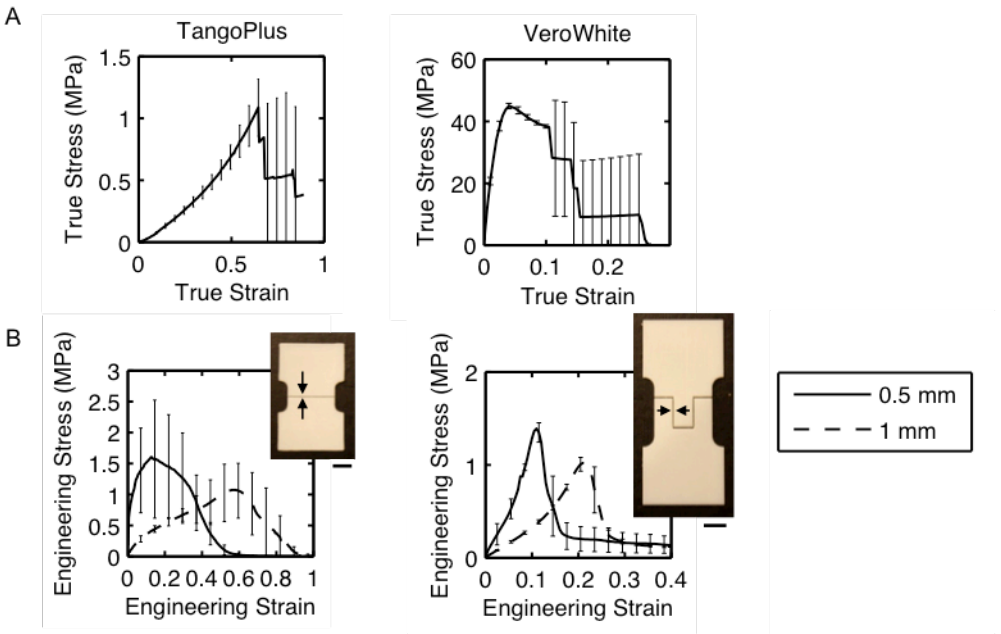

Figure 3-2 | Mechanical properties of 3D-printed material under uniaxial longitudinal tension. A) True stress-true strain curves of interfacial layer (TangoPlus) and tooth material (VeroWhite), B) flat and shear interface specimen and experimental stress-strain behavior. Scale bars are 10 mm, and error bars indicate standard deviation.

Four samples of each suture interface design were tested using a Zwick Mechanical Tester (Zwick Z010, Zwick Roell, Germany) for force-displacement measurements in conjunction with a video extensometer and digital image correlation (DIC) software (VIC2D) for global and local strain measurements and contours in the suture area (including both teeth and interfacial layers). All experiments were quasi-static with a constant strain rate of 0.002 s^{-1}. Engineering stress was calculated from force measurements, while engineering strain was calculated from local displacement measurements from DIC.

3.3 Theory

The geometry of a general trapezoidal suture interface can be described by five independent parameters: the wavelength, λ, the tooth amplitude, A, the shape factor, β, the slant interface width, g, and the tip interface width, g_0 (Figure 1B). β determines the shape of the suture interface: anti-trapezoidal when $-\theta < \beta < 0$, rectangular when $\beta = 0$, trapezoidal when $0 < \beta < \theta$, and triangular when $\beta = \theta$, (Li et al., 2013). The frequency of the waveforms can be quantified by the nondimensional tooth tip angle, θ, defined as $\tan\theta = \frac{\lambda - 2g}{2A}$. For the same tooth volume fraction, θ corresponds to the aspect ratio, $\frac{\lambda}{A}$, of a representative volume element. The tooth angle, φ, is defined as $\tan\varphi = \frac{(\tan\beta + \tan\theta)}{2}$.

In the following section, the analytical models derived via the principle of complementary virtual work presented in Li et al. (2013a) are expanded to derive the in-plane tensile modulus, tensile strength, and fracture toughness of suture interfaces with a bonded interfacial layer at the tip region. In all derivations, the tooth and interfacial layers are assumed to be perfectly bonded over the entire interface. Both interface and tooth phases are taken to be homogeneous, linear elastic and isotropic. The slanted and tip interfacial layers are considered to have no direct interaction (Figure 3-3A). These assumptions are appropriate for the prediction of stiffness, strength, and toughness for the 3D-printed suture interface prototypes: the 3D-printed materials are shown experimentally to be isotropic and homogeneous and the cohesive failure of the interfacial layer closely approximates a perfectly bonded tooth and interfacial layer.

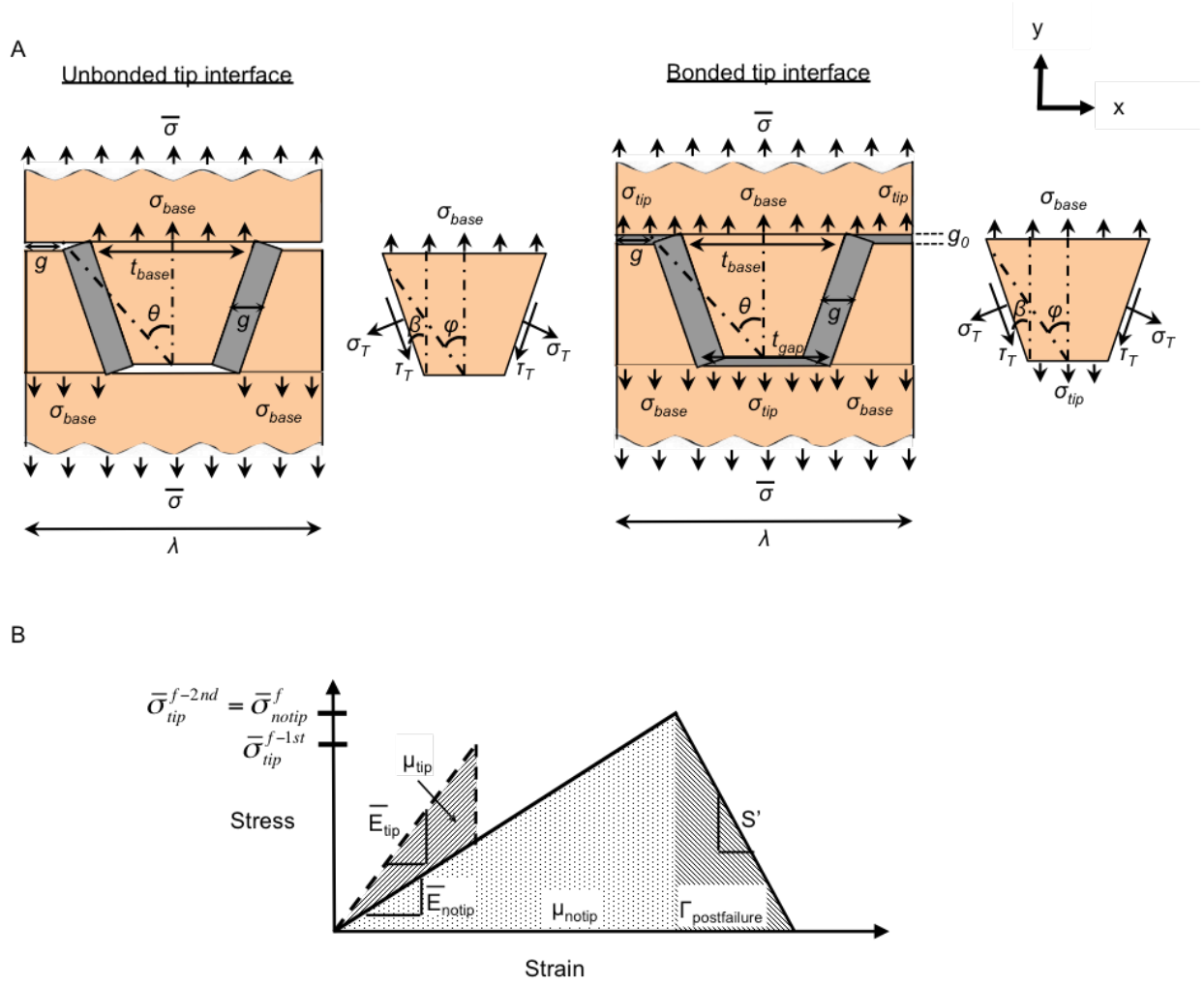

Figure 3-3 | Schematic of mechanical model. A) Diagram showing geometry of suture interface with unbonded vs. bonded tip interface, and the corresponding stresses under uniaxial longitudinal tension, B) schematic of expected mechanical behavior of suture interface with un-bonded and bonded tip interface under uniaxial longitudinal tension, where $\bar{\boldsymbol{\sigma}}^{t}_{\text{tip}}$ and $\bar{\boldsymbol{E}}_{\text{tip}}$ are the strength and stiffness from the bonded tip

interface, $\bar{\boldsymbol{\sigma}}^{f}_{notip}$ and $\bar{\boldsymbol{E}}_{notip}$ are the strength and stiffness from the slant interface, and S′ is the post-peak failure process.

3.3.1 In-plane tensile modulus

The suture interface under tension due to far-field loading, $\bar{\sigma}$, perpendicular to the suture axis, is balanced by stress across the base of the tooth, σ_{base}, and the normal stress across the tip region, σ_{tip}, as shown in Figure 3A, with the relationship

$$\bar{\sigma} = \left[\sigma_{base}\frac{t_{base}}{\lambda} + \sigma_{tip}\frac{t_{gap}}{\lambda}\right] \tag{1}$$

where $t_{base} = 2A\tan\varphi$ and $t_{gap} = \lambda - 2A\tan\varphi$ are the lengths of the base and gap between teeth, respectively; and A and λ are the amplitude and wavelength of the tooth geometry, respectively.

The tension at the base of the tooth, σ_{base}, is further balanced by the interfacial shear stress, τ_T, and interfacial normal stress, σ_T, and the normal stress across the tip, σ_{tip}, as shown in the free-body diagram in Figure 3A. Force equilibrium in the x and y directions yields

$$\sigma_T = \tau_T \tan\beta \tag{2a}$$

and

$$\sigma_{base}\tan\varphi = \sigma_{tip}(\tan\varphi - \tan\beta) + \frac{\tau_T}{\cos^2\beta}. \tag{2b}$$

3.3.1.1 Rigid tooth model (RTM)

First, we consider the case of the Rigid Tooth Model (RTM) where the teeth are assumed to be rigid. The total strain energy, $U_{T,RTM}$ due to applied tension across the suture can be expressed as

$$U_{T,RTM} = \frac{1}{2}\bar{E}_{tip}\varepsilon^2 V, \tag{3a}$$

where $\bar{E}_{tip}$ denotes the effective modulus of the suture interface with tip material, ε is the effective axial strain across the entire suture area, and $V$is the volume of the entire suture, and $V = (A + g_0)\lambda$.

$U_{T,RTM}$ can also be expressed in terms of the interfacial layer contributions

$$U_{T,RTM} = \frac{1}{2} V_{slant} \left[\frac{(\sigma_T)^2}{E_0^{PS}} + \frac{(\tau_T)^2}{G_0} \right] + \frac{1}{2} V_{tip} \frac{(\sigma_{tip})^2}{E_0^{PS}}, \quad (3b)$$

where V_{slant} is the volume of the slanted region of the interface, V_{tip} is the volume of the tip region, E_0^{PS} is the plane strain tensile modulus of the interfacial material, and G_0 is the shear modulus of the interfacial material.

By equating Eq. (3a) and Eq. (3b), an expression for the effective stiffness, $\bar{E}_{tip}$, can be derived.

For a small elastic deformation, δ, equilibrium and kinematic analysis of the slanted and tip interface regions yield

$$\sigma_{tip} = E_0^{PS} \varepsilon_{tip} = E_0^{PS} \frac{\delta}{g_0}, \quad (4a)$$

$$\tau_T = G_0 \gamma_{slant} = G_0 \frac{\delta}{g}. \quad (4b)$$

By substituting Eq. (2) and Eqs. (4a, b) into Eqs. (3a,b), the effective tensile modulus of a suture interface with a bonded tip area and rigid teeth is derived to be

$$\bar{E}_{tip,RTM} = E_{slant} + E_{tip}, \quad (5a)$$

where

$$E_{slant} = f_s \left(\frac{A}{g} \right)^2 \left[\frac{G_0^2}{E_0^{PS}} \tan^2 \beta + G_0 \right]; \quad (5b)$$

$$E_{tip} = f_t E_0^{PS} (\frac{A}{g_0})^2, \quad (5c)$$

and where f_s and f_t are the volume fractions of the slant interfacial layer and tip interfacial layer in the suture area, respectively; and $f_s = \frac{V_{slant}}{V} = 1 - \frac{2g}{\lambda}$, and $f_t = \frac{V_{tip}}{V} = \frac{2t_{gap} g_0}{\lambda(A+g_0)}$.

The bonded tip region provides an increase in stiffness that can be expressed as the ratio of E_{slant} to E_{tip}, R_S:

$$R_s = \frac{E_{tip}}{E_{slant}} = \frac{f_t}{f_s} \left(\frac{g}{g_0} \frac{E_0^{PS}}{G_0} \right)^2 \left[\frac{1}{\tan^2 \beta + \frac{E_0^{PS}}{G_0}} \right]. \quad (5d)$$

As will be seen later, this increase in stiffness can be significant. For example, for the case of $\theta = 22.6°$ and $\beta = 0°$ (a rectangular suture), $R_S = 0.71$ meaning a 71% increase in stiffness.

3.3.1.2 Deformable Tooth Model (DTM)

A rigid tooth assumption is reasonable when the tooth modulus, $E_1 \geq 1000\, E_0^{PS}$. However, in general, the deformation of the teeth can add compliance and can be a significant contribution to the strain energy. Therefore, using a deformable tooth model, the total strain energy, $U_{T,DTM}$, of the suture interfaces is from the slant interface, the tip interface, and the teeth.

$$U_{T,DTM} = \frac{1}{2}\frac{\bar{\sigma}^2 V}{\bar{E}_{tip,DTM}} = U_{slant} + U_{tip} + U_{tooth} \tag{6a}$$

where

$$\begin{aligned} U_{slant} &= \frac{1}{2} V_{slant}\left[\frac{(\sigma_T)^2}{E_0^{PS}} + \frac{(\tau_T)^2}{G_0}\right]; \\ U_{tip} &= \frac{1}{2} V_{tip}\left[\frac{(\sigma_{tip})^2}{E_0^{PS}}\right]; \\ U_{tooth} &= 2\int_0^A \frac{\sigma_{yy}(y)^2}{E_1} w(y)dy\,, \end{aligned} \tag{6b}$$

where $w(y)$ is the profile of the slant edge, given by (Li et al., 2013)

$$w(y) = y\,tan\beta + A(tan\varphi - tan\beta), \quad 0 \leq y \leq A, 0 \leq w(y) < \frac{\lambda f_v}{2}, \tag{6c}$$

and where $\sigma_{yy}(y)$ is the stress distribution in the tooth, given by

$$\sigma_{yy}(y) = \frac{[\sigma_{base}\,\tan\varphi - \sigma_{tip}\,(\tan\varphi - \tan\beta)]y + A\,(\tan\varphi - \tan\beta)\sigma_{tip}}{y\,\tan\beta + A\,(\tan\varphi - \tan\beta)}. \tag{6d}$$

The full expressions and derivations are shown in the Appendix.

For a small elastic deformation, δ, assuming the tip deforms by δ_0 and the teeth deform by δ_1, where $\delta = \delta_0 + \delta_1$, equilibrium and kinematic analysis of the slant and tip interface yields

$$\sigma_{tip} = E_0^{PS}\varepsilon_{tip} = E_0^{PS}\frac{\delta_0}{g_0}; \tag{7a}$$

$$\sigma_{base} = E_1\,\varepsilon_{tooth} = E_1\,\frac{\delta_1}{A}; \tag{7b}$$

$$\tau_T = G_0\gamma_{slant} = G_0 \frac{\delta}{g} . \quad (7c)$$

Using Eqs. (2a, b) and Eqs. (7a-c), the normal stress across the tip region, σ_{tip}, can be expressed in terms of the axial stress at the base, σ_{base}, as

$$\sigma_{tip} = \frac{\tan\varphi - \frac{AG_0}{gE_1}\sec^2\beta}{\tan\varphi - \tan\beta + \frac{G_0\, g_0}{E_0^{PS}\, g}\sec^2\beta}\sigma_{base}, \quad (8)$$

where g_0 is the width of the tip interfacial region and g is the width of the slant interfacial region.

The effective stiffness $\bar{\bar{E}}_{tip,DTM}$ can be obtained by proper differentiation with respect to $\bar{\sigma}$, when σ_T, τ_T, σ_{base}, and σ_{tip} have all been given as a function of $\bar{\sigma}$. Hence, using Eq. (1), Eq. (2), Eq. (6a-d), and Eq. 8, the effective stiffness assuming deformable teeth can be expressed as

$$\bar{\bar{E}}_{tip,DTM} = [B_{slant} + B_{tip} + B_{tooth}]^{-1} \quad (9a)$$

where

$$B_{slant} = \frac{\partial^2(U_{slant})}{\partial\bar{\bar{\sigma}}^2} = f_s\left[\frac{(\sigma_T)^2}{E_0^{PS}} + \frac{(\tau_T)^2}{G_0}\right][\sigma_{base}\frac{t_{base}}{\lambda} + \sigma_{tip}\frac{t_{tip}}{\lambda}]^{-2}$$

$$B_{tip} = \frac{\partial^2(U_{tip})}{\partial\bar{\bar{\sigma}}^2} = f_t\left[\frac{(\sigma_{tip})^2}{E_0^{PS}}\right][\sigma_{base}\frac{t_{base}}{\lambda} + \sigma_{tip}\frac{t_{tip}}{\lambda}]^{-2}$$

$$B_{tooth} = \frac{\partial^2(U_{tooth})}{\partial\bar{\bar{\sigma}}^2} = 4\int_0^A \frac{\sigma_{yy}(y)^2}{E_1}\frac{w(y)}{V}dy\,][\sigma_{base}\frac{t_{base}}{\lambda} + \sigma_{tip}\frac{t_{tip}}{\lambda}]^{-2} \quad (9b)$$

and where $f_s = \frac{V_{slant}}{V}$, $f_v = \frac{V_{tooth}}{V}$, and $f_t = \frac{V_{tip}}{V}$. By excluding the contributions of the bonded tip: B_{tip} and $\sigma_{tip}\frac{t_{tip}}{\lambda}$ in B_{slant} and B_{tooth}, Eq. 9a degenerates into the case of an unbonded tip, the effective stiffness of which is given by (Li et al. 2013a)

$$\bar{\bar{E}}_{notip,DTM} = f_v\left[\left(\frac{1}{f_v} - 1\right)tan^2\theta\left(\frac{cos^2\beta\, sin^2\beta}{E_0^{PS}} + \frac{cos^4\beta}{G_0}\right) + \frac{\zeta(\beta,\theta)}{E_1}\right]^{-1} , \quad (10a)$$

where

$$\zeta(\beta,\theta) = \begin{cases} 1 & if\ \beta = \theta \\ \frac{2}{3}\frac{tan\theta}{tan\varphi} & if\ \beta = 0 \\ 2\frac{tan\theta}{tan\varphi}\left[0.5 - a + a^2 ln\left(1 + \frac{1}{a}\right)\right] & if\ \beta \in (-\theta, 0)\cup(0,\ \theta) \end{cases} , \quad (10b)$$

and where

$$a = \frac{tan\varphi}{tan\beta} - 1. \quad (10c)$$

Eqs. (9a,b) show the increased stiffness due to the bonded tip in comparison to Eqs. (10a,b,c). The bonded tips provide an additional contribution from the bonded interface and, inherently, also transfer more load to the tooth material making the teeth more effective contributors. Therefore, the effect of the bonded interface depends largely on β, which determines the volume fraction of the tip area and the stress distribution in the teeth. For example, the tooth material of a triangular suture is already fully engaged in load carrying without a bonded tip interface, and therefore no significant difference occurs by introducing a bonded tip. On the other hand, tip bonding significantly changes the behavior of the other suture geometries and depend strongly on β.

3.3.2 Tensile Strength

For a suture interface with a bonded tip area under tension, we expect two peaks in the stress-strain curve (Figure 3-3B). The first peak typically corresponds to the failure of the bonded tip interface, while the second peak corresponds to the failure of the slanted interfacial material or possibly the tooth material. The second peak is identical to the strength of a suture interface without a bonded tip area under tension.

The bonded tip interface is taken to fail using a maximum principal stress criterion. When the normal stress at the tip of the tooth, σ_{tip}, is equal to the strength of the interface material, σ_0^f, then failure is taken to initiate. Therefore, using Eq. (1) and Eq. (8), the far-field stress, $\bar{\sigma}$, can be expressed in terms of σ_{tip}. Taking $\sigma_{tip} = \sigma_0^f$, the effective suture strength of the first peak, $\bar{\sigma}_{tip}^{f-1st}$, due to tip interfacial material failure is derived as

$$\bar{\sigma}_{tip}^{f-1st} = f_v \sigma_0^f \left(\frac{\tan\varphi - \tan\beta + \frac{G_0 g_0}{E_0\, g}\sec^2\beta}{\tan\varphi - \frac{AG_0}{gE_1}\sec^2\beta} \frac{\tan\varphi}{\tan\theta} + \frac{\lambda - 2A\tan\varphi}{2A\tan\theta} \right) \tag{11}$$

where g is the slanted interface width, and g_0 is the tip interface width. For a given tooth tip angle, interface widths, and tooth volume fraction, the first term of the expression determines the effect of the bonded tip area. Once the tip fails the load will decrease until dropping to the load carrying ability of the suture with an unbonded tip. As strain is further increased, the load will rise to a second peak whereupon the slanted interface fails and is derived previously in Li et al. 2013a to be:

$$\bar{\sigma}_{tip}^{f-2nd} = \bar{\sigma}_{notip}^{f} = f_v \sigma_1^f \min\left[\bar{\sigma}_I,\ \bar{\sigma}_{II}\right], \tag{12a}$$

where $\bar{\sigma}_I$ and $\bar{\sigma}_{II}$ correspond to tooth failure and interface failure, respectively, using a maximum principal stress failure criterion and are derived as

$$\begin{cases} \bar{\sigma}_I = \frac{tan\varphi}{tan\theta}, & (tooth\ failure: \sigma = \sigma_1^f) \\ \bar{\sigma}_{II} = \frac{\sigma_0^f}{\sigma_1^f} \frac{tan\varphi}{tan\theta B(\varphi,\ \beta)}, & (interface\ failure: \sigma_0^P = \sigma_0^f) \end{cases} \tag{12b}$$

where

$$B(\varphi,\ \beta) = \frac{tan\varphi cos\beta}{2}\left[(1+v_0)sin\beta + \sqrt{(1-v_0)^2 sin^2\beta + 4cos^2\beta}\right], \tag{12c}$$

and where σ_1^f is the tooth strength.

3.3.2 Toughness

The tensile toughness of the suture interface with a bonded tip area is predicted as

$$\bar{\Gamma}^f = \Gamma_{tip}^f + \Gamma_{notip}^f \tag{13a}$$

where Γ_{tip}^f is the contribution from the energy dissipated from the bonded tip, and Γ_{notip}^f is the tensile toughness of a suture interface without a bonded tip area (Figure 3B). Because linear elasticity is assumed, Γ_{tip}^f and Γ_{notip}^f can be approximated by the resilience, such that

$$\bar{\Gamma}^f = \Gamma_{tip}^f + \Gamma_{notip}^f \approx \mu_{tip} + \mu_{notip} = \left(\frac{1}{2}\frac{\left(\bar{\sigma}_{tip}^f\right)^2}{\bar{E}_{tip}} - \frac{1}{2}\frac{\left(\bar{\sigma}_{tip}^f\right)^2 \bar{E}_{notip}}{\bar{E}_{tip}^2}\right) + \frac{1}{2}\frac{\left(\bar{\sigma}_{notip}^f\right)}{\bar{E}_{notip}} \tag{13b}$$

where μ_{tip} is the resilience of the tip interfacial layer and μ_{notip} is the resilience of the suture interface without a bonded tip area. This approximation only accounts for strain energy density in the linear elastic regime and does not account for the energy dissipated by material degradation during the post-peak failure process stage. To account for failure process energy dissipation, we would need to model the post-peak failure process (Figure 3B) represented by the negative slope S′, by adding an additional term, $\Gamma_{postfailure} = \frac{1}{2}\frac{\left(\bar{\sigma}^f\right)^2}{S'}$ that can be empirically determined and represents the contribution from the post-failure behavior. This toughness definition approximates the energy dissipation from the tip interface after its failure to be negligible. Because the deformation of the tip interface offers an additional energy dissipation mechanism in both teeth and interfacial layers, the toughness of a suture interface with bonded tip region will clearly have higher toughness than a suture interface without a bonded tip region.

3.4 Results and Discussion

3.4.1 Sutures with Bonded vs. Unbonded Tip Interfaces

The effect of bonded tips on the mechanical behavior of suture interfaces is explored by testing four representative geometries of $\theta = 22.6°$, $g = g_0 = 1\ mm$, and $f_s = 0.16$, with and without bonded tip interfaces, that span the range of general trapezoidal suture interfaces: anti-trapezoidal, rectangular, trapezoidal, and triangular. The volume fractions of the flat tip interface with respect to the total volume are 7.6%, 5.2%, 2.7%, and 0% for anti-trapezoidal, rectangular, trapezoidal, and triangular suture interfaces, respectively.

The engineering stress-strain curves of suture interfaces with and without a bonded tip region are shown in Figure 3-4A. The anticipated dramatic increase in stiffness due to the bonded tips is observed for the trapezoidal, anti-trapezoidal, and rectangular cases. These cases also exhibit double peaks in the stress-strain curves. The first peak corresponds to the failure of the tip interfacial region. A drop in stress is then observed until reaching the stress-strain curve of the corresponding suture interface which had not possessed a bonded tip. The second peak then coincides with the corresponding peak of the stress-strain curves of suture interface without flat tip material. The stress-strain curves of the triangular suture interface with and without bonded tips are essentially identical. Therefore, as assumed in the model, the experimental observation shows the failure of the bonded tip interface and slanted interface of the different geometries to occur independently. Indeed, as seen in Figure 3-4A, once the bonded tip failure occurs, the stress drops, and the stress-strain curves of the bonded and unbonded case are essentially identical.

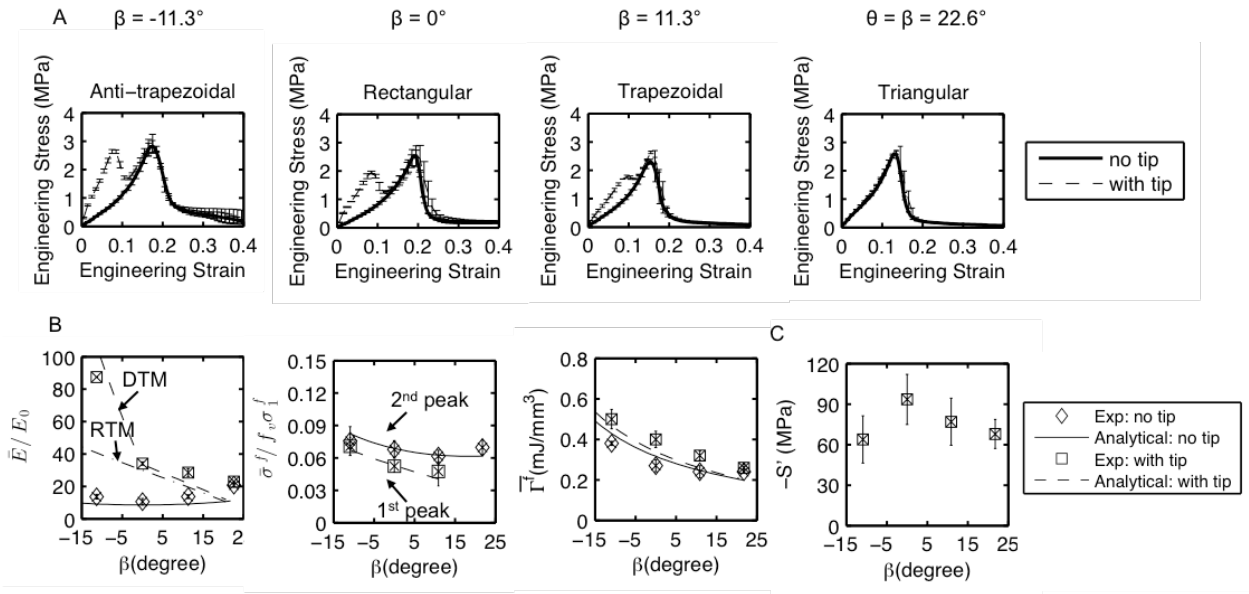

Figure 3-4 | Effect of tip interface on mechanical behavior of suture interfaces with different geometries for θ = 22.6° and f_s = 0.16. (A) Stress-strain behavior, (B) analytical and experimental results of non-dimensional effective stiffness and strength, toughness (C) post-failure slope. Error bars indicate standard deviation.

Experimental images taken *in situ* for an anti-trapezoidal suture interface of $\theta = 22.6°$ and $\beta = -11.3°$, with and without tip material (Figure 3-4), show that the first peak corresponds to the beginning of tip material failure, while the second peak corresponds to the beginning of material failure in the slanted interfacial layers. From a comparison of the two sets of images, once the tip material fails, the failure processes of those with a bonded tip and an unbonded tip are identical. This observation explains the coincidence of the stress-strain curves after the first peak for suture interfaces with and without tip material. In addition, this observation validates the analytical model, which treats the flat tip interface as independent of the slanted interface, and explains the good agreement between experiments and model prediction.

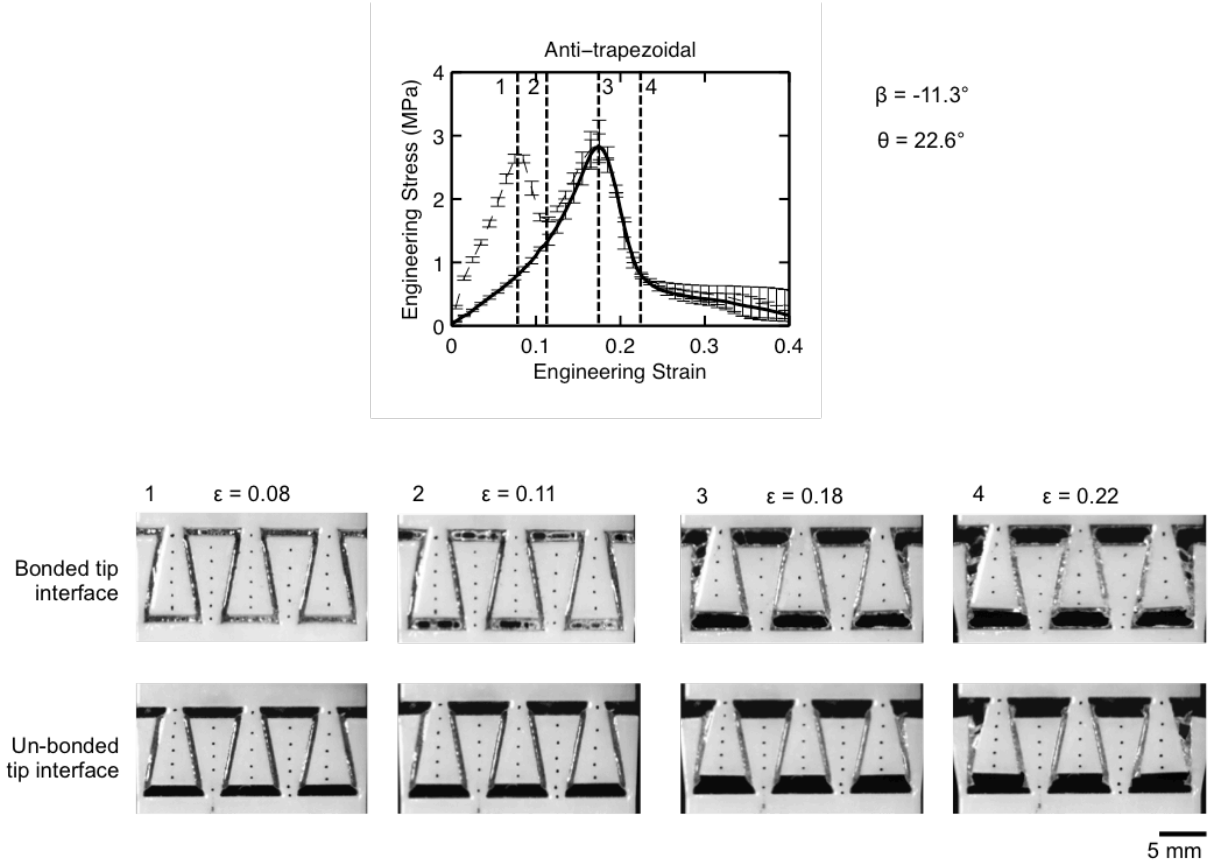

Figure 3-5 | Deformation of anti-trapezoidal suture interface with and without tip material. Optical images of suture interfaces with bonded and un-bonded tip interfaces at different strains under longitudinal tension. Error bars indicate standard deviation.

The analytical results for stiffness, strength, and toughness track the experimental result well as shown in Figure 3-4B. Hence, the models can be used to aid design of suture geometries, and we can utilize analytical models to further explore the interplay between the geometric and material parameters (Figure 3-6). The following sections discuss the effect of the bonded tip interface on stiffness, strength, toughness and failure mechanisms utilizing both experimental results and analytical predictions.

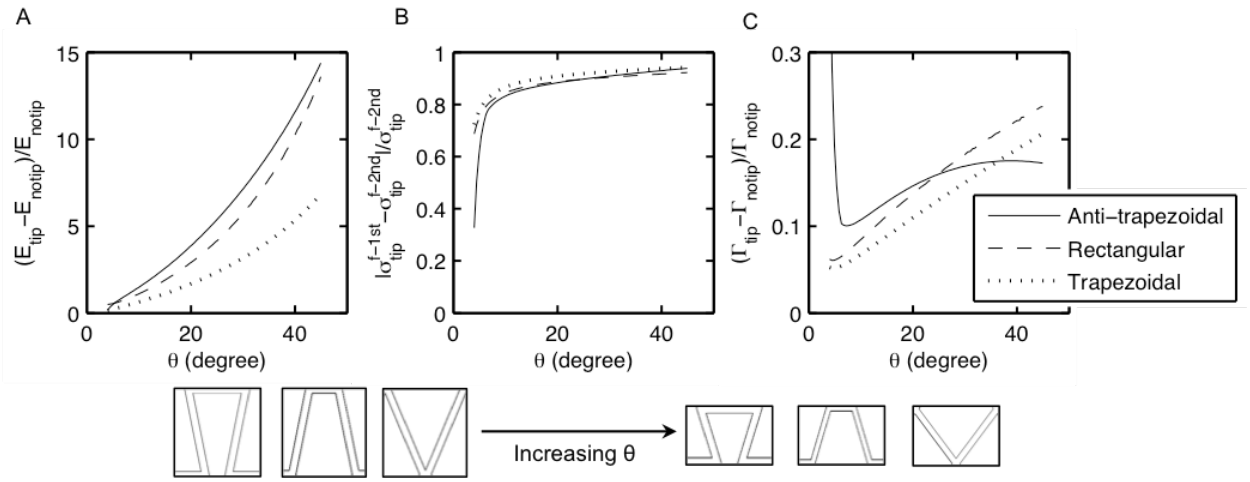

Figure 3-6 | Change in mechanical properties of suture interfaces with bonded tip region relative to suture interfaces with an unbonded tip region predicted by analytical model with a bonded tip angle. Change in (A) longitudinal stiffness, (B) tensile strength, and (C) toughness as a function of tip angle.

Stiffness: As seen in the stress-strain curves for suture interfaces without bonded tip interfaces, the triangular suture interface has the highest stiffness (Figure 3-4B). As derived in Li. et al. (2011, 2013), the triangular geometry uniquely, and therefore optimally, distributes stress uniformly across the teeth and interface, therefore resulting in high stiffness and strength. However, for the suture interfaces with bonded tips, the triangular suture interface has the lowest stiffness. The anti-trapezoidal suture interface with a bonded tip interface has the highest stiffness. This boost in stiffness is due to the additional contribution from the strain energy of the bonded interface as well as an increased load transfer to the teeth. This increase in load transfer to the teeth can be visualized by experimental strain contours shown by comparing the strain contours prior to tip failure (Figure 3-7A) and after tip failure (Figure 3-7B). Therefore, the stiffness is directly dependent on the tip angle and geometry, where the larger the tip interface region, the more significant the increase in stiffness. The effect of the tip material is much more significant in suture interfaces with a large tip angle—the anti-trapezoidal geometry shows an amplification of nearly 15 times the original stiffness as the tip angle approaches 45 degrees (Figure 3-6A). As shown by the analytical model, a larger tip interface volume fraction and smaller β will result in more dramatic changes in stiffness. This allows non-triangular suture geometries to transfer load to a greater fraction of the tooth material and hence to have higher stiffness than triangular suture interfaces. Because the material needed to fabricate a bonded tip interface may be insignificant relative to the slant interface, designing suture interfaces with bonded tip regions is a simple and cost-effective method to improve the stiffness.

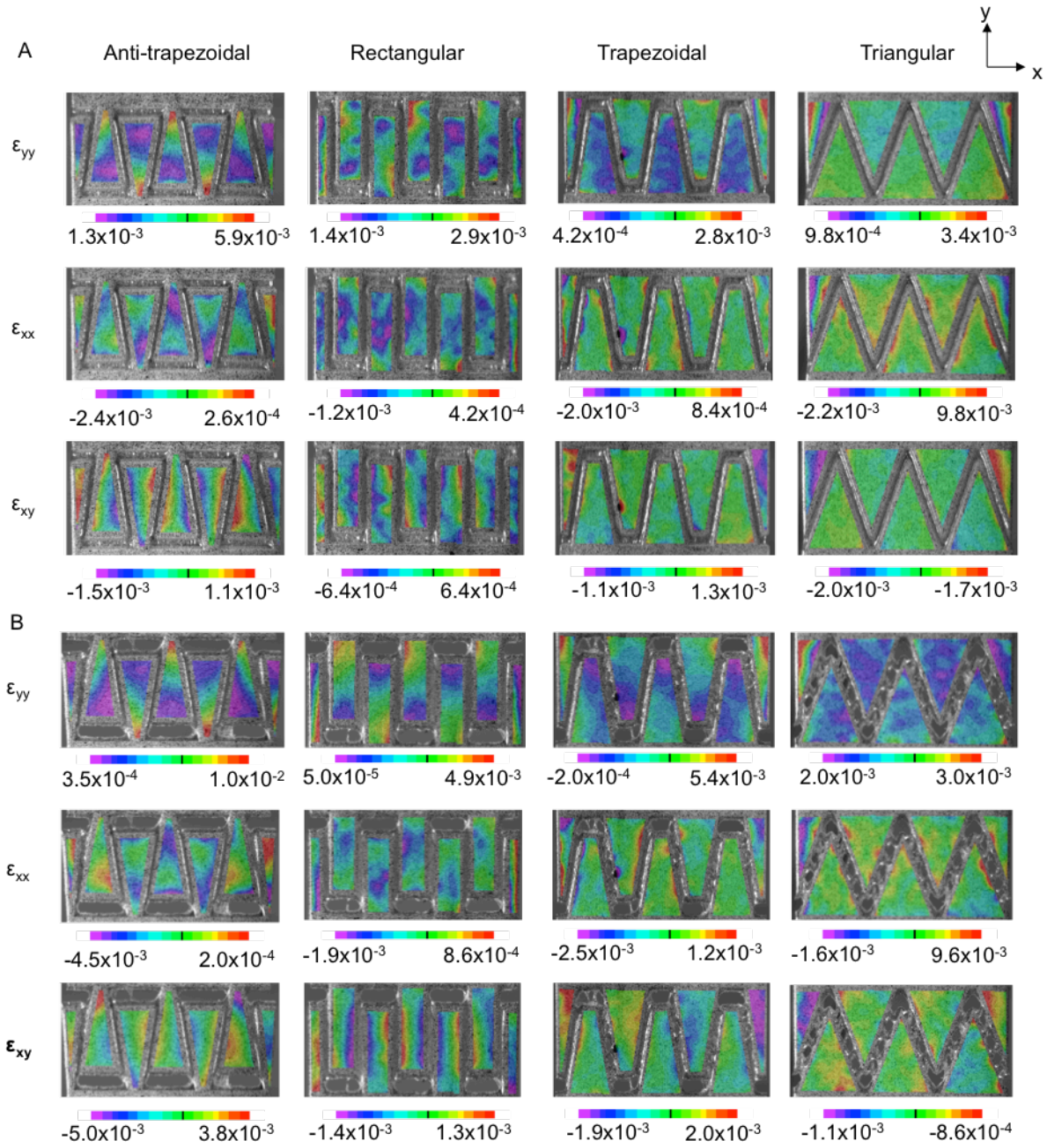

Figure 3-7 | Experimental strain contours of general trapezoidal suture interfaces using digital image correlation at a moment in tension. A) before tip interface failure and B) after tip interface failure.

Tensile strength: The maximum tensile strength of a suture interface with a bonded tip does not change relative to that of a suture interface with an unbonded tip. However, in addition, and prior to, the common peak in stress, a suture interface with a bonded tip has an additional peak in stress. For all geometries, the tip angle influences the strength of this first peak similarly, with small tip angles showing a small effect, and a steep

increase in effect when the tip angle increases from 5 degrees to 10 degrees. Because of this additional peak, the load-carrying capacity at any given strain of a suture interface with a bonded tip is equivalent or greater than that of a suture interface with an unbonded tip. Designing suture interfaces with bonded tip regions is an easy way to improve the overall load-bearing capacity of non-triangular geometries, especially at small strains.

Toughness and failure mechanisms: The bonded tip also allows for an additional energy dissipation mechanism for both the tip interface region and the teeth, therefore increasing the overall toughness. Similar to stiffness, the increase in toughness is dependent on geometry, with the most significant increase in anti-trapezoidal geometries, which have the largest tip interface region, when the tip angle is less than 25 degrees, and the most significant increase in rectangular geometries when the tip angle is greater than 25 degrees. At smaller tip angles, the increase in strength is more significant than the increase in stiffness in anti-trapezoidal geometries, resulting in a larger increase in toughness. The double peak nature of the failure process gives a damage tolerance feature to the structure because there is a recovery of load bearing after the first failure event. This damage tolerance feature is an important asset in natural materials, some of which have the ability to "self heal," since the constituent components remain in physical proximity after the first failure event, thus permitting healing so material regeneration can occur.

Experimental results in Figure 3-4C show that the failure process slope, S', depends on geometry (Figure 3-4C). The anti-trapezoidal geometry and triangular have the lowest S', and the rectangular geometry has the highest S'. The rectangular geometry is a simple shearing failure process whereas the slanted interface of the geometries is experiencing both a shearing and a normal stress, which further contributes to the failure stress and the failure process. The failure process of the different geometries will be discussed in more detail in the non-bonded tip cases of the next section. The post-peak failure process determines the energy dissipation due to interfacial material degradation and has a significant influence on the overall toughness of these particular suture interfaces due to how the particular constituent material behaves.

2.4.2 Sutures with Non-Bonded Tip Interfaces: Effect of Tip Angle (θ) and Geometry (β)

The effect of tip angle (θ) and geometry (β) on mechanical behavior and properties of suture interfaces is further examined for the case of non-bonded tip interfaces as shown in Figures 3-8 and 3-9 and discussed below.

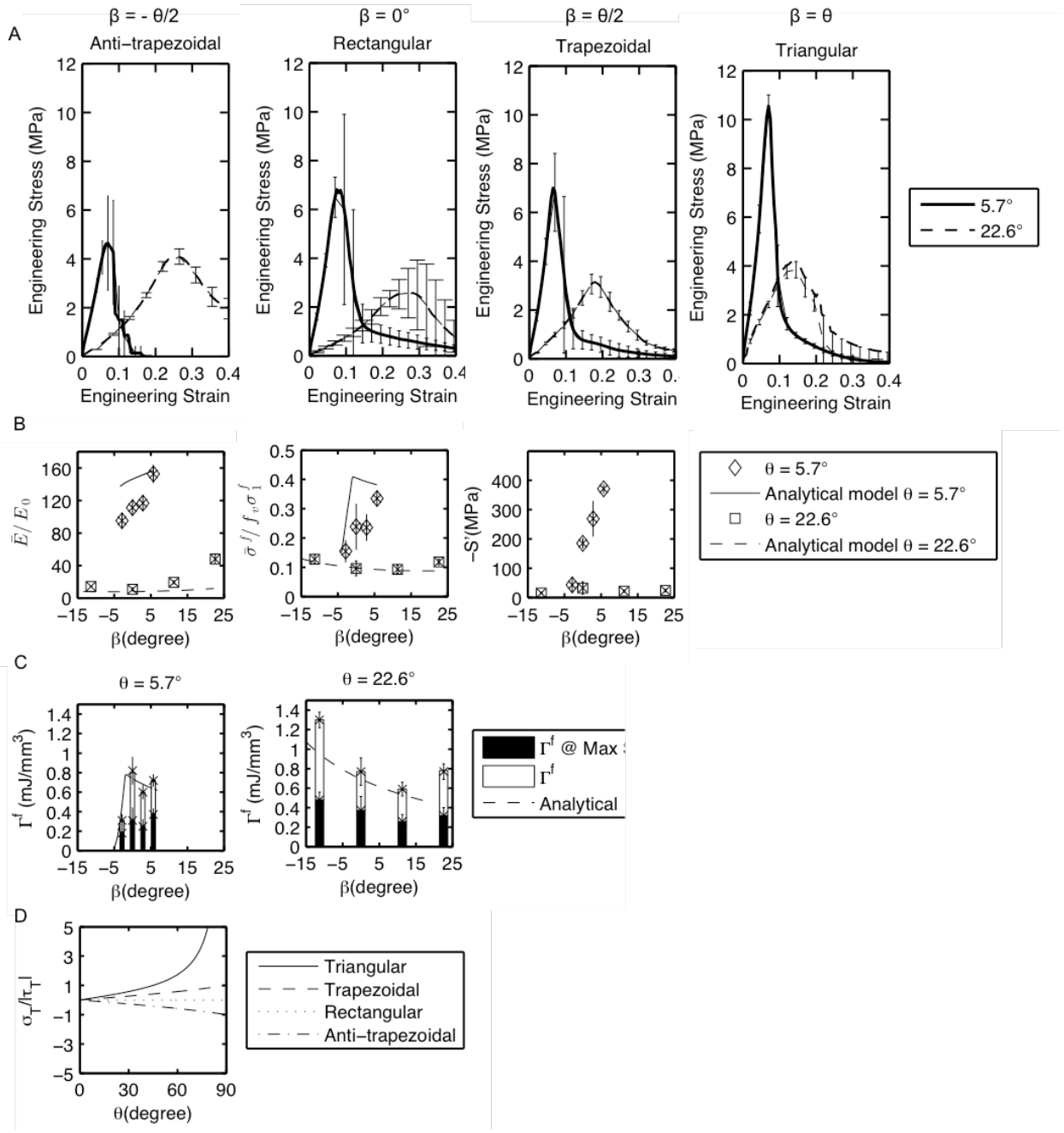

Figure 3-8 | Effect of tip angle and geometry on mechanical behavior of suture interfaces with unbonded tips. (A) Stress-strain behavior, (B) non-dimensional effective stiffness and strength, and post-failure slope, (C) resilience and total toughness, (D) interfacial normal stress and shear stress ratio as a function of tip angle. Error bars indicate standard deviation.

2.4.2.1 Effect of Tip Angle

There is a clear dependence of stress-strain behavior on tip angle as seen in Figure 8 which compares the case of $\theta = 5.7°$ to that of $\theta = 22.6°$. All samples have interface

width $g = g_0 = 0.5\ mm$, and $f_s = 0.25$. Smaller tip angles correspond to higher stiffness and strength; stiffness and strength also increase as β increases (i.e. are greatest for triangular sutures and smallest for anti-trapezoidal sutures). These results follow the model predictions.

The strength and failure process can be further understood by considering the ratio of the interfacial normal stress to interfacial shear stress in Figure 3-8D, by examining images of the deformation and failure process shown in Figure 3-9, and by examining the tooth strain contours of Figure 3-7B. The ratio of normal stress to the magnitude of the shear stress in the interfacial layer, $\frac{\sigma_T}{|\tau_T|} = \tan\beta = \tan(c\theta)$, where c is a constant determined by the geometry: $c = 1$ for triangular, $c = \frac{1}{2}$ for trapezoidal, $c = 0$ for rectangular, and $c = -\frac{1}{2}$ for anti-trapezoidal. The rectangular sutures have a simple shear condition; the anti-trapezoidal case undergoes interface shear and a compressive normal stress; the trapezoidal and triangular suture interfaces undergo interface shear and a tensile normal stress.

For the case of $\theta = 5.7°$, the anti-trapezoidal strength is governed by tooth failure due to the high stress concentration at the tooth base (see the strain contours of Figure 3-7); the rectangular suture failure is governed by interface shear; the trapezoidal and triangular suture failure are governed by both interface shear and a tensile interface normal stress which also leads to progressive periodic cavitation events and subsequent stretching of the remaining interface ligaments. The formation of periodic cavitations is clearly shown in Figure 9B, where $\theta = 21.8°$, and $f_v = 0.92$. For the case of $\theta = 22.6°$, the anti-trapezoidal failure is interfacial due to the combination of shear and normal stress as opposed to the tooth failure observed for $\theta = 5.7°$; for the other geometries similar failure events are observed with a more graceful post-peak failure process in all cases.

For the triangular suture, when $\theta = 5.7°$, $\frac{\sigma_T}{|\tau_T|} = 0.1$, and when $\theta = 22.6°$, $\frac{\sigma_T}{|\tau_T|} = 0.4$, the ratios of normal stress to shear stress in the interfacial layer govern the stress initiation at failure, the periodicity of cavitations, and the shearing and stretching and final failure of the remaining interface ligaments. The interface failure process is observed to be one of an initial cavitation event, followed by a shear lag load transfer to the remaining intact interface, followed by another cavitation event, leading to a periodicity of cavitation events. The remaining ligaments (i.e, the interfacial ligaments between the cavitation events) then shear and stretch until final failure.

The post-peak strength failure processes of the suture interfaces are further quantified using S', a measure of the failure process. Suture interfaces with the larger tip angle have a much lower S', indicating a more graceful failure mechanism. For suture interfaces with a smaller tip angle, S' increases dramatically with β. The geometry and tip angle govern the shear and normal stresses in the interfacial layer as discussed above which in turn govern the post-strength S' and failure process.

2.4.2.2 Effect of Geometry

For a given tooth tip angle, the geometry of the suture interface influences the overall stiffness, strength, and toughness. However, the magnitude of the effect of geometry is dependent on the tip angle. In general, the geometry has larger effect when the tip angle is smaller.

Stiffness: It is possible to fine-tune the stiffness of a suture interface with a large tip angle by switching between the different geometries. The higher sensitivity to changes in geometry observed at smaller tip angles results from the decrease in tooth material loaded for anti-trapezoidal and trapezoidal geometries. For all tip angles, the triangular geometry amplifies the stiffness significantly. Here, the analytical model captures the general effect of the geometry. However, the analytical model predicts a stiffness that is higher than experimentally determined for small angle suture interfaces. This can be understood by the small cross-sectional area of the root of the teeth for non-triangular geometries that will make the suture interfaces less stiff than expected due to slight in-plane bending of the teeth at smaller tip angles as seen in Figure 3-9A.

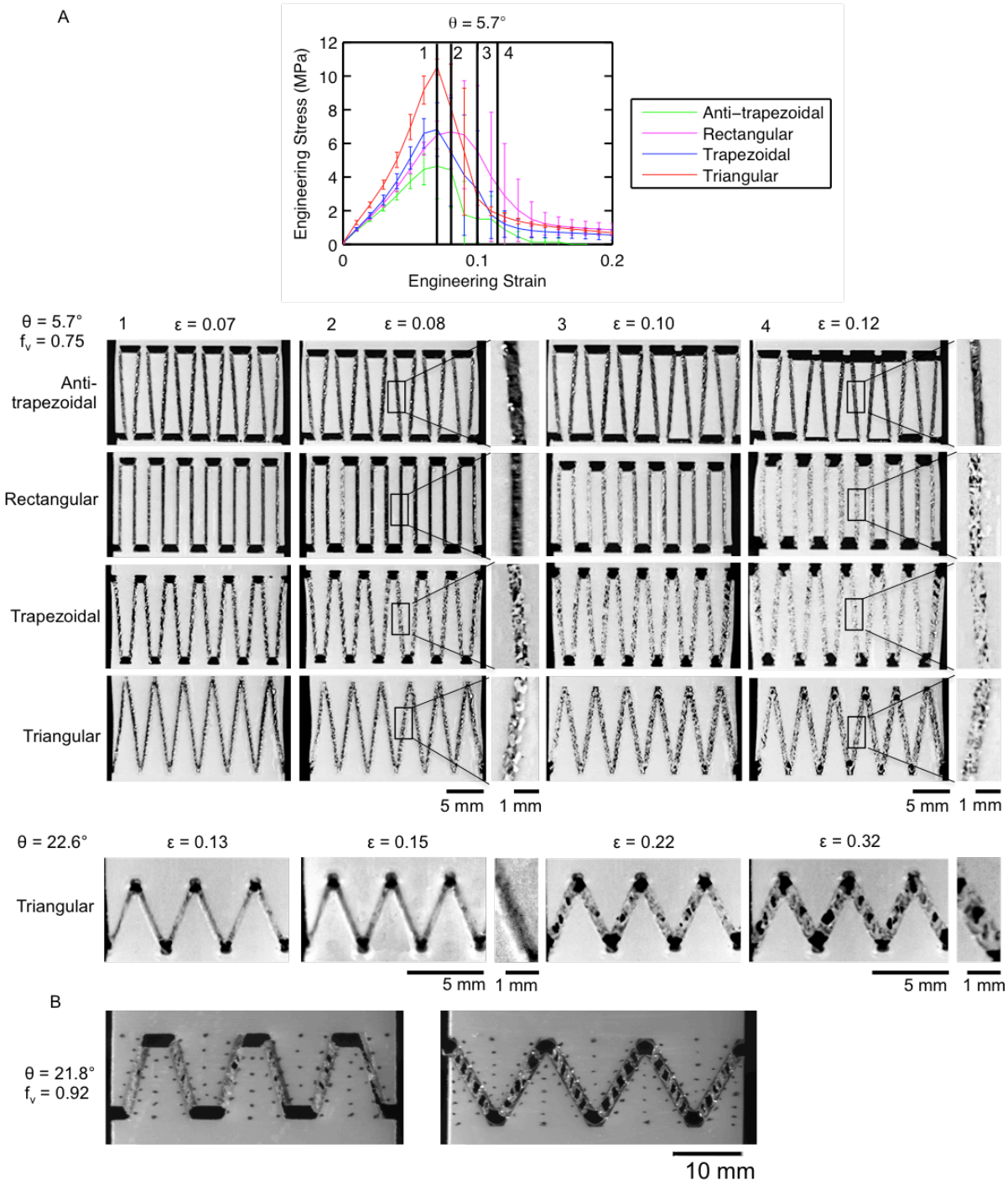

Figure 3-9 | Deformation of anti-trapezoidal, rectangular, and trapezoidal suture interfaces at θ = 5.7°, and triangular suture interfaces at θ = 5.7° and θ = 22.6°. A) Optical images of suture interfaces with unbonded tip interfaces at different strains under longitudinal tension. B) Periodic cavitations in trapezoidal and triangular suture interfaces at θ = 21.8° and f_v = 0.92.

Tensile strength: The dependence of strength on tip angle and geometry is similar to that of stiffness, where the tip angle governs the broad range of possibilities, and geometry dictates the specific strength of the design. The triangular suture interface has the largest strength at both tip angles. For strength, the failure mechanism is highly important. The tip angle and the geometry greatly influence whether the suture interface design fails by interface failure, tooth failure, or both. Smaller tip angles and anti-trapezoidal suture geometries are more likely to fail by tooth failure, due to the small cross-sectional area of the base of the teeth. This results in high stress concentrations at the teeth base and the strength of suture interfaces drops dramatically. The analytical model accurately predicts the tensile strength for large tip angles, but differs for suture interfaces with the smaller tip angles. The peak in the analytical model for the smaller tip angle corresponds to the point at which tooth and interface failure are expected to occur simultaneously, resulting in high strength. However, in the experiment, only interface failure occurs. This discrepancy can be understood by the slight expansion in the x-direction of the suture interface as seen in Figure 3-9A, which relieves some of the stress from the teeth, therefore resulting in only interface failure and lower strength.

Toughness and failure mechanisms: Toughness depends on the stiffness, strength, and post-failure process. The tip angle and geometry influence the interfacial normal to shear stress ratio, which in turn dictates the interfacial layer failure initiation and subsequent failure process. As mentioned before, the ratio between interfacial normal stresses and shear stresses influences the interfacial layer failure process. The rectangular suture interfaces fails simply due to shear stresses, while the other geometries fail due to a combination of normal and shear stresses. Looking at the toughness at maximum stress and the total toughness, it can be seen that the post-failure energy dissipation is an important contribution to the total toughness, regardless of geometry (Figure 3-8C). For the small angle trapezoidal and triangular cases, failure occurs due to the periodic cavitation events followed by the shearing and stretching of the remaining ligaments giving a higher S'. Although the triangular geometry has a steeper post-failure slope (S'), there is a graceful failure regime after the initial drop in load-bearing capacity. This regime is due to the ductile failure of the interface. The graceful failure regime significantly contributes to the total toughness. In addition, tooth failure is more likely to occur in suture interfaces with small tip angle or in the anti-trapezoidal and rectangular suture interfaces, in which there are high stress concentrations at the base of the teeth due to a smaller cross-sectional area. Suture interfaces that fail by tooth failure (small tip angles or anti-trapezoidal geometries) are more brittle and allow for much less energy dissipation, resulting in a lower toughness. However, because an anti-trapezoidal geometry is inherently interlocking, if the tip angle is large enough, the post-failure process is more graceful, resulting in higher

toughness, analogous to the increased toughness due to interlocking platelets shown in nacre ([37,38]). Experimentally, tooth failure occurs in a single tooth at a time, in which the strain localizes immediately prior to failure. In general, tooth failure results in catastrophic and less graceful failure.

The effect of geometry can be further quantified by looking at the strain distributions in the teeth of the suture interface under tension (Figure 3-7B). Although the tooth strain contours are of suture interfaces with a bonded tip interfacial layer, the previous section has established that after tip interface failure, the stress-strain behavior is identical to suture interfaces with an unbonded tip interfacial layer and therefore can be used in this section to explore the effect of geometry. The anti-trapezoidal suture interface has significantly non-uniform strain distribution, with high strain concentration at the base of the tooth. With an increase in β, the strain distribution becomes more uniform, with the triangular suture interface showing remarkable uniform strain distribution. This corresponds with the analytical and finite element results shown by Li et. al. (2013), where the triangular geometry is shown to provide a uniform stress distribution in both teeth and interfaces.

2.5 Conclusion

The dependence of the stiffness, strength, and toughness of suture interfaces on geometric parameters and material constituent properties was found through analytical modeling and experiment. By tailoring the geometric parameters, including having an unbonded or bonded tip region, tip angle, and geometry, a range of mechanical behaviors can be achieved. As shown in Table 3-1, for each property the underlying mechanism that improves the property corresponds to certain optimal geometric parameters. To improve stiffness, a bonded tip and decreased tip angle can result in additional strain energy and increased load transfer to teeth; to improve strength, decreased tip angle can result in simultaneous tooth and interface failure or the triangular geometry can increase the ratio of interfacial normal stress to shear stress; to improve toughness, larger tip angles can result in ductile failure of the interface or anti-trapezoidal geometries can result in interlocking of the teeth. In summary, for many purposes the triangular geometry is optimal, allowing for high stiffness, strength, toughness, and high integrity due to its ability to uniformly distribute stress. However, the anti-trapezoidal suture interface is also desirable, due to its high stiffness, strength and toughness when possessing an initially bonded tip interface; the anti-trapezoidal geometry also exhibits a damage tolerance due to increased strain to failure as well as mechanical interlocking.

Table 3-1. Summary of underlying mechanisms and optimal geometric parameters for improved stiffness, strength, and toughness.

	Improved stiffness	Improved strength	Improved toughness
Underlying mechanism	Additional strain energy; increased load transfer to teeth	Simultaneous tooth and interface failure; high ratio of interfacial normal stress to interfacial shear stress	Ductile failure of interface; interlocking of teeth
Optimal geometric parameters	Bonded tip; decreased tip angle	Decreased tip angle; triangular geometry	Increased tip angle; anti-trapezoidal geometry

Careful consideration of suture interface geometry is a simple, yet powerful, way to precisely tailor effective mechanical behavior—through small changes, the stiffness, strength, toughness, and failure mechanisms can be designed to fit particular needs. The geometry, which is described by the presence or absence of bonded or unbonded tip regions, the tip angle, and the shape factor, determines the contributions of interfacial layer and teeth deformation, the transfer of load across the interfaces, the stress distributions in the teeth, and the amount of tooth material carrying load, which in turn influence the stiffness, strength, toughness, failure mechanisms, damage tolerance, and integrity. From this understanding of the role of geometry in its mechanical behavior, suture interfaces could be carefully designed to be bio-inspired materials for a range of applications. In particular, the analytical model presented can serve as an important tool in the design of suture interfaces for easy optimization of designs given an application.

4 Bio-inspired hierarchical suture interfaces

This chapter was published as an article in the *Journal of Materials Research* in 2014.

4.1 Introduction

Additive manufacturing, with its ability to rapidly fabricate complex geometries, has emerged as a useful approach for prototyping and understanding the mechanical behavior of new material designs [33-35,39]. Materials in nature often possess complex geometries that are critical for their mechanical performance (wainwright) [30,40,41], and therefore the use of additive manufacturing for prototyping bio-inspired materials designs is a particularly powerful experimental research platform. These complex geometries are often hierarchical, both across[42,43] and within[7,18] length scales. Hierarchical designs within a given length scale consists of intricate, fractal-like patterns with repeating self-similar geometries, and have been shown to contribute significantly to the mechanical properties of natural materials[5,44].

One particularly fascinating example of hierarchical design in nature are suture interfaces, which consist of interdigitating stiffer components, or teeth, joined by a compliant interfacial layer[4,5,7,9,18,20]. Suture interface geometries vary significantly both across species, ranging from the triangular waveform of the three-spined stickleback[10] to the intricate, hierarchical designs of ammonites[6,12]. As shown in Fig. 1(a), even within ammonites, suture interfaces exhibit various geometries, from simple curves to complex, hierarchical geometries[7,45,46].

We have recently shown through analytical models that simple changes in first order geometries and frequency of suture interfaces without any hierarchical designs can finely tune the stiffness, strength, toughness, and failure mechanisms of the overall structure[4,11,24]. In addition, we have shown through analytical models that the hierarchical design of suture interfaces can be used to tailor and amplify mechanical properties nonlinearly[12]. Here, we further explore the role of hierarchy in mechanical behavior through direct mechanical testing on additively manufactured prototypes. Through the use of prototyping by 3D-printing, not only can the influence of hierarchical geometry on mechanical behavior, including stiffness, strength, and toughness be experimentally determined, but also the failure mechanisms and post-failure behavior can be investigated. In addition, through direct mechanical testing of 3D-printed prototypes, the mechanical behavior of additively manufactured materials can be further explored and understood.

In this chapter, we experimentally investigate the stiffness, strength, toughness, and failure mechanisms of hierarchical suture interfaces by utilizing additive manufacturing to create physical prototypes. Bio-inspired design principles are extracted and hierarchical designs are explored as a method of expanding the range of mechanical behaviors that additively manufactured materials possess. Through this study, a deeper understanding of structure/property relationships of geometrically structured, multi-material, additively manufactured prototypes is also elucidated.

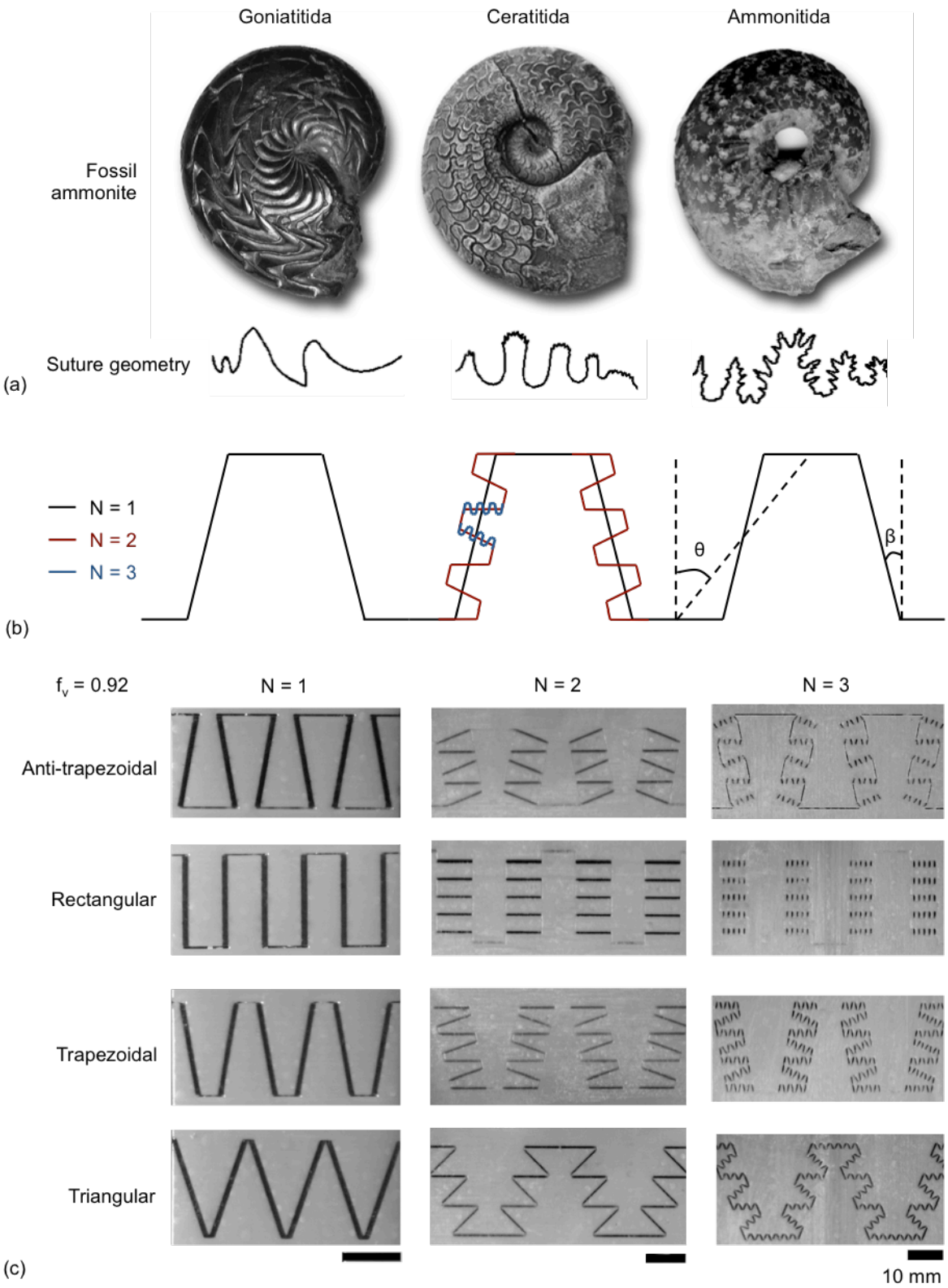

Figure 4-1 | Ammonite-Inspired design of hierarchical suture interfaces. (a) Photographs illustrating the progressive increase in Ammonite suture structural complexity, (b) Schematic of hierarchical suture interface design, (c) Optical images of 3D-printed prototypes of anti-trapezoidal, rectangular, trapezoidal,

and triangular suture interfaces with N = 1, 2, and 3 at a volume fraction, f_v, of 92%. (Images in (a) adapted from Wikimedia Commons)

3.2 Materials and Methods

Hierarchical suture interfaces with four geometries (anti-trapezoidal, rectangular, trapezoidal, and triangular) and three orders of hierarchy (N = 1, 2, and 3) were designed. The four geometries were general trapezoidal geometries introduced in Li et al. (2012), that are defined by the relationship between the shape factor, β, and tip angle, θ, shown in Fig. 4-1(a): anti-trapezoidal if $-\theta < \beta < 0$, rectangular if $\beta = 0$, trapezoidal if $0 < \beta < \theta$, triangular if $\beta = \theta$. All fabricated suture interface designs have $\theta = 21.8°$, and $\beta = -\theta/2$ and $\beta = \theta/2$ for anti-trapezoidal and trapezoidal geometries, respectively. Higher order hierarchical designs were created by iteratively superimposing self-similar waveforms on the slant interfaces of former suture interface profiles, as shown in Fig. 4-1(a). A tooth volume fraction, f_v, of 92% and an interface width of 0.5 mm were maintained for all designs. The major teeth were defined as the teeth of the first-order suture interface profile, while the minor teeth were defined as the teeth corresponding to higher order suture interface profiles.

The hierarchical suture interface prototypes were designed within Solidworks (Dassault Systemes, 2013) and fabricated via multi-material additive manufacturing (Stratasys Ltd., USA) as shown in Fig. 4-1(b). VeroWhite, an acrylic-based photo-polymer, was utilized for the teeth, and TangoPlus, a rubber-like compliant material, was used for the interfacial layer. The Young's moduli of TangoPlus (E_0) and VeroWhite (E_1) were previously determined to be 0.63 +/- 0.02 MPa and 2.0 +/- .09 GPa, respectively. In addition, the tensile and shear strength were previously determined to be 1.8 +/- 0.94 MPa and 1.4 +/- 0.11 MPa, respectively, for an interfacial layer of 0.5 mm ([24]). These material properties were used for the analytical predictions of the various suture interfaces and primary failure modes were found to be cohesive failures within the interfacial layer.

Three samples of each geometry were mechanically tested with a Zwick mechanical tester (Zwick Z010, Zwick Roell, Germany) under longitudinal tension at a constant strain rate of 0.05 s^{-1} for force-displacement measurements. Speckle patterns were created with an airbrush and a video extensometer in conjunction with digital image correlation (DIC) software:VIC-2D (Correlated Solutions, Inc, 2009) was used to calculate the local strain in the suture area. After mechanical testing, the fractured samples were sputter coated with gold and examined by scanning electron microscopy (SEM).

4.3 Results

The different geometries and orders of hierarchy (N) resulted in a wide range of mechanical behaviors as seen in Fig. 4-2. In this paper, we focused on the stiffness, strength, toughness, and failure mechanisms of the hierarchical suture interfaces under longitudinal tension. In the following section, the influence of order of hierarchy on the mechanical behavior of suture interfaces with different geometries are discussed in detail.

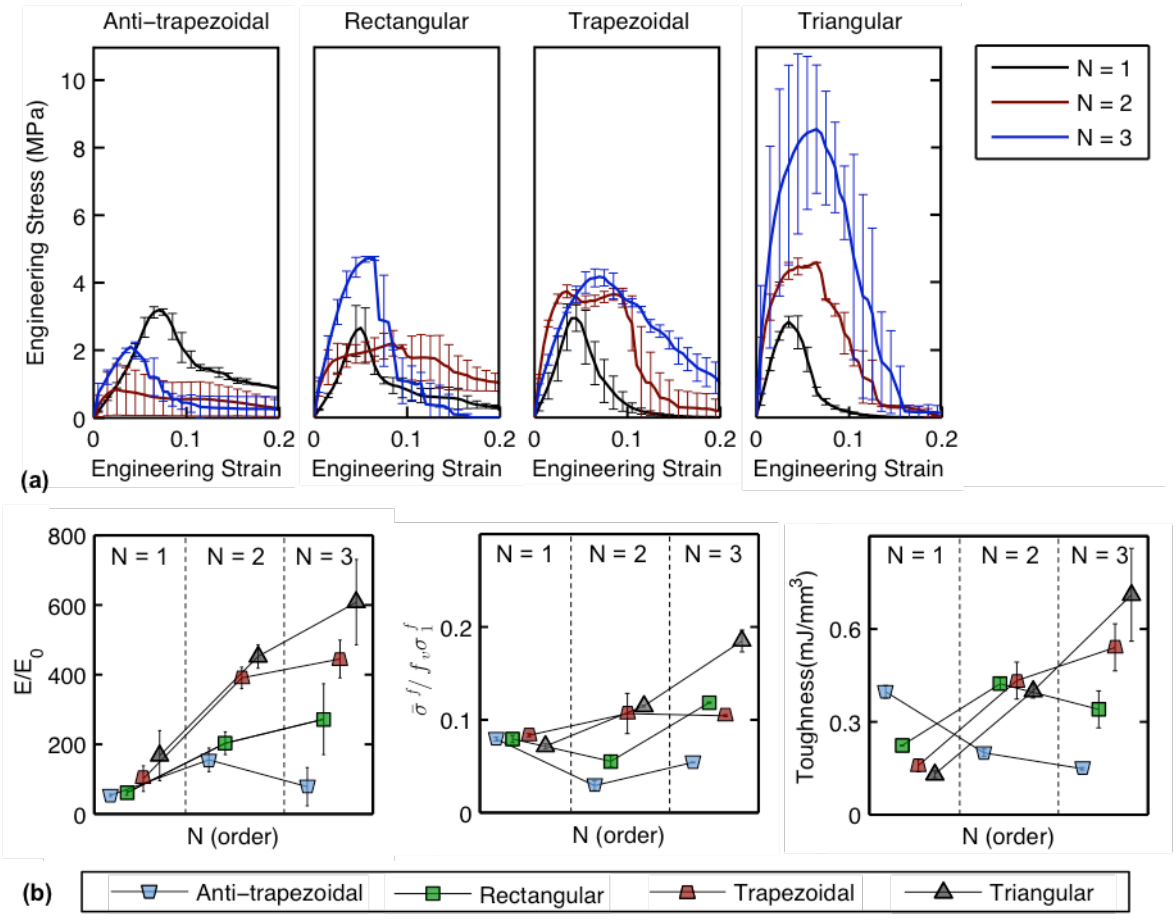

Figure 4-2 | Mechanical behavior of hierarchical suture interfaces under longitudinal tension. (a) Engineering stress-strain curves of hierarchical suture interfaces, (b) Non-dimensional effective stiffness and strength, and toughness with respect to N. Error bars indicate the standard deviation

3.3.1 Stiffness

With the four geometries and three orders of hierarchy, stiffness increases over an order of magnitude, from the least stiff first-order anti-trapezoidal suture interface to the stiffest third-order triangular suture interface. For all values of N, the anti-trapezoidal

geometry had the lowest stiffness, followed by the rectangular, trapezoidal, and triangular geometries with increasing stiffness. Increasing the order of hierarchy amplified the effect of geometry on stiffness. For N=1, the stiffnesses were more similar to each other (ranging from 37 MPa to 115 MPa), with the triangular geometry possessing a stiffness approximately three times that of the anti-trapezoidal geometry. With increasing N, the stiffness difference between the various geometries became more pronounced, ranging from 54 MPa to 419 MPa and with the triangular geometry possessing a stiffness over six times that of the anti-trapezoidal geometry. Considering that the stiffness of an Nth hierarchical suture interfaces depends on the tensile and shear modulus of the $(N-1)$th hierarchical suture interface[12], a small difference in stiffness between two geometries at N = 1 can easily become significant at N = 3.

For all geometries except the anti-trapezoidal geometry, the stiffness was highest at N = 3, with the triangular geometry showing a stiffness three times greater than the first-order triangular suture interface. With an increased order of hierarchy, two opposing factors influenced the stiffness: the increased order of hierarchy resulted in a stiffness amplification due to an increased effective stiffness of the first order interfaces, while maintaining a constant overall volume fraction resulted in a decreased stiffness due to the reduction of the building block (minor teeth) volume fraction[12]. For the rectangular, trapezoidal, and triangular geometry, the amplification from increasing the order of hierarchy was greater than the decrease from a reduction of building block volume fraction. However, for the anti-trapezoidal geometry, there was a peak at N = 2. The more significant effect from the lowering of building block volume fraction was due to the small cross-sectional area of the anti-trapezoidal geometry at the base of its teeth, and hence a decreased volume of tooth material under mechanical load.

3.3.2 Tensile Strength

The tensile strength was taken to be the maximum stress that the suture interface undergoes under tension. When N = 1, all geometries exhibited similar strengths, the maximum strength was within 17% of the minimum strength; this strength then increased when N = 2 for the triangular and trapezoidal geometries and decreased for the rectangular and anti-trapezoidal geometries, resulting in a range of strengths of over 250% of the minimum strength. From N = 2 to N = 3, the strength of all geometries increased.

Depending on the failure mechanism, the strength corresponded to the stress at interfacial layer failure, tooth failure, or both simultaneously, whichever occurred first. Regardless of the failure mechanism leading to catastrophic failure, interfacial layer failure was observed to occur first in all samples. Therefore, the change in strength can

be explained by the failure mechanisms of the interface, which are governed by the ratio of interfacial normal stress to interfacial shear stress. This effect was seen most clearly in the rectangular geometry. For $N = 1$ and at $N = 3$, the interfacial layer failed by shearing, while for $N = 2$, the interfacial layer failed due to normal stresses. Therefore, the strength of first-order and third-order rectangular suture interfaces were higher than that of second-order rectangular suture interfaces. Anti-trapezoidal suture interfaces followed a similar trend. On the other hand, there was no decrease in strength for trapezoidal and triangular geometries at $N = 2$. For these geometries, the larger cross-sectional area of the tooth base of the minor teeth provided for greater load bearing before the initial onset of failure.

3.3.3 Toughness

The influence of the order of hierarchy on tensile toughness (defined here as the total area under the stress-strain curve until complete failure) differed across geometries, with the triangular and trapezoidal exhibiting maximum toughness at $N = 3$, the rectangular at $N = 2$, and the anti-trapezoidal geometry at $N = 1$. For the anti-trapezoidal geometry, increasing N decreased the toughness, and it possessed the highest toughness relative to the other geometries at $N = 1$ due the interlocking of its teeth. This interlocking became less significant at higher N, since the failure of the minor and major teeth occurred before significant interlocking of the teeth. For the rectangular geometry, the toughness peaked at $N = 2$ with the other orders of hierarchy exhibiting similar toughnesses. At $N = 2$, the rectangular geometry required the failure of almost all of the minor teeth before catastrophic failure, greatly increasing the toughness. For both the trapezoidal and triangular geometry, the toughness increased with an increase in N, although the triangular geometry has a more significant increase in toughness with each increase in N. For the trapezoidal geometry, at $N = 2$, the suture interface was able to bear loads close to its maximum load-bearing capacity for some strain before failing, as seen in the plateau of the stress-strain curve. For $N = 3$, graceful failure, a result of significant interfacial layer and minor teeth failure occurring before catastrophic failure, resulted in an increase in toughness. The triangular geometry exhibited an increased stiffness, strength, and strain at maximum load-bearing capacity, and graceful failure with an increased N that all contributed to its significant increase in toughness.

3.3.4 Failure Mechanisms

As mentioned above, graceful failure is an important contribution to the increase in toughness of suture interfaces since the majority of the energy dissipation of hierarchical suture interfaces comes from post-failure mechanisms. As shown in Fig. 4-3, suture interfaces failed through major tooth failure, minor tooth failure, and

interfacial layer failure. First order suture interfaces failed mainly through interfacial layer failure. When $N = 2$, both interface failure and minor tooth failure occurred, with major tooth failure in the triangular geometry. For $N = 3$, interface failure, minor tooth failure, and major tooth failure all played a part in the failure mechanisms. While for $N = 1$, the anti-trapezoidal geometry is the only interlocking geometry, so for higher orders of hierarchy, interlocking is an inherent result of the geometry. As a result, the suture interfaces exhibited damage tolerance, where interface failure alone did not result in catastrophic failure.

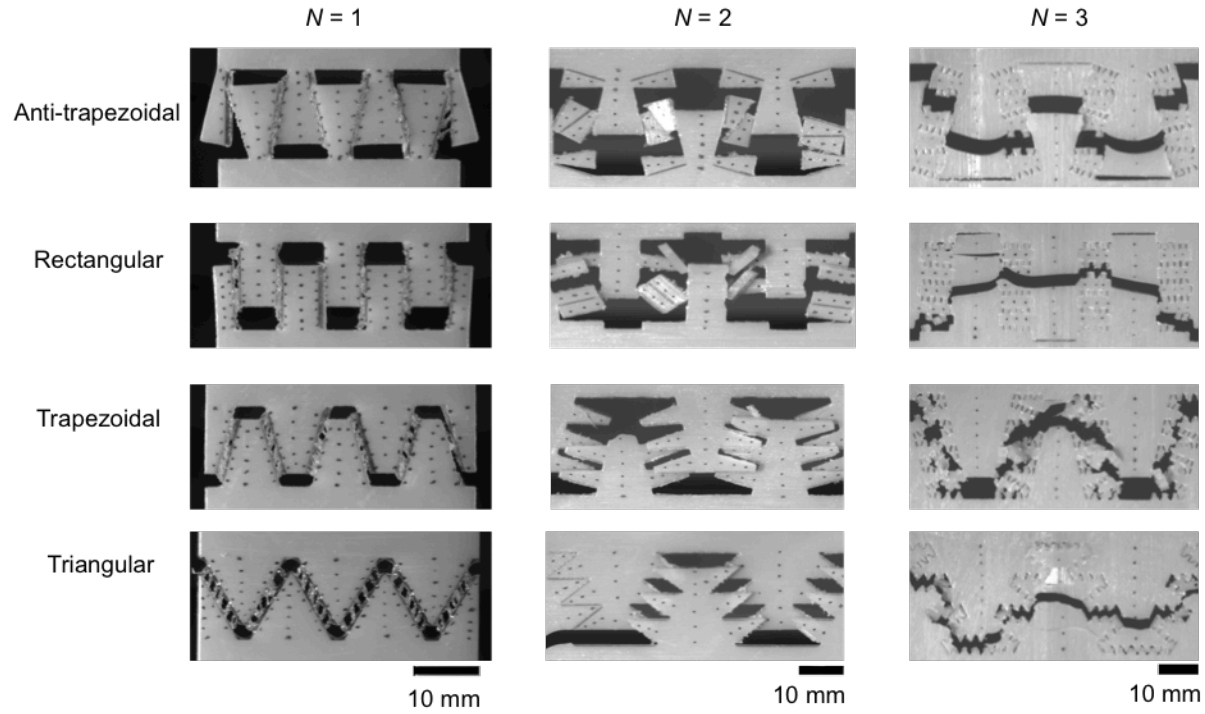

Figure 4-3 | Optical images of catastrophic failure of hierarchical suture interfaces under longitudinal tension.

The failure mechanisms of the third-order hierarchical suture interfaces were much more complex, as shown in Fig. 4-4(a), and determined the overall toughness of the suture interface. Catastrophic failure occurred when the cracks from major and minor teeth failure eventually coalesced to form a tortuous path across the suture interface. Therefore, the amount of interface failure and minor tooth failure prior to catastrophic failure greatly influenced the overall toughness of the interface. The major teeth of the anti-trapezoidal and rectangular geometries failed at lower strains of $\varepsilon = 0.04$ and 0.07, respectively, and therefore their load-bearing capacities fell quickly with each major tooth breakage. Triangular and trapezoidal geometries, on the other hand, exhibited significant interface and minor tooth failure prior to major tooth failure. In addition,

even with initial minor tooth failure, the triangular and trapezoidal geometries were still able to maintain interlocking of the major teeth, exhibiting significant damage tolerance.

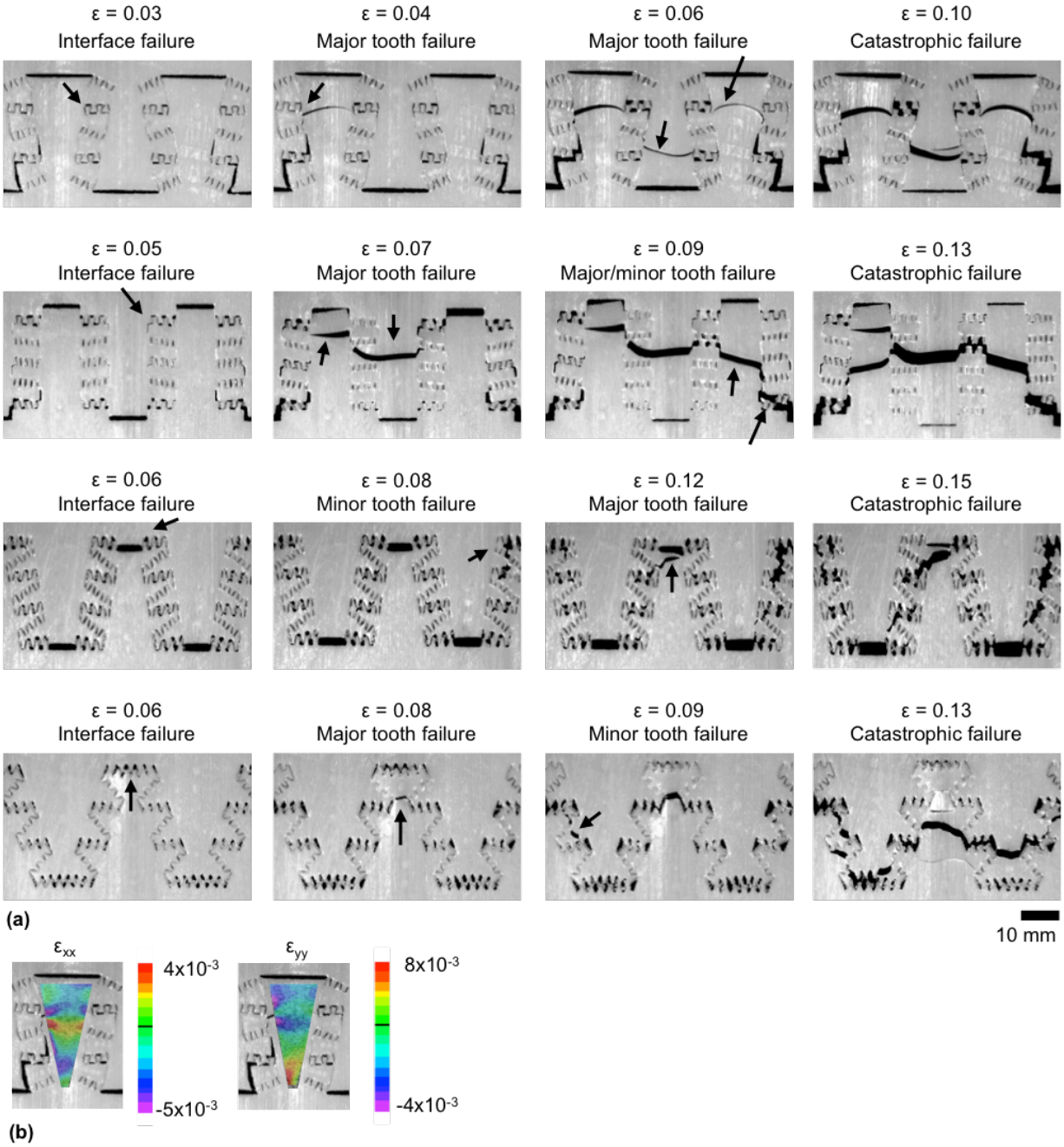

Figure 4-4 | Failure mechanisms of third-order hierarchical suture interfaces. (a) Optical images of third-order triangular and anti-trapezoidal suture interfaces, showing interface failure, minor and major tooth failure, and catastrophic failure, (b) strain contours of third-order anti-trapezoidal suture interfaces immediately prior to major tooth failure.

Tooth failure in first-order suture interfaces can occur for specific geometries, tip angles, and tooth to interfacial layer stiffness ratios, but always occurred at the base of the teeth. Third-order suture interfaces, on the other hand, exhibited major tooth failure near the middle or top of its teeth, even for anti-trapezoidal geometries, which had a small cross-sectional area at the base of its teeth. The location of major tooth failure can be explained by the strain contours shown in Fig. 4-4(b). The strain contours show the local strain in the anti-trapezoidal major tooth immediately prior to major tooth failure. Although the strain in the vertical direction is indeed greatest at the base of the tooth, there was a compressive strain from the interlocking of the teeth exactly where major tooth failure occurred. Failure along the middle of the major teeth allowed for interlocking even after tooth failure.

High resolution imaging of the third-order triangular suture interface specimen via scanning electron microscopy (SEM), post-failure, as shown in Fig. 4-5 revealed the deformation in the interfacial layer even in regions that remained intact. The failure of every interface in the triangular suture interface allowed for maximized energy dissipation. In addition, Figs. 4-5(d) and 4-5(f) shows slanted cracks through the interfacial layer that correspond to the periodic cavitations observed in the interfacial layer. As opposed to the interfacial layer, which eventually failed through the stretching and shearing modes, resulting in rough surfaces, the failure of the teeth was more brittle and resulted in smooth surfaces, as seen in Fig. 4-5(b). In addition, layers through the thickness of the material in both the interfacial layer and teeth can be seen in the images of the tilted specimens in Fig. 4-5(b) and 4-5(d), that resulted from the intrinsic layer-by-layer fabrication method of additive manufacturing.

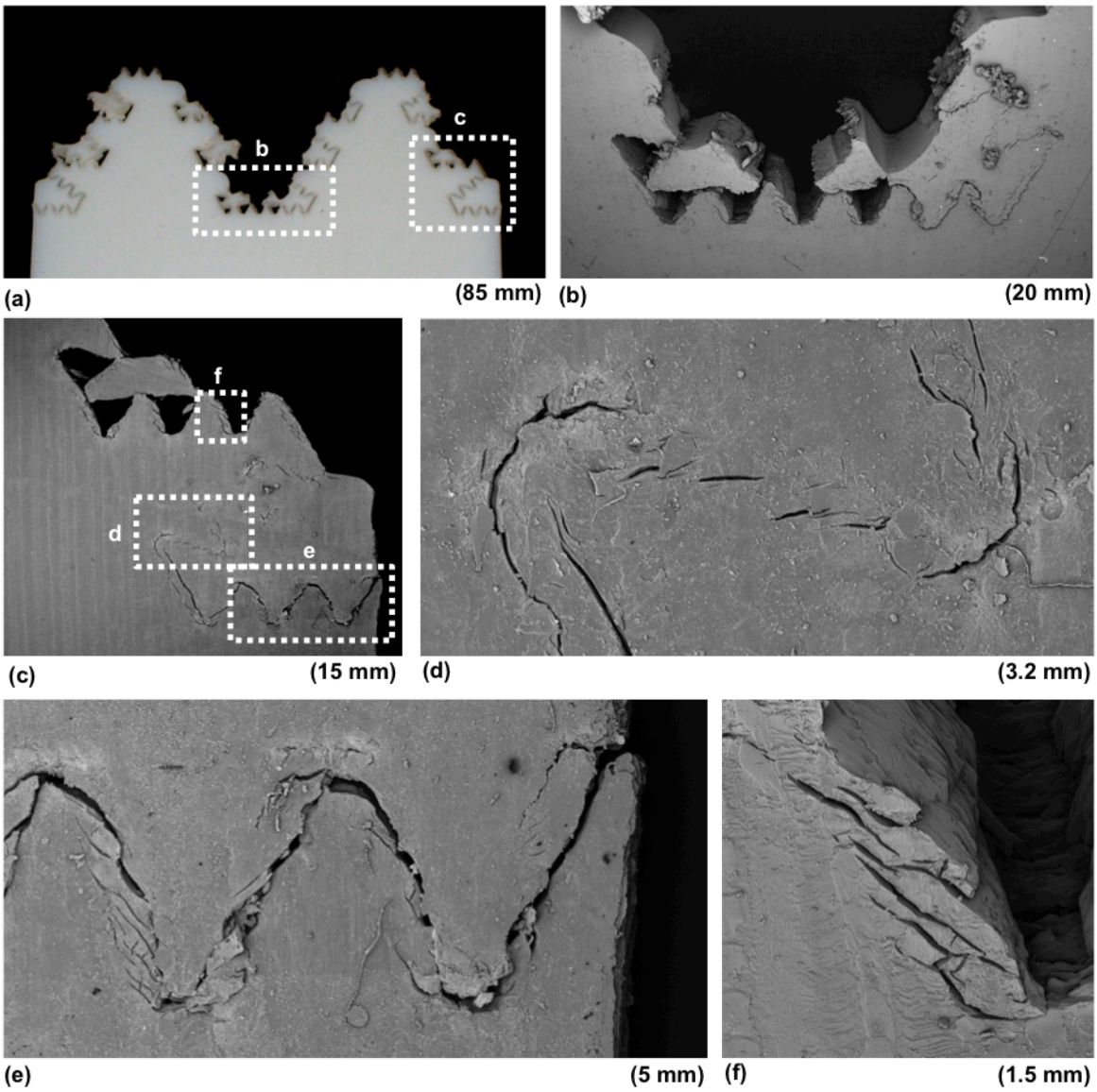

Figure 4-5 | Post-failure images, (a) optical, (b)-(f), scanning electron microscope images) of a triangular third-order hierarchical suture interface. Scales indicate the image width.

3.3.5 Comparison with Analytical Model

The analytical model presented in Li et al. (2012) predicted the stiffness, strength, and toughness of first, second, and third-order triangular suture interfaces. Fig. 4-6(a) shows a comparison between experimental results presented in this paper and the predicted mechanical properties. The model predicted the stiffness and strength of the triangular suture interfaces quite well with the exception of the strength of the second-order triangular suture interface. For this case, the experimental tensile strength is significantly less than predicted. This can be explained by the effect of boundary

conditions in the experiment, whether tooth failure occurs only at the edge, rather than across the entire suture interface.

As for toughness, it is difficult to capture this analytically due to the significant energy dissipation after maximum load-bearing capacity is exceeded. As shown in Fig. 4-6(b), triangular suture interfaces of all orders of hierarchy were able to dissipate energy significantly after reaching maximum load-bearing capacity. For all *N*, approximately 50% of the total toughness was due to the overall failure progression. Therefore, the difference in total toughness was doubled relative to the difference in toughness up to the peak stress when *N* was increased.

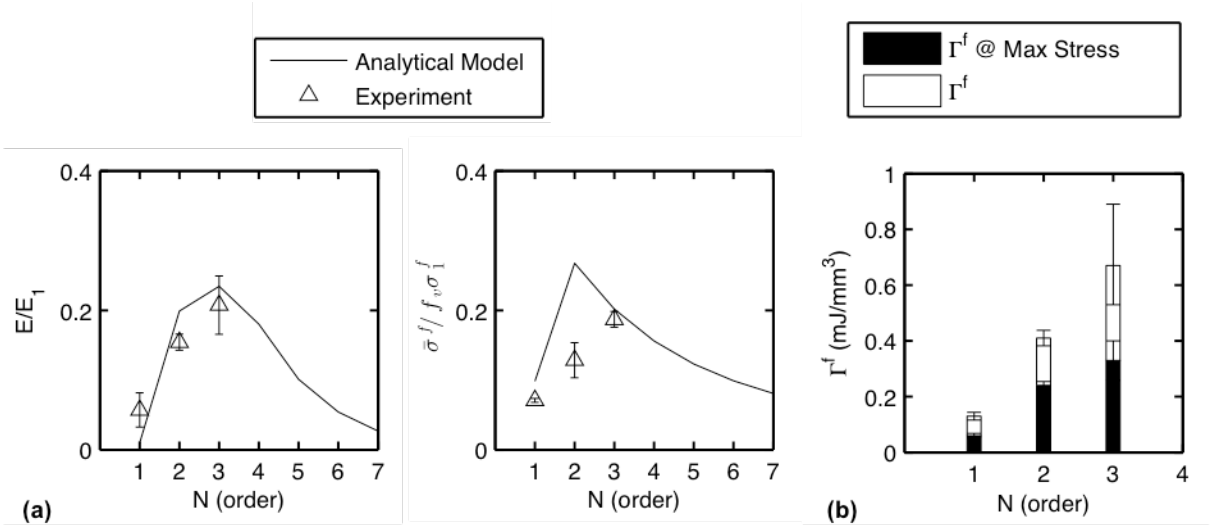

Figure 4-6 | Mechanical properties of triangular suture interfaces. (a) Experimental non-dimensional stiffness and strength compared to predictions from the analytical model, (b) Experimental toughness at maximum stress and total toughness. Error bars indicate the standard deviation.

4.4 Discussion and Conclusion

The stiffness, strength, toughness and failure mechanisms of suture interfaces can be tailored or amplified by changing the order of hierarchy. An understanding of the underlying role of geometry and hierarchy in the mechanical behavior of suture interfaces will allow for the design of damage tolerant materials with tailored mechanical properties. In particular, the increase in hierarchy shows an enhancement or tunability of mechanical properties that can be utilized to diversify the current additive manufacturing materials library.

4.4.1 Enhancement and Tunability of Interface Mechanical Properties

Four suture interface geometries with three orders of hierarchy, each resulted in different combinations of stiffness, strength, and toughness. For a given tooth volume fraction, increasing the order of hierarchy increases the complexity of the design. This complexity can be quantified by a suture complexity index, I_N, which is defined by the total suture interfacial layer length over the horizontal length of the suture interface structure[11]. With this definition, a simple flat interface would have $I_N = 1$.

Fig. 4-7(a) shows the stiffness, strength, and toughness ratios of geometric suture interfaces relative to a flat interface with respect to I_N. By increasing the suture complexity index by less than six times, the stiffness can be increased by 50 times, and strength and toughness increased by 5 times. Even doubling the suture complexity index can result in an order of magnitude increase in stiffness and double the strength for triangular suture interfaces. In addition, the increases in mechanical properties have a clear dependence on geometry, with the triangular and trapezoidal geometries resulting in the greatest increases generally, and the anti-trapezoidal geometry resulting in the least significant increase. With additive manufacturing, because added complexity and changes in geometry is easily accomplished, often with no net effect on total fabrication time, significant improvements in mechanical behavior of interfaces can be conveniently attained. Fine-tuning of mechanical properties can thus be easily accomplished through changes in suture interface geometry and complexity.

In addition, Fig. 4-7(b) shows that stiffness, strength, and toughness can all be improved without the usual tradeoff between the properties. For all three properties, triangular suture interfaces exhibit highest stiffness, strength, and toughness. Apart from the triangular geometry, the general trend shows increased stiffness with increased strength and increased toughness for many designs. Therefore, the use of suture interface design in conjunction with additive manufacturing is a simple way of enhancing mechanical properties of interfaces.

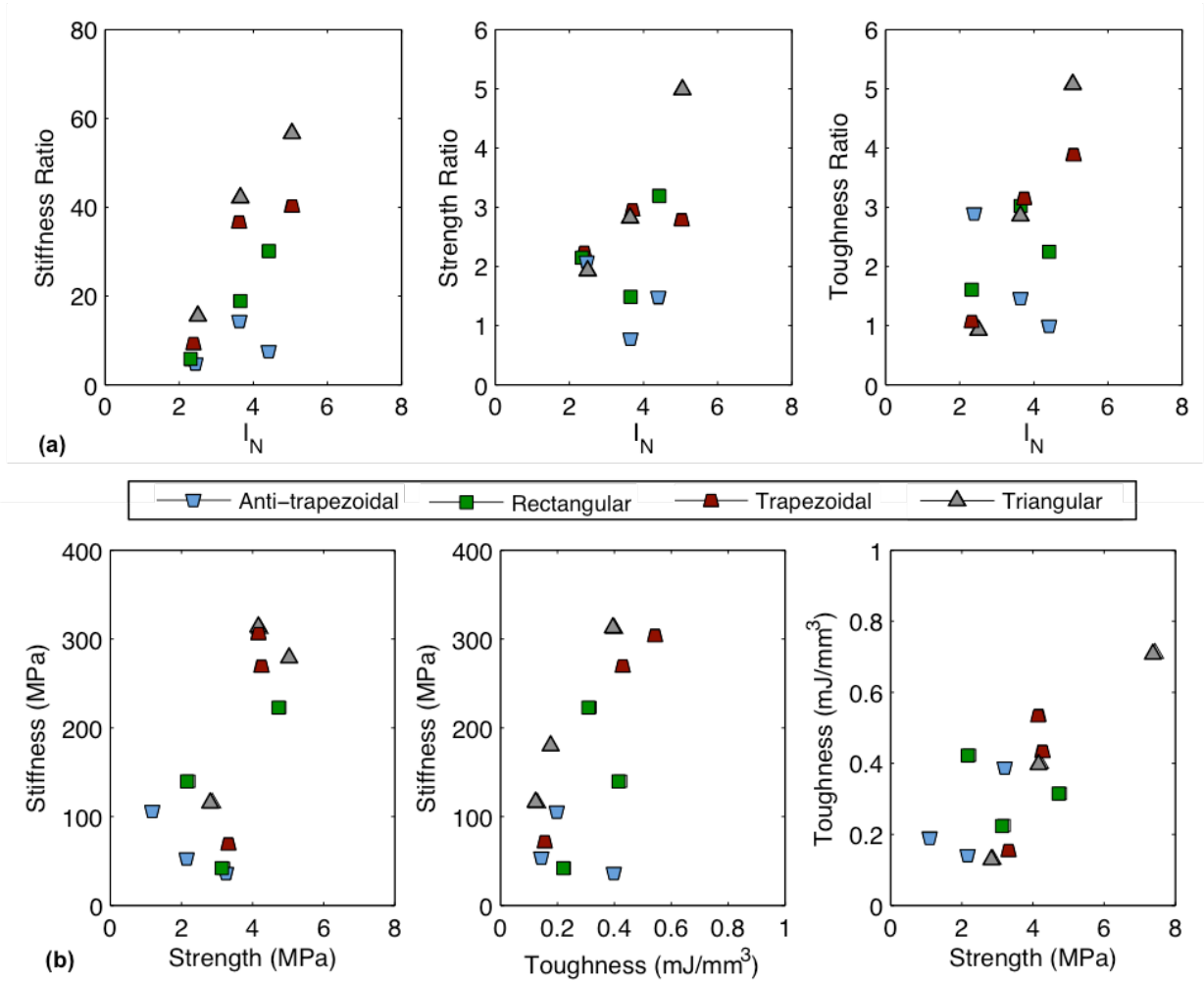

Figure 4-7 | Tunability and enhancement of mechanical properties of suture interfaces. (a) Experimental stiffness, strength and toughness ratios of suture interfaces with respect to their suture complexity index, I_N, (b) Stiffness vs. strength, stiffness vs. toughness, and toughness vs. strength of hierarchical suture interfaces. Standard deviation of experimental values is given in Table 1.

4.4.2 Expanding the Additive Manufacturing Materials Library

Currently, a number of metallic, ceramic, and polymer materials can be utilized in additive manufacturing, but as in nature, the available materials and the mechanical behavior of the materials are limited compared to other manufacturing methods. Just as nature utilizes geometry to create materials with an incredible range of mechanical properties[29,40,47], suture interfaces can also be utilized to expand the current range of mechanical properties available for additive manufacturing. As demonstrated by the results in this paper, bio-inspired hierarchical suture interface designs can enhance or tune mechanical properties of interfaces. Therefore, these same design principles can be

utilized to combine currently available materials to create materials with different mechanical properties that can be easily fabricated via additive manufacturing.

4.4.3 Hierarchical Suture Interface Designs with Natural Materials

In this chapter, the influence of hierarchical suture designs with additively manufactured polymers was shown to amplify the toughness relative to flat interface designs. It is interesting to note that due to the inherently different mechanical properties of natural materials, the effects of hierarchical suture interface designs are expected to be even more largely amplified. As opposed to the ductile additively manufactured polymers used in the present study, many natural materials, such as the mineral phase of ammonite shells, aragonite, is brittle. With a brittle suture tooth material, hierarchical suture interface designs essentially provide the structure with increased ductility. In contrast, the hierarchical suture designs with organic interfacial layers reported in this present study are able to exhibit graceful failure, and as demonstrated, can greatly amplify the toughness of the synthetic structures relative to their natural biological counterparts.

5 Suture composites

5.1 Introduction

Composite materials are materials that consist of two or more materials with significantly different properties that produce a material with properties different from any of the constituent materials. Composite materials are designed to take advantage of the best properties of individual constituents, but also have also been shown to result in better mechanical properties depending on how materials are combined. Due to the range of properties achievable through composite materials, they have been used in many industries including aerospace, energy, and civil construction.

Nature is filled with examples of composites that have amplified mechanical properties relative to their weak constituents. Sponge spicules have incredible flexural toughness; nacreous shells and crab exoskeleton have increased tensile strength and toughness[48]; armor plates of stickleback fish allow for protection and flexibility[10]. In all these examples, the structure of the composite material is essential to the amplification of mechanical properties.

The suture interfaces described in the previous chapters can be extended to composite materials by extending the interface in both directions (Figure 5-1). These suture composites have a natural flexibility that is dependent on the suture geometry. Therefore, through changes in geometry, both mechanical properties under tension and bending can be tailored simultaneously.

This chapter investigates the mechanical behavior of suture composites under tension and bending through analytical models, finite element simulations, and experimental testing. Through careful analysis, the mechanics and failure mechanisms of suture composites are elucidated, and design principles are extracted that can guide efficient design of suture composites that meet given requirements.

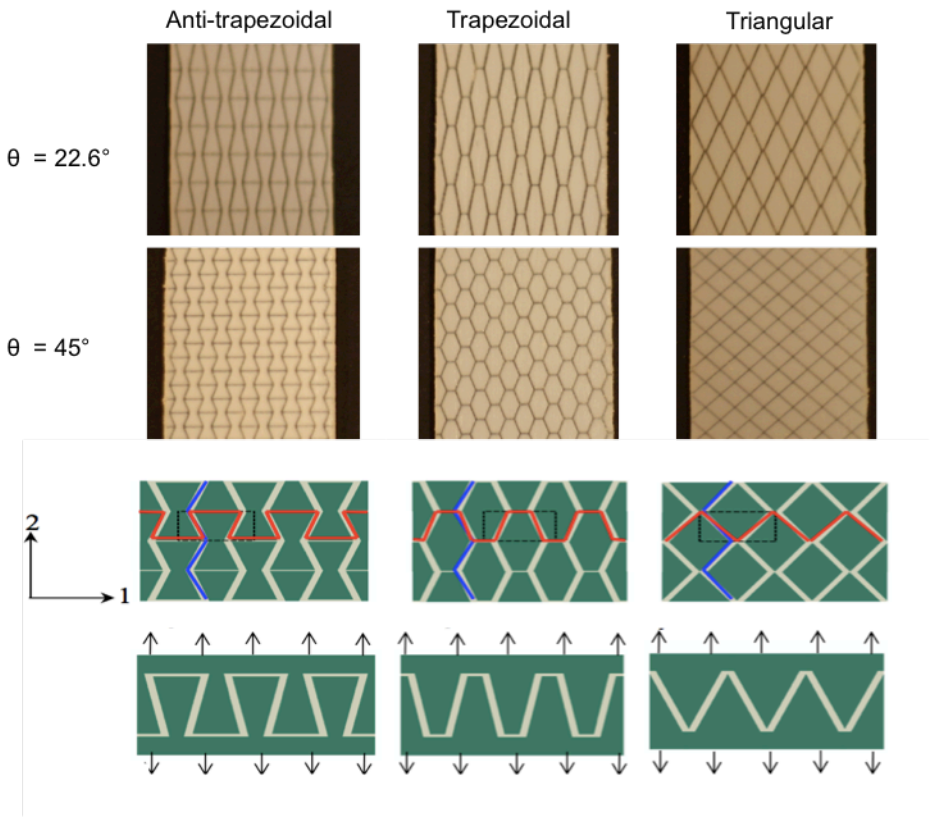

Figure 5-1 | Extension of suture interfaces to suture composites.

5.2 Materials and methods

5.2.1 Three-point bending

Three-point bending tests are performed on the Zwick mechanical tester (Zwick Z010, Zwick Roell, Germany). Suture composite prototypes are 3D-printed with the same materials as previous chapters.

5.2.2 Finite element modeling

Finite element modeling is performed using ABAQUS. Tensile tests are simulated in 2D with a single RVE and periodic boundary conditions. Three-point bending tests are simulated in 3D with tetrahedral elements.

5.3 Results

5.3.1 Tensile tests of suture composites

As shown in Figure 5-1, under longitudinal tension, the geometry of each row of the suture composite is identical to the suture interface. Therefore, the same analytical models discussed in Chapter 2 and 3 can be utilized to predict the stiffness and strength of suture composites under longitudinal tension. These analytical predictions were compared to finite element analysis results (for stiffness) and experimental results (Figure 5-2). For a smaller tip angle of 22.6°, analytical, finite element, and experimental results agree quite well, showing the trends discussed in Chapter 3. At a larger angle of 45°, the analytical, finite element, and experimental results mostly agree, with a few interesting discrepancies. In particular, the experimental stiffness and strength of the triangular geometry is significantly higher than that predicted, and the strength of trapezoidal and anti-trapezoidal geometries without the flat interface material is lower than predicted. The reasons for these discrepancies are explored in the following sections by looking at experimental failure processes and finite element results.

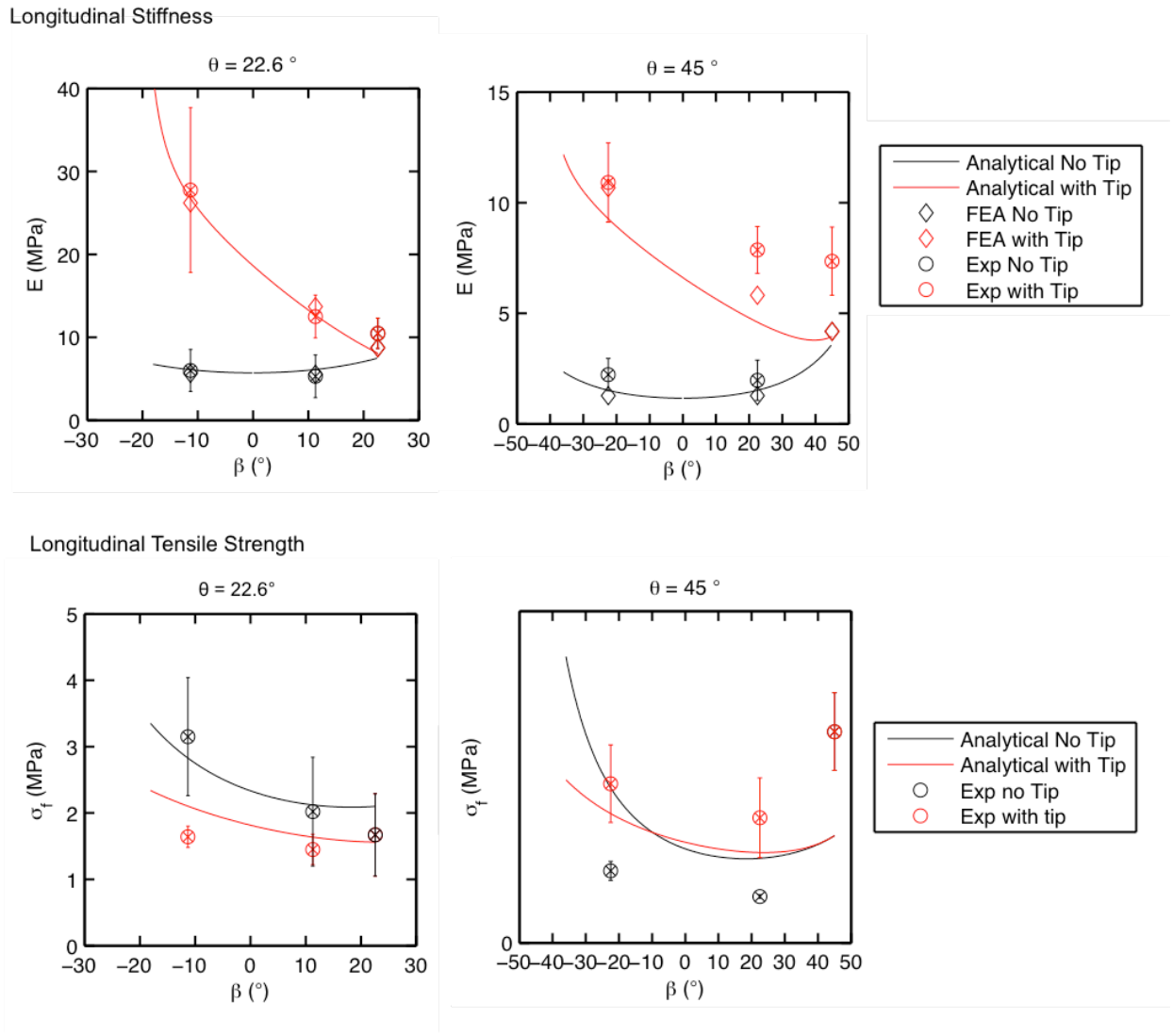

Figure 5-2 | Stiffness and strength of suture composites under longitudinal tension.

Under longitudinal tension, the suture composites all failed by interface failure (Figs. 5-2 and 5-3). Figure 5-2 shows the failure process of regular suture composites, with a tip angle of 45°, and Figure 5-3 shows the failure process of suture composites with a tip angle of 22.6°. Similar to the suture interfaces discussed in the previous chapters, all suture composites show failure of the flat interfaces initially. However, for the composite structure, not all slant interfaces fail. Suture composites with a smaller tip angle ($\theta = 22.6°$) fail at a lower strain than those with a larger tip angle ($\theta = 45°$), which corresponds to the higher stiffness of suture composites with smaller tip angles. At both tip angles, the interlocking of anti-trapezoidal geometry is apparent, requiring the stiffer teeth to strain in the x-direction to allow the teeth to slide past each other.

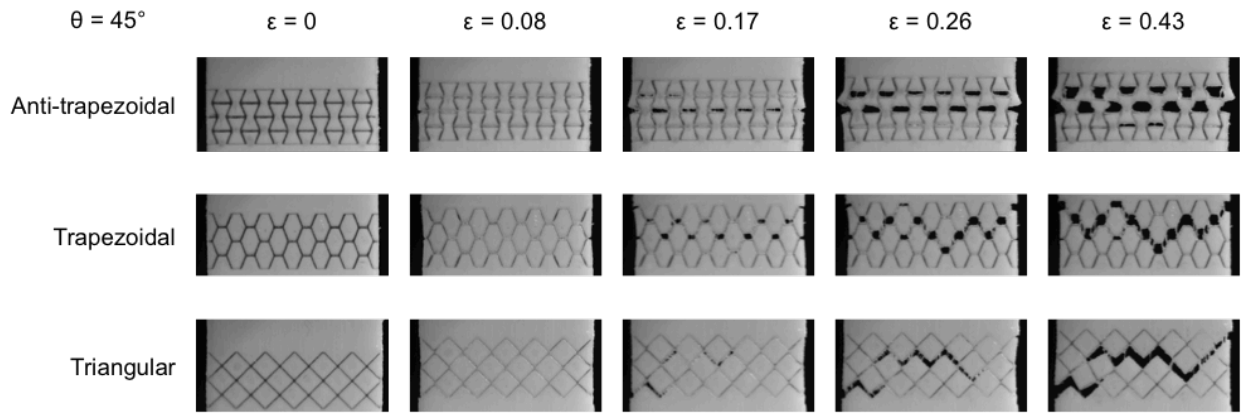

Figure 5-3 | Failure of suture composites under longitudinal tension.

Looking at the failure process of regular suture interfaces, the geometry largely affects the tortuosity of the failure path. For the anti-trapezoidal geometry, after failure of flat interfaces, only slant interfaces along the center row of teeth fail. In the trapezoidal geometry, the slant interfaces along two rows of teeth fail. For the triangular geometry, most of the slant interfaces fail, resulting in a failure path that spans all three rows. Similar to the third-order hierarchical triangular suture interfaces discussed in Chapter 4, the failure of most slant interfaces allows for the maximal amount of energy dissipation. Because the failure spans more than a single row, the failure of the triangular suture composite under longitudinal tension is not identical to that of a triangular suture interface. This difference could explain the discrepancy between the analytical model and the experimental results discussed earlier.

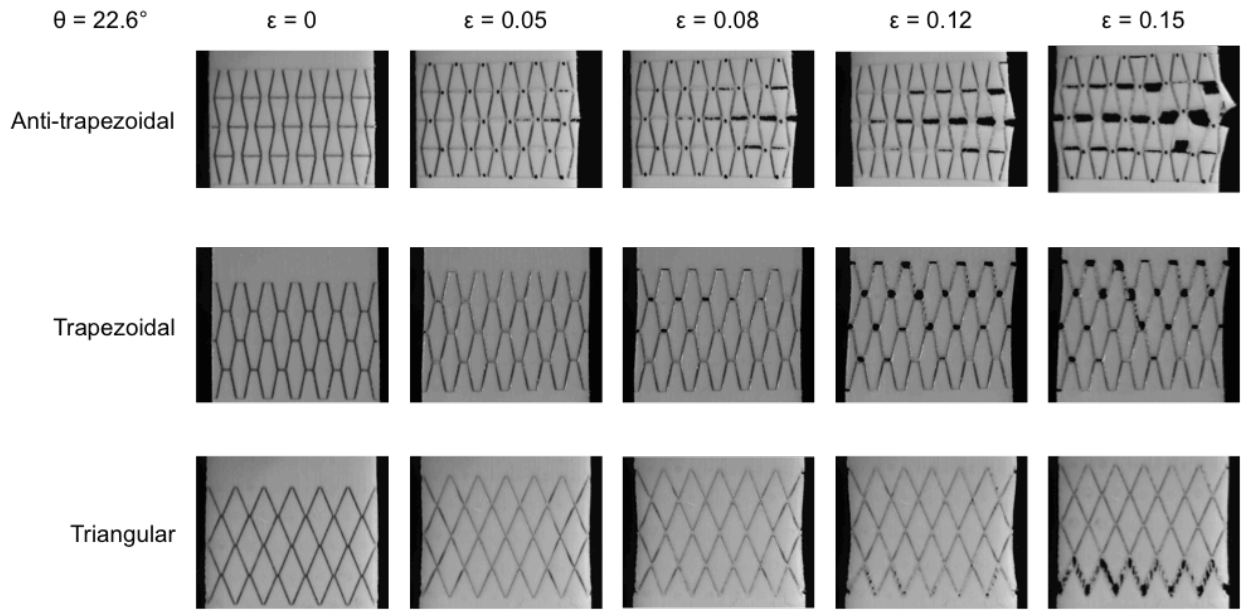

Figure 5-4 | Failure of suture composites under longitudinal tension

For suture composites with a smaller tip angle, failure occurs mostly along one row of slant suture interfaces. For the triangular suture composite, the entire sample contracts along the x-direction as strain increases from $\varepsilon = 0$ to $\varepsilon = 0.12$, similar to the triangular suture interface with a small tip angle in Chapter 2. At $\varepsilon = 0.12$, cracks begin to form along the slant interface of the bottom row, and failure propagates along that row. Looking only at the bottom row of the triangular suture composite at $\varepsilon = 0.15$, the failure process looks identical to that of triangular suture interfaces.

A better understanding of the effect of geometry on the behavior of suture composites can be gained by looking at stress and strain contours from finite element analysis. Figure 5-5 shows normal stress (σ_{22}), shear stress (σ_{12}), and shear strain (ε_{12}) of the suture composites. Looking at the normal stress in the teeth of the anti-trapezoidal suture composite, there is a variation in normal stresses across the tooth. There is a high stress concentration at the corner of the small base of the teeth, and decreasing normal stress towards the wider tip of the teeth. For the area surrounding the flat interface, there is even a very slight compressive normal stress due to the interlocking of the teeth. In addition, the tooth area surrounding the slant interface does not experience significant shear stress, while the center of the tooth and the area near the flat tip interface experiences some shear stress. For the trapezoidal suture composite, normal stresses exhibit similar behavior, with the largest stress being near the corner of the base of the teeth. The smaller tip of the tip also experiences slightly less normal stress, although it is not compressive like the anti-trapezoidal geometry. The shear stress is more concentrated at the base of the teeth than the anti-trapezoidal geometry. Similar to the

anti-trapezoidal geometry, there is an area near the interface that experiences less shear stress, although it is slightly less than the anti-trapezoidal geometry. Finally, for the triangular geometry, there is uniform normal stress in the teeth. As opposed to the trapezoidal and anti-trapezoidal geometry, there is actually higher shear stress surrounding the interface. For all geometries, the shear strain is localized in the interface and insignificant in the teeth.

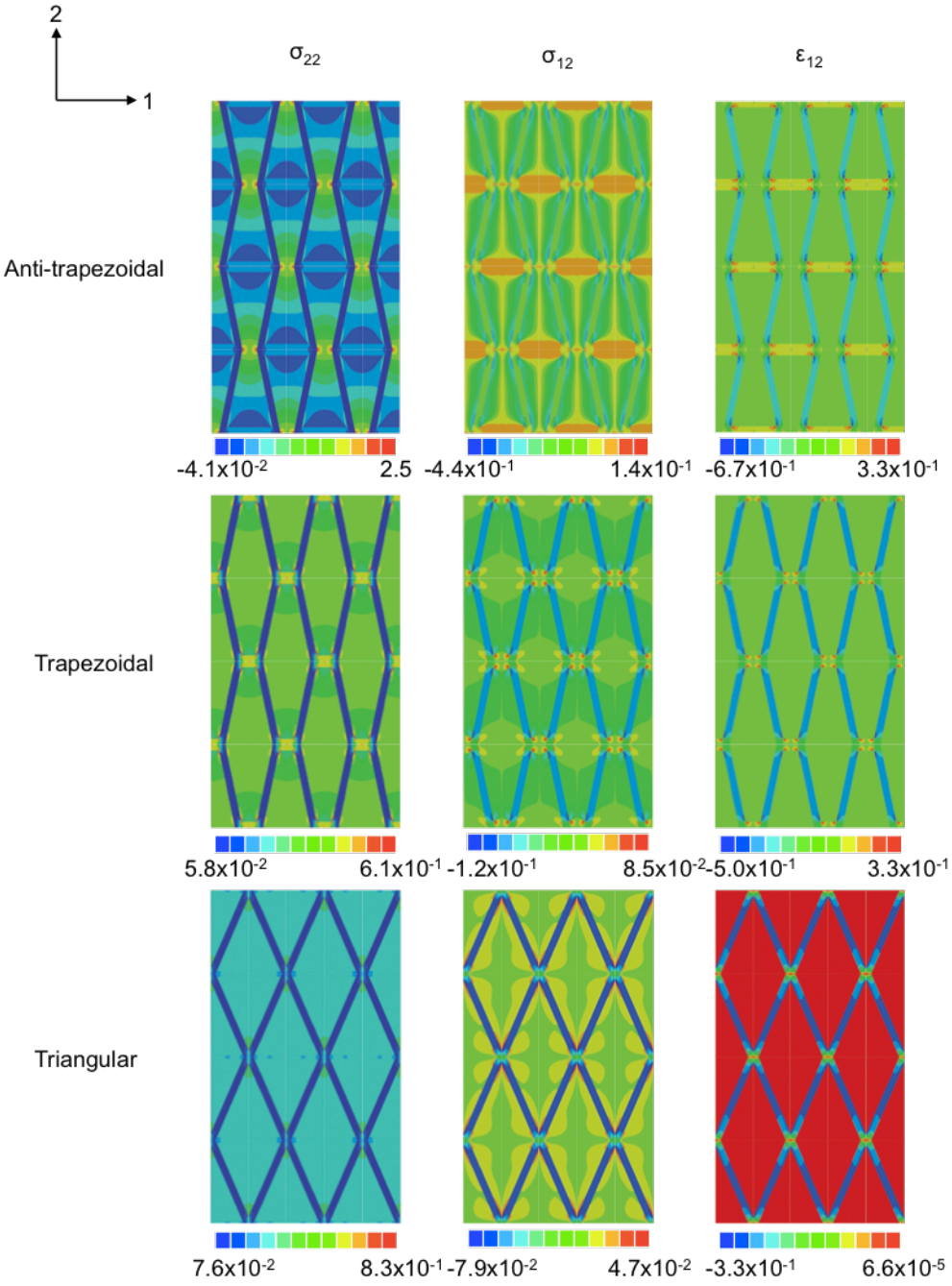

Figure 5-5 | Stress and strain contours from FEA of suture composites under longitudinal tension (strain = 0.3)

The normal and shear stresses are transformed from the 1-2 frame to a frame aligned with the slant interface in order to better understand the stresses and strains along the slant interfaces (Figure 5-6). From these stress contours, it can be seen that there is normal stress (normal to the interface) in the triangular interfaces, but it is insignificant in the anti-trapezoidal geometry. Shear stress and strain is most prominent in the interfaces of the anti-trapezoidal geometry.

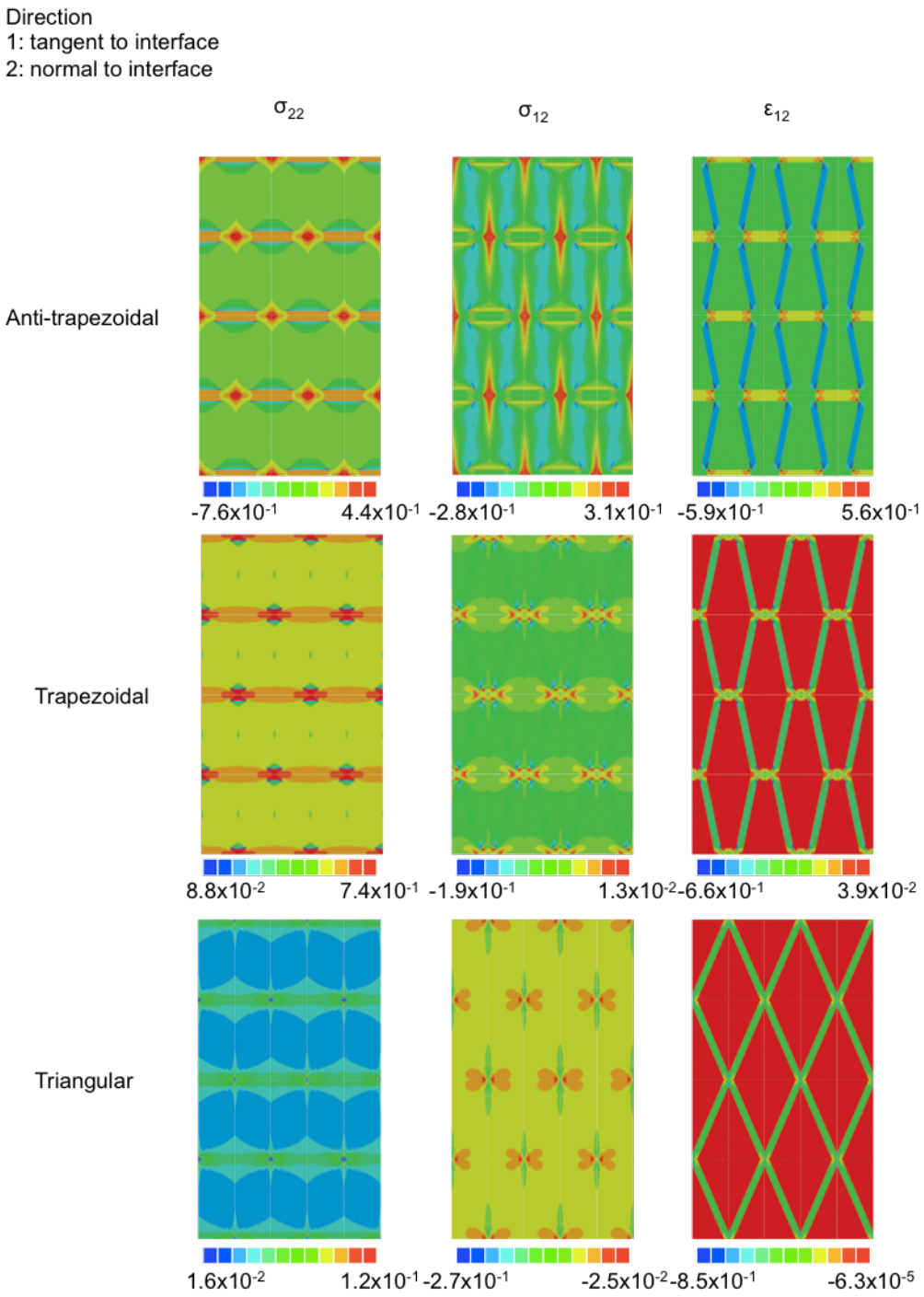

Figure 5-6 | Stress and strain contours from FEA of suture composites under longitudinal tension.

Suture composites without flat tip interface material shows similar stress and strain contours (Figs. 5-7 and 5-8). All of them possess a lower magnitude of stress which corresponds to the lower stiffness. For the trapezoidal geometry, there is larger area of higher stress surrounding the tips of the teeth, in addition to distinctly seeing the shear

stress increase in areas farther away from the slant interfaces. In addition, the shear stress in the interfaces are much more prominent without the tip interface.

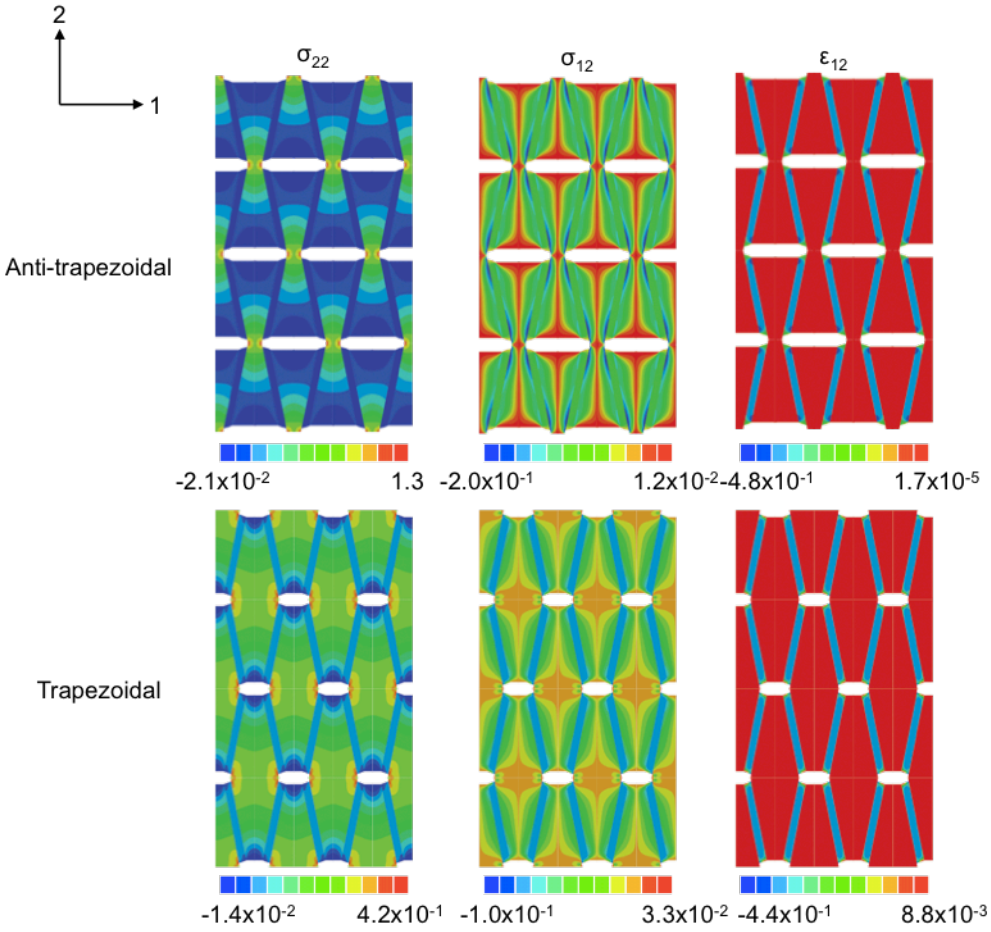

Figure 5-7 | Stress and strain contours from FEA of suture composites without tip material under longitudinal tension.

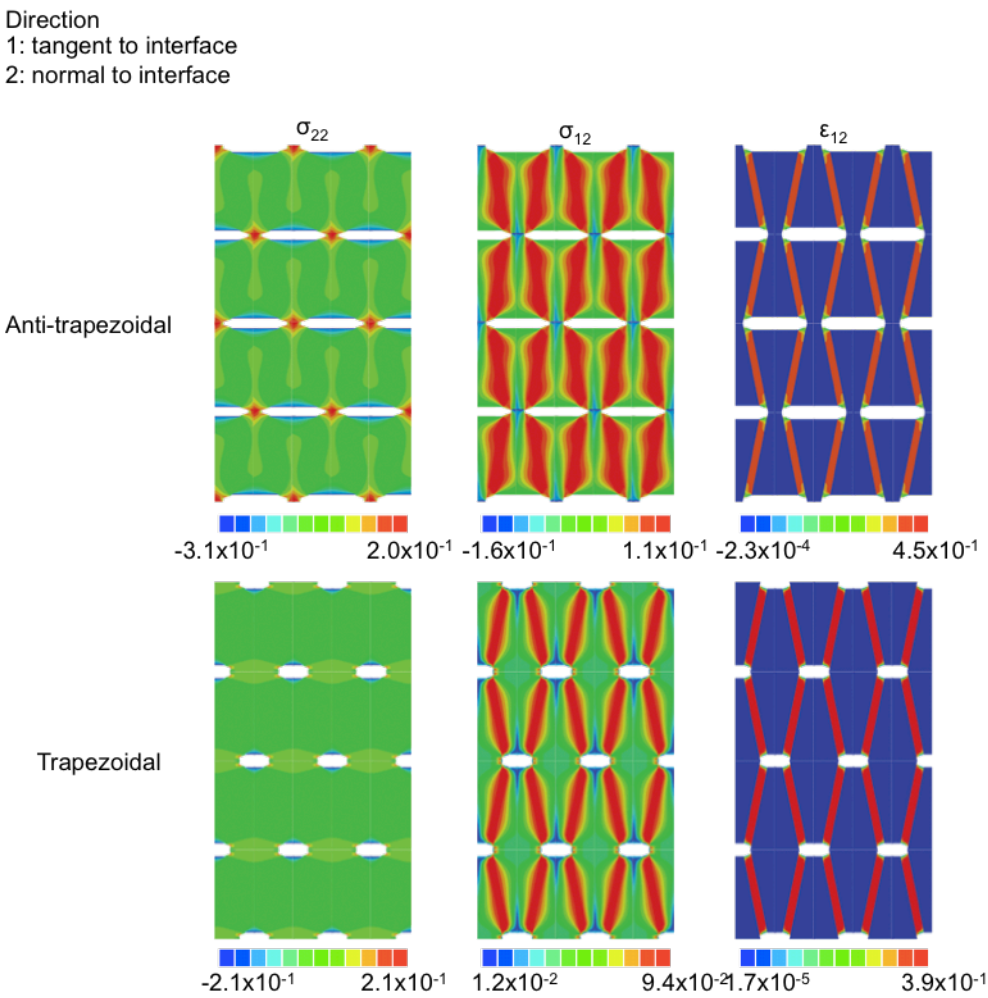

Figure 5-8 | Stress and strain contours from FEA of suture composites without tip material under longitudinal tension

5.3.2 Three-point bending of suture composites

Both experimental and finite element analysis results show that the anti-trapezoidal suture composite has the highest stiffness, while the trapezoidal and triangular suture composite have similar stiffnesses at a tooth angle of $\theta = 45°$. On the other hand, FEA results show that the for a tooth angle of $\theta = 22.6°$, the trapezoidal has a bending stiffness in between that of the anti-trapezoidal suture composite and the triangular suture composite (Figure 5-9a,b). Since bending stiffness varies linearly with Young's modulus, these trends fit previously discussed results, where the Young's modulus of the anti-trapezoidal suture composite (with tip material) is significantly greater than that of the trapezoidal and triangular suture composite. In addition, at a larger tip angle of $\theta = 45°$, the Young's modulus of the trapezoidal and triangular suture composites

are quite similar. At the same force, results from FEA show the triangular suture composite having the greatest displacement in the 3-direction (Figure 5-9d).

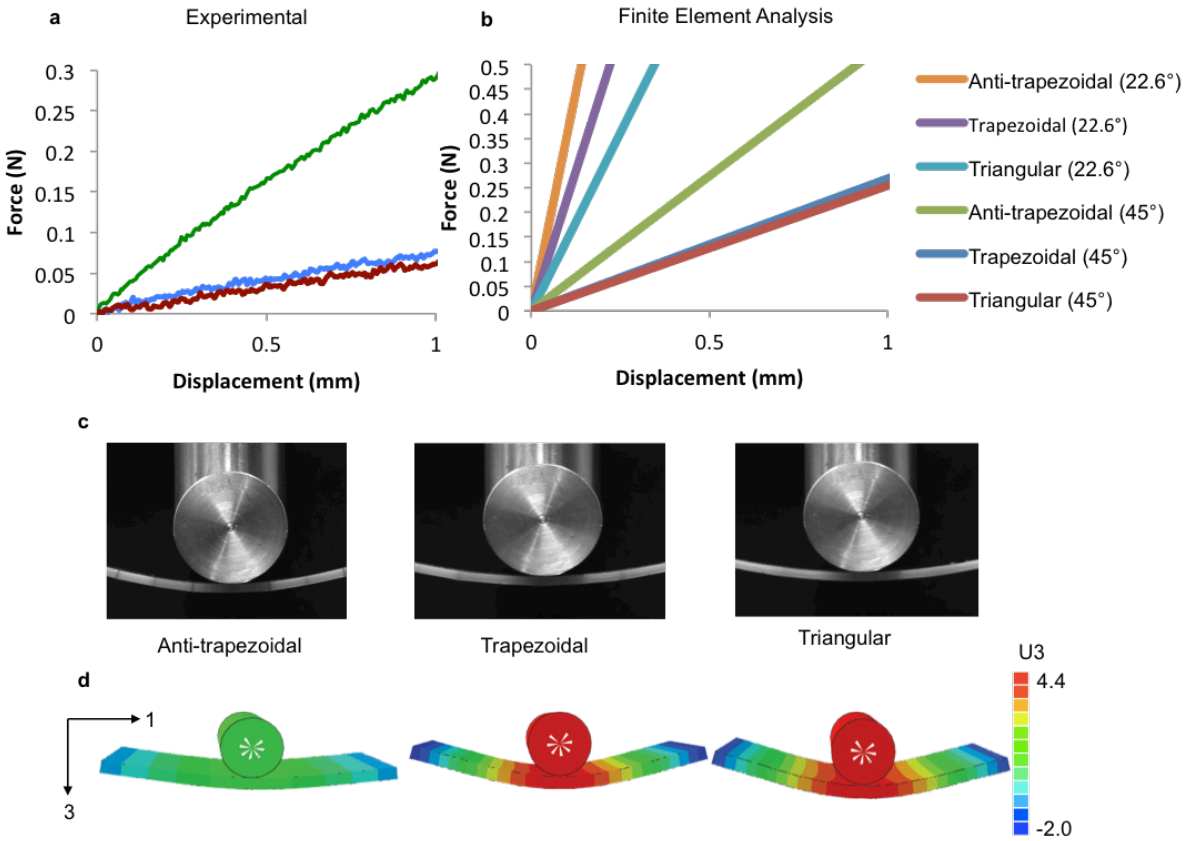

Figure 5-9 | Three-point bending of suture composites. a Experimental force-displacement of anti-trapezoidal, trapezoidal, and triangular suture composites with a tip angle of $\theta = 45°$, b FEA force-displacement of the same suture composites with a tip angle of $\theta = 45°$ and $\theta = 22.6°$, c optical images of three-point bending from experiment, and d displacement in the 3-direction from FEA three-point bending.

Figure 5-10 shows the stress and strain contours of the anti-trapezoidal, trapezoidal, and triangular suture composites at the same displacement of U3 = 0.3. From strain contours showing the tension in the top surface (σ_{11}), the anti-trapezoidal suture composite shows high stress concentration at the smaller base of the teeth. In the trapezoidal and triangular geometries, the stress is distributed across the entire teeth. At small tablet sizes relative to the radius of the die, however, the teeth undergo essentially no strain and can be seen as rigid. As for ε_{11}, the strain is concentrated in the flat tip interfaces and has highest magnitude in the anti-trapezoidal geometry. The slant interfaces of the anti-trapezoidal geometry undergo slight compression in the 1-direction. The triangular suture composite does not have a flat interface, and therefore the largest ε_{11} is present in the slant interfaces. This strain, however, is less than that of the flat interfaces of the trapezoidal and anti-trapezoidal suture composites. As for the

shear strains (ε_{13} and ε_{23}), the anti-trapezoidal suture composite has the smallest ε_{13} shear strain in the flat tips, as well as the smallest ε_{23} shear strain in the slant interfaces, while the triangular suture interface shows the largest shear strains in both cases. Therefore, the largest component of strain in the anti-trapezoidal suture composite is the normal tensile strain of the flat tip interfaces, while the largest component of strain in the triangular suture composite is in the shearing of the interfaces in the 1-3 and 2-3 directions. The difference in the strain distributions sheds light on the difference in bending stiffness since for the shear modulus is significantly less than the Young's modulus.

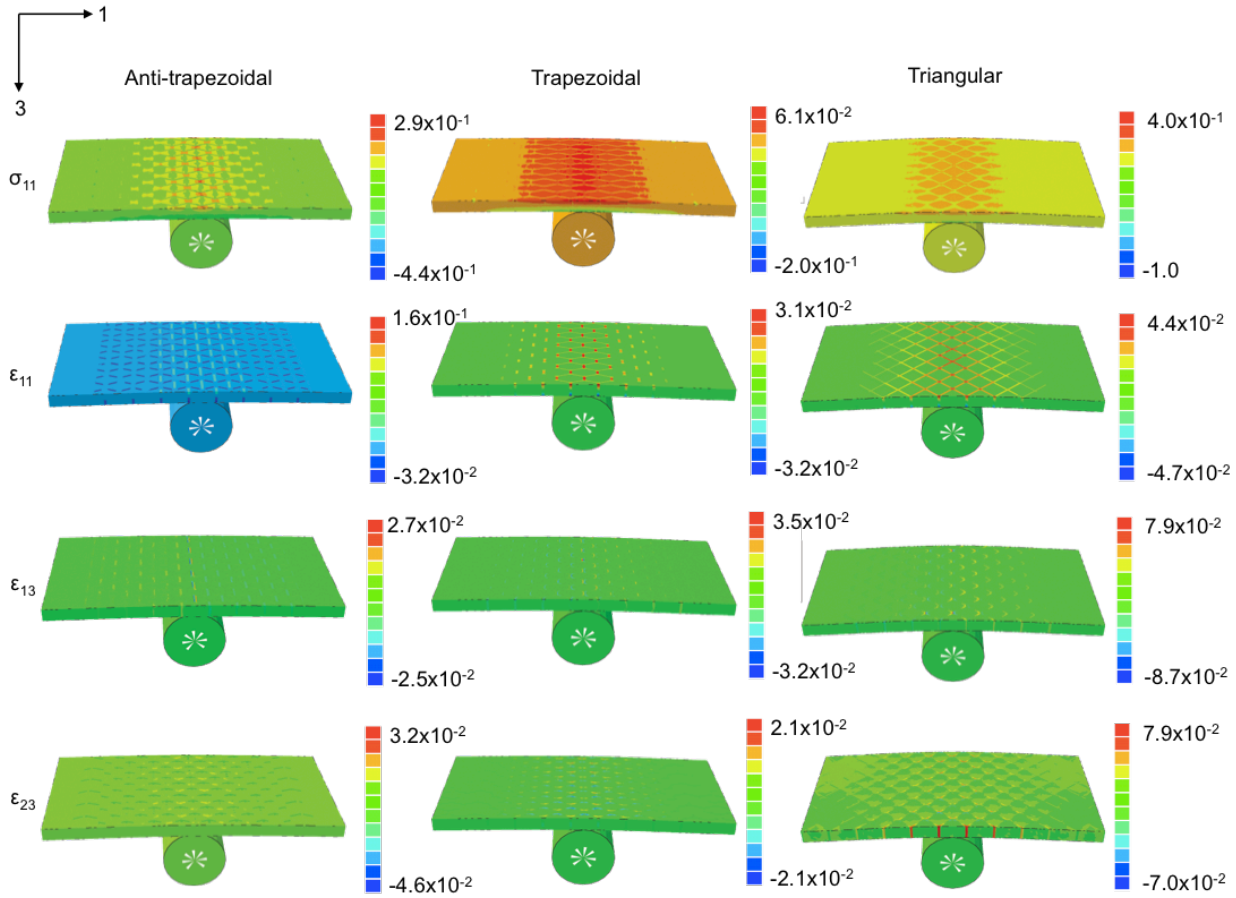

Figure 5-10 | FEA stress and strain contours of suture composites (θ = 45°) under three-point bending at a vertical displacement of U3 = 0.3.

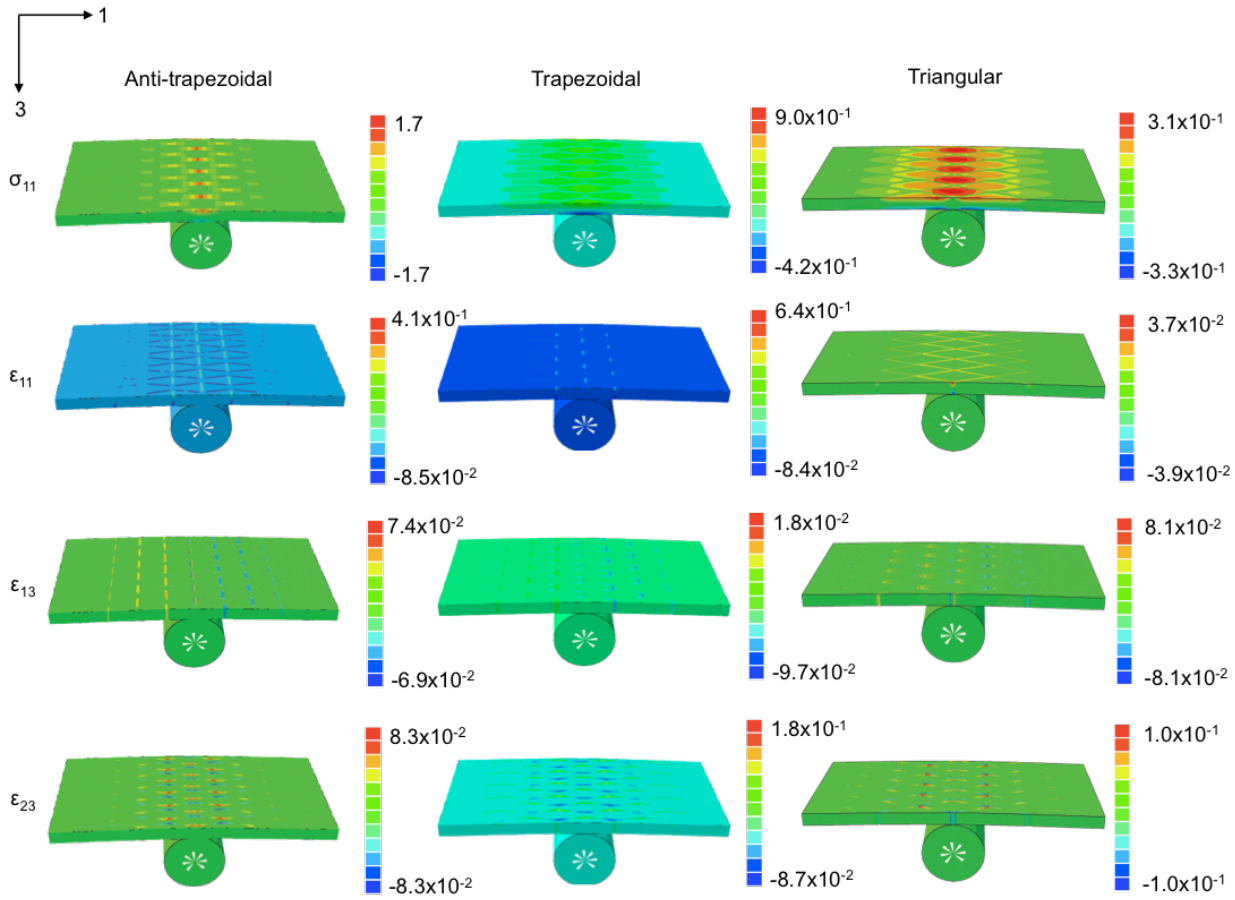

Figure 5-11 | FEA stress and strain contours of suture composites (θ = 22.6°) under three-point bending at a vertical displacement of U3 = 0.3.

As for suture composites with a smaller tip angle, the tablet size is also larger than the radius of the die. In such cases, there will be significantly more stress in the teeth, as shown in Figure 5-11. Because the teeth are much stiffer than the interface, there is also significantly greater deformation in the interfaces to reach the same vertical displacement. For a smaller tip angle, the difference between the trapezoidal and triangular suture composite becomes more pronounced.

5.4 Discussion

5.4.1 Tailoring flexibility through variation in size

From the tensile and bending test results shown above, it is shown that the tensile stiffness and strength of the suture composite is dependent on the tip angle and the geometry, while the bending stiffness is dependent on the tablet size and the geometry. This means that suture composites that maintain the same tip angle but have a variance in tablet sizes (Figure 5-12), can maintain the same tensile stiffness while varying in the

bending stiffness. This can lead to designs with tailored flexibility that does not sacrifice in stiffness and strength.

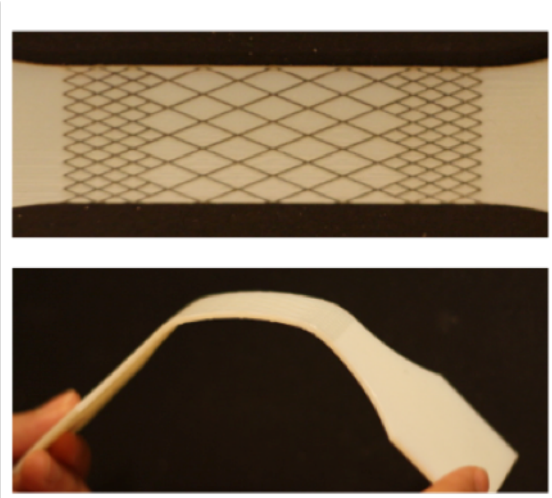

Figure 5-12 | 3D printed prototypes of suture composites with varying bending stiffness.

5.4.1 Tailoring flexibility through variation flat tip interface material

In both tension and bending, the flat tip interface of the anti-trapezoidal and trapezoidal geometries are shown to significantly influence the stiffness and strength. While the amplified tensile stiffness and strength from a flat tip can often be useful, the decrease in flexibility may not be optimal for designs. One way to capture some of the increase in tensile strength and stiffness while allowing for more flexibility in bending would be to utilize a material in the flat tip interface that is less stiff than the slant interface. Through changing material properties in only the flat tip interface, the bending stiffness can be tailored to fit the function of the material.

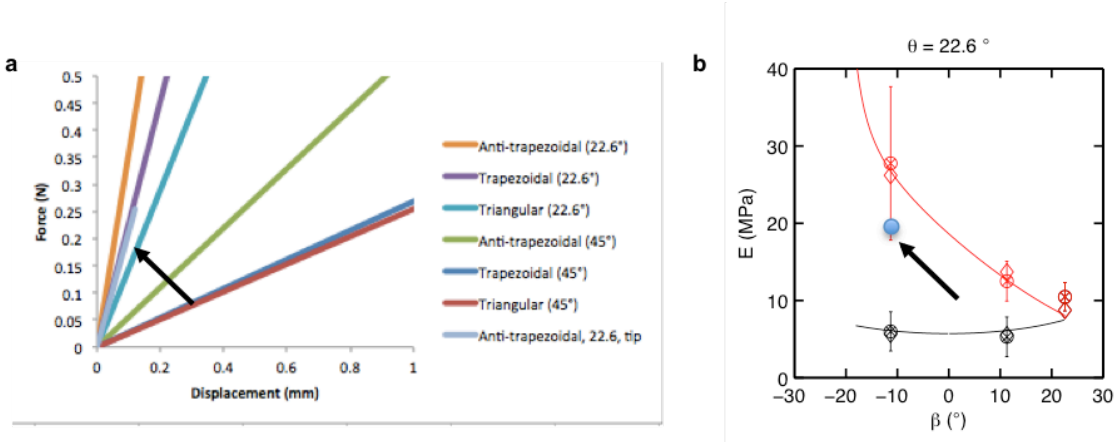

Figure 5-13 | Tailoring flexibility and stiffness of suture composites. a Force-place displacement behavior of anti-trapezoidal suture composite with changed tip material has the same behavior as a trapezoidal suture composite, b Stiffness of anti-trapezoidal composite with changed tip material has higher stiffness than the trapezoidal suture composite.

As a proof of concept, the force-displacement behavior and stiffness of anti-trapezoidal suture composites with different flat tip material were simulated. The flat tip material has a stiffness that is only half of the stiffness of the slant tip material. From Figure 5-13, the resulting bending behavior is similar to that of a trapezoidal suture composite, however, the stiffness is higher than that of a trapezoidal suture composite. From this simulation, it shows how simple changes in material can result in simultaneous tailoring of stiffness and flexibility. In addition, by understanding the mechanics of the composites under tension and bending, optimal and efficient designs can be created with specific mechanical properties.

6 Multi-scale design of suture interfaces

6.1 Introduction

In nature, design across multiple length scales amplifies mechanical properties of the biological material. Through macro-scale design and 3D printing of suture composites, we have demonstrated and explored the tunability and amplification of stiffness, strength, and toughness through macroscopic geometric changes. This chapter will further explore the tunability and amplification of mechanical properties though both micro-scale and macro-scale designs. Specifically, we are interested in maximizing the toughness of the suture composites through hierarchical designs.

In composite literature, the mechanical properties of composites with structure at the nanoscale (nanocomposites), microscale (fiber composites), or macroscale have been studied. However, there has been little design and fabrication of composites that span multiple length scales. Here, additive manufacturing can be a huge advantage, allowing for precise and convenient design at both the micro and macro scale. In addition, nanocomposites in nature mostly consist of less than 10 weight percent of nanoparticles (e.g. carbon nanotubes or nanoclay). With additive manufacturing, the weight percent can be much higher, closer to what is observed in nature.

Over the years, there has been incorporation of nanoparticles in various additive manufacturing techniques. Metal nanoparticles, including iron and silver[49], were incorporated into printed inks and reached high concentrations of greater than 70% by weight. Addition of carbon nanotubes to stereolithography resins and laser sintering materials were also shown to increase tensile stress and fracture stress, and increase electrical conductivity, but decrease elongation at break[50-52]. For carbon nanotubes, the max weight percentage achieved was 3%. Semiconducting and ceramic nanoparticles have also been incorporated in laser sintering, direct writing, and stereolithography. Inks including titanium dioxide nanoparticles up to 10% by weight were used to print 3D scaffolds, and were shown to have a tendency toward lower deformation and increased elastic properties [53,54]. Inks made of $BaTiO_3$ of greater than 45% by weight were also printed using direct writing and shown to increase shear stress and elastic modulus by one order of magnitude[55]. Recently, quantum dots were added to commercial Objet resin and its viscosity, surface tension, and jettability were studied[56].

With these examples of incorporating nanoparticles in 3D printing, many challenges still remain. Most prominently, the agglomeration of nanoparticles in the printing media is one of the largest problems. In addition, for stereolithography, the cure depth

can be affected by the presence of nanoparticles due to their ability to absorb UV light. Nozzles are also easily clogged with high loading of nanoparticles, and often the resulting material is brittle. Also the printed structures do not explore incorporating hierarchical designs—printed structures in literature contain nanoparticles uniformly across the structure.

In this chapter, a preliminary study of creating hierarchical suture interface designs utilizing nanoparticles and 3D printing is presented. Through hierarchical designs that selectively incorporate nanoparticles at weak points along the interface, the stiffness, strength, and toughness of triangular suture interfaces are amplified.

6.2 Materials and methods

6.2.1 Custom 3D-printing

Samples were 3D-printed with a custom built 3D printer by the Matusik Lab at MIT CSAIL. This printer allows for the printing of any UV-curable material with a viscosity under 20 cP at 70 degrees Celsius. The printer utilizes a piezoelectric print head and the waveform was calibrated for each material to ensure optimized, steady jetting of the material.

6.2.2 Drop analysis

The JetXpert (ImageXpert Inc, USA) was used to optimize the waveform and measure the average drop volume and velocity of drops. Waveforms were considered optimized if the material continuously jets out of all nozzles for over 10 minutes. Average drop volume of different materials were optimized to be around 24 picoliters.

6.2.3 Viscosity

A viscometer (Brookfield Engineering, USA) was used to measure the viscosity of the material at different temperatures. The viscosity was measured for each material at 25, 50, 60, and 70 degrees Celsius.

Nanoparticle loading	**Viscosity (cP)**			
	25°C	50°C	60°C	70°C
5%	230	43.2	26.4	16.7

10%	261	44.0	26.8	17.2

Table 6-1 | Viscosity of materials with hydroxyapatite nanoparticles at different temperatures.

6.2.4 Nanoparticle suspension

Hydroxyapatite nanoparticles were suspended in UV-curable material using an ultrasonicator. After mixing the nanoparticles, the material is processed with the ultrasonicator for one hour on pulse mode (5s on, 10 s off). The temperature is maintained under 60 degrees Celsius.

6.2.5 Triangular suture interface with multi-scale design

Hierarchical suture interfaces were designed with nanoparticles strategically placed in locations of high strain along the interface as shown in Fig. 6-1. In addition, two control suture interface designs were fabricated with homogeneous interface materials: one design utilized only the polymer, the other design utilized only the polymer with nanoparticles distributed homogeneously. All designs are tested under tension, with a constant strain rate of 0.002 s^{-1}.

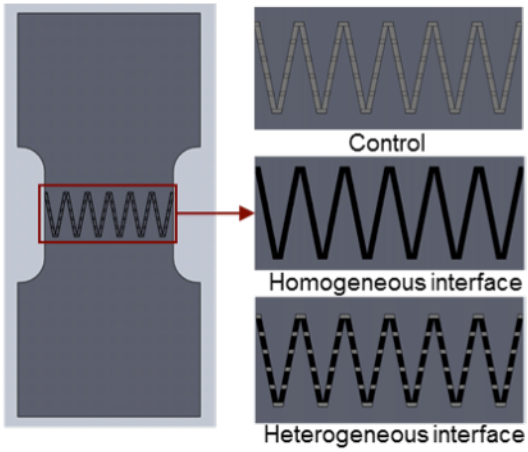

Figure 6-1 | CAD drawings of triangular suture with multiscale design. The control sample has only elastic material in the interface, while the homogeneous interface has elastic material with nanoparticles as the interface. The heterogeneous interface has elastic material with nanoparticles in the locations colored grey at the interface, and elastic material without any nanoparticles in the locations colored in black at the interface.

6.3 Results

6.3.1 Triangular suture interface with multi-scale design

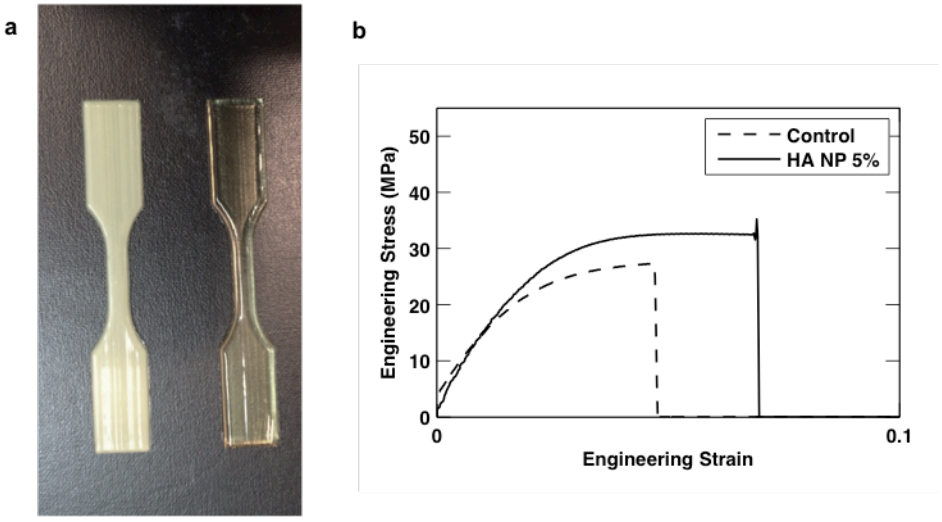

Figure 6-2 | Effect of adding nanoparticles to 3D-printed material. a Optical images of 3D-printed standard dogbones, one with nanoparticles (left) and one without (right), b Stress-strain behavior of control and material with 5 wt% nanoparticles.

As shown in Figure 6-2, the addition of nanoparticles changes the optical properties of the printed materials. Also, addition of nanoparticles to 3D-printed materials shows an increase in stiffness, strength, and toughness (Figure 6-2). Even with just 5 wt% nanoparticles, amplification of all properties is shown.

	Stiffness (MPa)	Strength (MPa)	Toughness (mJ/mm^3)
Control	53.6 +/- 4.8	2.5 +/- 0.4	0.10 +/- 0.02
Basic design	60.0 +/- 36.5	3.1 +/- 0.8	0.38 +/- 0.1

Table 6-2 | Stiffness, strength, and toughness of triangular suture interfaces with and without nanoparticles.

For a simple triangular suture interface, strategically placing nanoparticles at the weakest points along the interface leads to improved mechanical properties even relative to an interface with nanoparticles homogeneously distributed across the interface. Therefore, by using less nanoparticles at strategic locations, mechanical properties can actually be improved. This is a proof-of-concept that shows how design principles from previous chapters could lead to more efficient and better designs.

6.4 Discussion

This chapter demonstrates the potential of utilizing 3D-printing for hierarchical multi-scale design inspired by nature. Due to the layer by layer nature of 3D-printing and the ease of increasing complexity, 3D-printing is an ideal method of fabricating multi-scale hierarchical materials. Even through a basic design shown in this chapter, the mechanical properties of a suture interface can already be amplified with addition of nanoparticles. Therefore, the potential of improving materials design with this concept is incredibly promising.

Future work includes multi-scale design of hierarchical suture interfaces as discussed in Chapter 4. With an additional hierarchical design across length scales, the already amplified mechanical properties from the macroscale hierarchies should improve even more. In nature, materials sometimes show design across more than five different length scales, and it is worth investigating if that level of design in a synthetic material can reach the same, or even better, results.

6.4.1 Self-healing multi-scale hierarchical suture interfaces

In nature, damage tolerance is a critical characteristic because many natural materials are self-healing. Therefore, if the material exhibits high damage tolerance, the organism can heal itself before catastrophic failure occurs. Recently, self-healing polymeric materials that incorporate nanoparticles have been developed[57]. Therefore, following these same design principles, multi-scale hierarchical suture interfaces as shown in this chapter can incorporate self-healing nanoparticles that will heal the suture interfaces upon damage. By utilizing self-healing nanoparticles, we can fully maximize the damage tolerant characteristics of hierarchical suture interfaces.

6.4.2 Efficient suture interface design

In addition to demonstrating the effectiveness of multi-scale designs, this chapter also shows how an understanding of mechanics can lead to more efficient use of materials for suture interface designs. Even without using nanoparticles, suture interfaces can be designed to have tailored mechanical behavior using significantly less stiff material in the interface as shown in this chapter. Therefore, if a certain material is expensive, these design principles can guide the design such that a minimal amount of the expensive material is utilized.

7 Conclusion

The intricate and diverse geometries of suture interfaces in nature hint at a relationship between geometry and mechanical behavior of the suture interfaces. In this thesis, we investigated in depth how the geometry can lead to different mechanical behavior through mechanical testing of 3D-printed prototypes, finite element analysis, and development of analytical models. Through this work, we extracted design principles that can guide the efficient design of suture interfaces and composites.

7.1 Significance

7.1.1 Bio-inspired suture design principles

Through this thesis, bio-inspired design principles are extracted and outlined for the design of suture interfaces and composites. Both individual properties and the interplay between properties are explored, allowing for the design of multi-function materials. These design principles also give insight into the suture interface geometries that exist in nature, giving us a better understanding of natural structures. With the suture design principles outlined in this thesis, suture interfaces and composites with tailored mechanical behavior can be designed and fabricated.

7.1.2 Systematic methodology

In addition to the design principles, this thesis also outlines a robust method for a systematic, comprehensive understanding of the relationship between geometry and mechanical behavior. Through mechanical testing of prototypes in addition to finite element analysis and development of analytical models, a deep understanding of the mechanics and underlying role of geometry can be established. In addition to an understanding of the mechanics, the development of analytical models allow for the prediction of mechanical behavior of suture interfaces with any geometry. This methodology can be applied to any other system.

7.1.3 Development of 3D printing

As mentioned in Chapter 4, the range of mechanical behavior of 3D-printed materials can be expanded through the incorporation of suture interface and composite designs. Therefore, geometric designs can be incorporated as a method of going around the limitation of materials available for 3D printing. In addition, through this work, we demonstrated the feasibility of 3D printing polymers with nanoparticles at specific spatial locations of the prototypes. Through further development of printing polymers

with a higher percentage of nanoparticles, 3D printing can become an even more powerful tool.

7.2 Applications

Suture interfaces and composites can be incorporated into the designs of any material that requires tailored mechanical behavior. Specifically, through the design principles delineated in this thesis, materials that required tailored stiffness, strength, toughness, failure mechanisms, damage tolerance, and bending behavior can be designed utilizing suture interfaces and composites.

One possible application for suture composites is airless tires. Airless tires utilize geometry to allow for both rigidity and deformability of the tire. Utilizing suture composite designs, fully solid airless tires consisting of different materials can be designed. This can allow for precise control of the tire mechanical behavior, while maintaining the benefit of airless tires.

Another application could be for the design of snowboards. Snowboards require stiffness, strength, and flexibility that are currently achieved through layers of different materials and geometries. With suture composites, the same mechanical behavior can be achieved with just two materials, resulting in potentially cheaper and more precisely designed snowboards.

7.3 Future Work

Following the methodology outlined in this thesis, future work can further explore and unveil the relationship between three-dimensional suture interface geometry and mechanical behavior. As mentioned in the introduction, suture interfaces in nature are three-dimensional structures that vary through the thickness of the structure. The geometry in the third-dimension would significantly influence the bending behavior, creating non-linear bending behavior as interlocking occurs between the teeth of the suture interfaces. Therefore, an understanding of the effect of geometry in third-dimension would lead to suture interface and composite designs that fully take advantage of the nonlinear bending behavior.

In addition, the effect of geometry on many other mechanical properties would be a useful next step. In particular, the effect of geometry on the viscoelasticity of the overall suture structure would be worth exploring. Many applications require materials that have a certain viscoelasticity, and an understanding of the overall viscoelasticity

relative to the viscoelasticity of the constituent materials would be integral to the design of suture composites.

With the development of 3D-printing technology, synthetic suture interfaces and composites with intricate multi-scale designs and tailored mechanical behavior can be fabricated. This thesis fabricated suture interfaces with a maximum of three materials, however, with the possibility of utilizing more materials, gradients of materials and more types of nanoparticles, the mechanical behavior of suture interfaces can be even more finely tuned and designed. With the ability to conveniently and precisely fabricate complicated designs, the possibilities of new materials are endless.

References

1. CHEN, P. *et al.* Structure and mechanical properties of selected biological materials. *Journal of the Mechanical Behavior of Biomedical Materials* **1,** 208–226 (2008).
2. Vollrath, F., Madsen, B. & Shao, Z. The effect of spinning conditions on the mechanics of spider's dragline silk. *Proceedings of the Royal Society B: Biological Sciences* **268,** 2339–2346 (2001).
3. Autumn, K. *et al.* Adhesive force of a single gecko foot-hair. *Nature* **405,** 681–685 (2000).
4. Li, Y., Ortiz, C. & Boyce, M. Stiffness and strength of suture joints in nature. *Phys. Rev. E* **84,** 062904 (2011).
5. Allen, E. G. Understanding Ammonoid Sutures. *Cephalopods Present and Past: New Insights and Fresh Perspectives* 159–180 (2007).
6. Saunders, B. W. & Work, D. M. Shell morphology and suture complexity in Upper Carboniferous ammonoids. *Paleobiology* **22,** 189–218 (1996).
7. Saunders, W. B. Evolution of Complexity in Paleozoic Ammonoid Sutures. *Science* **286,** 760–763 (1999).
8. Ogle, R. C., Tholpady, S. S., McGlynn, K. A. & Ogle, R. A. Regulation of Cranial Suture Morphogenesis. *Cells Tissues Organs* **176,** 54–66 (2004).
9. Sun, Z., Lee, E. & Herring, S. W. Cranial sutures and bones: Growth and fusion in relation to masticatory strain. *Anat. Rec.* **276A,** 150–161 (2004).
10. Song, J. *et al.* Quantitative microstructural studies of the armor of the marine threespine stickleback (Gasterosteus aculeatus). *JOURNAL OF STRUCTURAL BIOLOGY* 1–14 (2010). doi:10.1016/j.jsb.2010.04.009
11. Li, Y., Ortiz, C. & Boyce, M. C. A generalized mechanical model for suture interfaces of arbitrary geometry. *Journal of the Mechanics and Physics of Solids* 1–24 (2013). doi:10.1016/j.jmps.2012.10.004
12. Li, Y., Ortiz, C. & Boyce, M. C. Bioinspired, mechanical, deterministic fractal model for hierarchical suture joints. *Phys. Rev. E* **85,** 031901 (2012).
13. De Stefano, M., De Stefano, L. & Congestri, R. Functional morphology of micro- and nanostructures in two distinct diatom frustules. *Superlattices and Microstructures* **46,** 64–68 (2009).
14. Herring, S. W. Mechanical influences on suture development and patency. *Front Oral BIology* **12,** 41–56 (2008).
15. Mechanical significance of ammonoid septa with complex sutures. 1–8 (2003).
16. Hewitt, R. A. & Westermann, G. E. G. Mechanical significance of ammonoid septa with complex sutures. *Lethaia* **30,** 205–212 (1997).
17. Saunders, W. B. The Ammonoid Suture Problem: Relationships Between Shell

and Septum Thickness and Suture Complexity in Paleozoic Ammonoids. *Paleobiology* **21,** 343–355

18. Jaslow, C. R. Mechanical properties of cranial sutures. *Journal of Biomechanics* **23,** 313–321 (1990).
19. Hubbard, R. P., Melvin, J. W.Barodawala. Flexure of cranial sutures. *Journal of Biomechanics* **4,** 491–496 (1971).
20. Krauss, S., Monsonego-Ornan, E., Zelzer, E., Fratzl, P. & Shahar, R. Mechanical Function of a Complex Three-Dimensional Suture Joining the Bony Elements in the Shell of the Red-Eared Slider Turtle. *Adv. Mater.* **21,** 407–412 (2009).
21. Bruck, H. A. Using Geometric Complexity to Enhance the Interfacial Strength of Heterogeneous Structures Fabricated in a Multi-Stage, Multi-Piece Molding Process. *Experimental Mechanics* **44,** 261–271 (2004).
22. Moazen, M. *et al.* Assessment of the role of sutures in a lizard skull: a computer modelling study. *Proceedings of the Royal Society B: Biological Sciences* **276,** 39–46 (2009).
23. Jasinoski, S. C., Reddy, B. D., Louw, K. K. & Chinsamy, A. Mechanics of cranial sutures using the finite element method. *Journal of Biomechanics* **43,** 3104–3111 (2010).
24. Lin, E., Li, Y., Ortiz, C. & Boyce, M. C. 3D printed, bio-inspired prototypes and analytical models for structured suture interfaces with geometrically-tuned deformation and failure behavior. *Journal of the Mechanics and Physics of Solids* **73,** 166–182 (2014).
25. Bruet, B. J. F., Song, J., Boyce, M. C. & Ortiz, C. Materials design principles of ancient fish|[nbsp]|armour. *Nature Materials* **7,** 748–756 (2008).
26. Zhang, Y., Yao, H., Ortiz, C., Xu, J. & Dao, M. Bio-inspired interfacial strengthening strategy through geometrically interlocking designs. *Journal of the Mechanical Behavior of Biomedical Materials* **15,** 70–77 (2012).
27. Li, B.-W., Zhao, H.-P., Qin, Q.-H., Feng, X.-Q. & Yu, S.-W. Numerical study on the effects of hierarchical wavy interface morphology on fracture toughness. *Computational Materials Science* **57,** 14–22 (2012).
28. Pritchard, J. J., Scott, J. H. & Girgis, F. G. The structure and development of cranial and facial sutures. *Journal of Anatomy* **90,** 73–85 (1956).
29. Dunlop, J. W. C. & Fratzl, P. Biological Composites. *Annu. Rev. Mater. Res.* **40,** 1–24 (2010).
30. Dunlop, J. W. C., Weinkamer, R. & Fratzl, P. Artful interfaces within biological materials. *Materials Today* **14,** 70–78 (2011).
31. Li, Y., Ortiz, C. & Boyce, M. C. A Generalized Mechanical Model for Suture Interfaces of Arbitrary Geometry. *Journal of the Mechanics and Physics of Solids* 1–51 (2012). doi:10.1016/j.jmps.2012.10.004
32. Wang, L., Song, J., Ortiz, C. & Boyce, M. C. Anisotropic design of a multilayered

biological exoskeleton. *J. Mater. Res.* **24,** 3477–3494 (2011).
33. Browning, A., Ortiz, C. & Boyce, M. C. Mechanics of composite elasmoid fish scale assemblies and their bioinspired analogues. *Journal of the Mechanical Behavior of Biomedical Materials* **19,** 75–86 (2013).
34. Dimas, L. S., Bratzel, G. H., Eylon, I. & Buehler, M. J. Tough Composites Inspired by Mineralized Natural Materials: Computation, 3D printing, and Testing. *Advanced Functional Materials* **23,** 4629–4638 (2013).
35. Li, Y., Kaynia, N., Rudykh, S. & Boyce, M. C. Wrinkling of Interfacial Layers in Stratified Composites. *Advanced Engineering Materials* **15,** 921–926 (2013).
36. Lin, E., Li, Y., Weaver, J. C., Ortiz, C. & Boyce, M. C. Tunability and enhancement of mechanical behavior with additively manufactured bio-inspired hierarchical suture interfaces. *J. Mater. Res.* **29,** 1867–1875 (2014).
37. Katti, K. S., Katti, D. R., Pradhan, S. M. & Bhosle, A. Platelet interlocks are the key to toughness and strength in nacre. *J. Mater. Res.* **20,** 1097–1100 (2005).
38. Ritchie, R. O. The conflicts between strength and toughness. *Nature Materials* **10,** 817–822 (2011).
39. Wang, L., Lau, J., Thomas, E. L. & Boyce, M. C. Co-Continuous Composite Materials for Stiffness, Strength, and Energy Dissipation. *Adv. Mater.* **23,** 1524–1529 (2011).
40. Meyers, M. A., Chen, P.-Y., Lin, A. Y.-M. & Seki, Y. Biological materials: Structure and mechanical properties. *Progress in Materials Science* **53,** 1–206 (2008).
41. Zhou, H. & Zhang, Y. Hierarchical Chain Model of Spider Capture Silk Elasticity. *Phys. Rev. Lett.* **94,** 028104 (2005).
42. Yao, H. & Gao, H. Mechanics of robust and releasable adhesion in biology: Bottom–up designed hierarchical structures of gecko. *Journal of the Mechanics and Physics of Solids* **54,** 1120–1146 (2006).
43. Long, C. A. & Long, J. E. Fractal Dimensions of Cranial Sutures and Waveforms. *Cells Tissues Organs* **145,** 201–206 (1992).
44. Jaslow, C. R. & Biewener, A. A. Strain patterns in the horncores, cranial bones and sutures of goats (Capra hircus) during impact loading. *Journal of Zoology* **235,** 193–210 (1995).
45. Daniel, T. L., Helmuth, B. S., Saunders, W. B. & Ward, P. D. Septal complexity in ammonoid cephalopods increased mechanical risk and limited depth. *Journal Information* (2010). doi:10.1666/0094-8373(1997)023[0470:SCIACI]2.3.CO;2
46. Hassan, M. A., Westermann, G. E. G., Hewitt, R. A. & Dokainish, M. A. Finite-element analysis of simulated ammonoid septa (extinct Cephalopoda): septal and sutural complexities do not reduce strength. *Journal …* **28,** 113–126 (2009).
47. Ortiz, C. & Boyce, M. C. Bioinspired Structural Materials. *Science* **319,** 1053–1054 (2008).
48. Meyers_BiolMatMech_StructuralBiolComposites2006.

49. Ahn, B. Y. *et al.* Omnidirectional Printing of Flexible, Stretchable, and Spanning Silver Microelectrodes. *Science* **323,** 1590–1593 (2009).
50. Yildirim, E. D., Yin, X., Nair, K. & Sun, W. Fabrication, characterization, and biocompatibility of single-walled carbon nanotube-reinforced alginate composite scaffolds manufactured using freeform fabrication technique. *Journal of Biomedical Materials Research Part B: Applied Biomaterials* **87B,** 406–414 (2008).
51. Athreya, S. R., Kalaitzidou, K. & Das, S. Mechanical and microstructural properties of Nylon-12/carbon black composites: Selective laser sintering versus melt compounding and injection molding. *Composites Science and Technology* **71,** 506–510 (2011).
52. Goodridge, R. D. *et al.* Processing of a Polyamide-12/carbon nanofibre composite by laser sintering. *Polymer Testing* **30,** 94–100 (2011).
53. Cai, K. *et al.* Direct-writing construction of layered meshes from nanoparticles-vaseline composite inks: rheological properties and structures. *Appl. Phys. A* **102,** 501–507 (2011).
54. Bin Duan, Cheung, W. L. & Wang, M. Optimized fabrication of Ca–P/PHBV nanocomposite scaffolds via selective laser sintering for bone tissue engineering. *Biofabrication* **3,** 015001 (2011).
55. Li, Q. & Lewis, J. A. Nanoparticle Inks for Directed Assembly of Three-Dimensional Periodic Structures. *Adv. Mater.* **15,** 1639–1643 (2003).
56. Campbell, T. A. & Ivanova, O. S. 3D printing of multifunctional nanocomposites. *Nano Today* **8,** 119–120 (2013).
57. Wu, D. Y., Meure, S. & Solomon, D. Self-healing polymeric materials: A review of recent developments. *Progress in Polymer Science* **33,** 479–522 (2008).

Appendix A. Derivation of stress distribution in the teeth for suture interfaces with a bonded tip

As derived in Li et. al (2013), force equilibrium yields the relationship between the normal stress in the teeth, $\sigma_{yy}(y)$, and the interfacial shear stress, τ_T,and normal stress σ_T

$$\left[\sigma_{yy}(y) + d\sigma_{yy}\right][w(y) + dw] = \tau_T \frac{dy}{\cos\beta} + \sigma_T \frac{dy}{\cos\beta}\sin\beta. \tag{A.1}$$

Neglecting higher order terms,

$$d\left[\sigma_{yy}(y)w(y)\right] = [\tau_T + \sigma_T \tan\beta]dy. \tag{A.2}$$

By using Eq. (2),

$$\frac{d[\sigma_{yy}(y)w(y)]}{dy} = \frac{\tau_T}{\cos^2\beta}. \tag{A.3}$$

Applying the boundary conditions, $\sigma_{yy}(0) = \sigma_{tip}$, and $\sigma_{yy}(A) = \sigma_{base}$, the stress distribution in the teeth, $\sigma_{yy}(y)$, is derived as

$$\sigma_{yy}(y) = \frac{[\sigma_{base}\tan\varphi - \sigma_{tip}(\tan\varphi - \tan\beta)]y + A(\tan\varphi - \tan\beta)\sigma_{tip}}{y\tan\beta + A(\tan\varphi - \tan\beta)}. \tag{A.4}$$

Using the stress distribution, B_{tooth} in Eq. (9b) can also be expressed as

$$B_{tooth} = \frac{4}{V\bar{\sigma}^2}\int_0^A \frac{\sigma_{yy}(y)^2}{E_1} w(y)dy =$$
$$\frac{4}{V\bar{\sigma}^2}\frac{A^2}{E_1\tan^3\beta}\Big[\tan\beta\left(\sigma_{tip}(a\tan\beta) + \sigma_{base}\tan\varphi\right)\Big(\sigma_{base}\tan\varphi\left(-3\tan\beta + 2\tan\varphi\right) -$$
$$\sigma_{tip}(a\tan\beta)(\tan\beta + 2\tan\varphi)\Big) + 2\sigma_{diff}^2(a\tan\beta)^2\ln\left(A\left(1 + \frac{1}{a}\right)\right)\Big], \tag{A.5a}$$

where V is the total volume, $\bar{\sigma}$ is the far-field loading and is given by Eq. (1), $w(y)$ is the profile of the slant edge and is given by Eq. (6c), and where

$$\sigma_{diff} = \sigma_{base} - \sigma_{tip} = \frac{\frac{G_0}{g}\left(\frac{g_0}{E_0^{PS}} - \frac{A}{E_1}\right)\sec^2\beta - \tan\beta}{\tan\varphi - \tan\beta + \frac{G_0}{E_0^{PS}}\frac{g_0}{g}\sec^2\beta}, \tag{A.5b}$$

and where,

$$a = \frac{tan\varphi}{tan\beta} - 1. \qquad \text{(A.5c)}$$